# Applying Small UAS to Produce Survey Grade Geospatial Products for DOT Preconstruction & Construction

**NCDOT Project 2020-18**
**FHWA/NC/2020-18**
**October 2021**

---

Kevin Han, PhD
William Rasdorf, PhD, PE
Yajie Liu
Civil, Construction, and Environmental Engineering
North Carolina State University

NC STATE UNIVERSITY

STATE OF NORTH CAROLINA DEPARTMENT OF TRANSPORTATION

RESEARCH & DEVELOPMENT

## Technical Report Documentation Page

| | | |
|---|---|---|
| 1. Report No.<br>**FHWA/NC/2020-18** | 2. Government Accession No. | 3. Recipient's Catalog No. |
| 4. Title and Subtitle<br>**Applying Small UAS to Produce Survey Grade Geospatial Products for DOT Preconstruction & Construction Activities** | | 5. Report Date<br>**October 31, 2021**<br>6. Performing Organization Code |
| 7. Author(s)<br>**Dr. Kevin Han, Dr. William Rasdorf, and Yajie Liu** | | 8. Performing Organization Report No. |
| 9. Performing Organization Name and Address<br>**North Carolina State University**<br>**Department of Civil, Construction and Environmental Engineering**<br>**Campus Box 7908**<br>**Raleigh, NC 27606** | | 10. Work Unit No.<br>11. Contract or Grant No. |
| 12. Sponsoring Agency Name and Address<br>**North Carolina Department of Transportation**<br>**Research and Development Unit**<br>**1020 Birch Ridge Drive, Building B**<br>**1549 Mail Service Center**<br>**Raleigh, NC 27699-1549** | | 13. Type of Report and Period Covered<br>**Draft Final Report**<br>**August 2019 to October 2021**<br>14. Sponsoring Agency Code<br>**RP 2020-18** |
| Supplementary Notes: | | |

16.Abstract: This project aimed to develop a set of comprehensive guidelines, recommendations, and specifications of applying small unmanned aerial system (UAS) for the North Carolina Department of Transportation (NCDOT) to produce survey-grade geospatial products on preconstruction and construction activities. A series of data collection and data evaluation tests were performed at six sites with different terrain types. Those sites included two preliminary sites located at North Carolina State University (NCSU) and four main UAS test sites coordinated by NCDOT. For the preliminary sites, the first site was a track facility site. The second one was a vertical structure near Lake Raleigh. The four UAS test sites included one facility site in Butner, two construction sites in High Point and Clinton, and one sloped site with rock surfaces in Mars Hill.

The collected geospatial data was used to 1) evaluate appropriate sensors for specific landcover, 2) assess flight altitudes and their associated vertical and horizontal accuracies, 3) determine the distance between ground sampling distance (GSD), 4) determine an appropriate number of ground control points (GCPs), their distribution, and weight, 5) determine image overlap in orthogonal directions, quality, and resolution, and 6) strategies for continuous surveying for capturing construction progress and changes in terrain.

Moreover, the collected data was also used to evaluate multiple factors that affect horizontal and vertical accuracies during data acquisition and processing. In addition, a quantitative analysis called the multiple regression (MR) method was developed to evaluate the level of significance of different flight configurations (i.e., flight height, image overlap, GCP quantity, focal length, and image quality) on accuracy. Furthermore, the developed MR model can be used to predict survey accuracy.

Additionally, research on the influence of GCP spacing and quantity on the accuracy was conducted using different numbers and separation distances of GCPs. This research was conducted at the corridor-shaped construction site and the Butner UAS test site.

Lastly, a set of guidelines and specifications that resulted from this research was developed, which will enable NCDOT to produce consistent and reliable survey-grade geospatial data using UAS-based photogrammetry surveying.

| | | | |
|---|---|---|---|
| 17. Key Words<br>**Unmanned Aerial System, Photogrammetry, Surveying, Geospatial Product** | 18. Distribution Statement | | |
| 19. Security Classif. (of this report)<br>**Unclassified** | 20. Security Classif. (of this page)<br>**Unclassified** | 21. No. of Pages | 22. Price |

**Form DOT F 1700.7** (8-72) **Reproduction of completed page authorized**

## DISCLAIMER

The contents of this report reflect the views of the authors who are responsible for the facts and the accuracy of the data presented herein. The contents of the report do not reflect the official views or policies of the North Carolina Department of Transportation.

## ACKNOWLEDGMENTS

The authors would like to acknowledge the North Carolina Department of Transportation for sponsoring this project and the steering committee (Curtis T. Bradley, Webster Moore, Keith Johnston, Wesly Cartner, Aaron Earwood, John L. Pilipchuk, Marc Swartz, Thomas Walls, Mark Ward, and Neil Mastin) and others who were involved (Matthew Macon, Patrick Tuttle, Richard Hensley, Donald Early, Jody Kuhne, Dale Burton, Richard Greene, and Rodney Hough) for their aid and assistance with the various tasks and activities of the project. We are sincerely grateful.

## EXECUTIVE SUMMARY

Recent advances in small unmanned aerial systems (UASs) and sensing technologies have enabled relatively low-cost and effective surveying methods for preconstruction, construction, and sloped sites. However, the commercial software that accompanies these technologies produces inconsistent and unreliable survey results, and there are no guidelines for ensuring the quality of the data. Without proper guidelines and specifications, repeated surveying at a designated area over time (e.g., a construction site with periodic data collection) is not ideal.

The goal of this research was to develop a comprehensive set of guidelines, recommendations, and specifications for producing survey-grade geospatial products using UAS solutions for applications in preconstruction, construction, and sloped sites. To achieve this goal, a series of data collection and evaluation tests at six sites with varying terrain types were conducted, including two preliminary test sites located at NC State University (NCSU) campus and four main test sites coordinated by the NCDOT. These six sites were:

1) Track facility site at NCSU campus, Raleigh, NC,
2) Lake Raleigh site at NCSU campus, Raleigh, NC,
3) NCDOT/NCEM UAS Test site in Butner, NC,
4) U2412-A construction site: a roadway construction site with disturbed terrain in High Point, NC,
5) R-2303E pit site: a large construction site with disturbed terrain in Clinton, NC, and
6) I-26 rock slope site: an open terrain site with rock surface near I-26 highway in Mars Hill, NC.

The collected geospatial data was processed using three software products of NCDOT's interest. The data was evaluated to create guidelines and recommendations for data acquisition, processing, and evaluation. A set of accuracy specifications that can help NCDOT estimate reasonable survey accuracy given site constraints and hardware was also developed.

The collected data was also used to evaluate multiple factors that affect horizontal and vertical accuracies during data acquisition and processing. In addition, a quantitative analysis called the multiple regression (MR) method was developed to evaluate the level of significance of different flight configurations (i.e., flight height, image overlap, ground control point (GCP) quantity, focal length, and image quality) on accuracy. Furthermore, the developed MR model can be used to predict survey accuracy.

Lastly, this research investigated how GCP spacing and quantity can affect the survey accuracy by analyzing multiple numbers of GCPs and their spacing. The data from the U2412-A and the Butner UAS test sites were used for this study. The results show expected accuracies with different GCP spacing.

This research is a systematic approach to the implementation of UASs with the non-metric camera. The produced guidelines, specifications, and recommendations that have resulted from the work enable this implementation to be accomplished so that accurate and useful data are available for NCDOT to perform UAS photogrammetric surveying.

**TABLE OF CONTENTS**

## LIST OF TABLES

## LIST OF FIGURES

# Chapter 1 Introduction

## 1.1 Problem Statement

There have been rapid advances in small unmanned aerial systems (UAS) and photogrammetry technologies that turn 2D digital images (non-metric) into 3D surveying data, enabling cost-effective, efficient, and accurate surveying for various civil engineering applications. With these advances, there is now many commercial software products that produce 3D geospatial data (often known as point clouds), such as Agisoft Metashape, Pix4Dmapper, PhotoModeler, and UASMaster.

However, the NC Department of Transportation (NCDOT) has experienced inconsistent and unreliable survey results using these latest technologies. This inconsistency is caused by inherent limitations of computer vision algorithms that estimate 3D points from 2D images (detailed in Ch. 2 Literature Review). Moreover, the aforementioned commercial software products are "black boxes," and their users, including NCDOT, often cannot comprehend the causes of inconsistency. There is no comprehensive set of guidelines and specifications that would allow NCDOT to overcome this limitation, produce consistent and reliable survey data at a designated area over time (i.e., a construction site with periodic data collection), and evaluate survey results.

Therefore, the main objective of this research was to develop a comprehensive set of guidelines and specifications for producing survey-grade geospatial products using UAS solutions for the applications of NCDOT's interest - preconstruction, construction, and sloped sites. To develop these guidelines and specifications, there is a need for 1) a literature review of the latest UAS solutions and practices by state DOTs and private sectors and 2) a structured set of research experiments with different settings and configurations of UASs with sensors and terrain types. More detailed research objectives are specified below.

## 1.2 Research Objectives

To achieve the aforementioned objective of developing guidelines and specifications, a series of data collection and evaluations at various sites with varying terrain types were conducted. Two sites with different terrains at NC State University (NCSU) were chosen as the preliminary study sites - a track facility and a vertical structure near Lake Raleigh. In addition, four main test sites were identified through coordination with NCDOT. These sites were:

1) NCDOT/NCEM UAS Test Site in Butner, NC,
2) U2412-A construction site: a roadway construction site with a disturbed terrain in High Point, NC,
3) R-2303E Pit site: a large construction site with disturbed terrain in Clinton, NC, and
4) I-26 rock slope site: an open terrain site with a sloped rock surface near the I-26 highway in Mars Hill, NC.

The collected geospatial data was used to evaluate:

1) Appropriate sensors for specific landcover,
2) Flight altitudes and their associated vertical and horizontal accuracies,
3) The distance between two pixels on the ground (known as ground sampling distance (GSD)),
4) An appropriate number of ground control points (GCPs), their distribution, and weight,
5) Image overlap in orthogonal directions, quality, and resolution (especially with regards to flight altitudes and GSD), and
6) Strategies for continuous surveying for capturing construction progress and changes in terrain.

### 1.3 Research Methods Overview

To achieve the aforementioned objectives, there were seven steps of research as follows:

1) Literature review to identify past research studies, currently available products (both software and hardware) and services, and applications of small UAS solutions for surveying.
2) Data collection at two preliminary study sites on the NCSU campus and four test sites arranged by NCDOT.
3) Data processing of UAS imagery using three structure-from-motion (SfM) software products - Pix4D, Agisoft, and UASMaster.
4) Data evaluation of 3D geospatial data to identify appropriate 1) sensors for specific terrain types, 2) flight altitudes and associated vertical and horizontal accuracies, 3) GSD, 4) number of GCPs, their distribution, and their weights, 4) image overlap in orthogonal directions, quality, and resolution, and 5) strategies for continuous surveying for capturing construction progress and changes in terrain.
5) Causes of inconsistencies identification by evaluating data collected in different types of environments. This evaluation was the basis for developing guidelines that minimize the risk of producing inconsistent survey data from non-metric sensors.
6) Guidelines and recommendations development by summarizing the findings of the previous tasks, which will enable NCDOT to produce consistent and reliable geospatial data using UAS-based photogrammetry for preconstruction, construction, and sloped sites. Moreover, simple guidelines for quick evaluation of geospatial data (output of "black box" tools) were developed.
7) Specifications development. A set of specifications will allow NCDOT to have reasonable expectations on the level of accuracy it and its subcontractors can produce, given the site constraints and a known set of hardware.

### 1.4 Structure of Report

This report is organized in chapters that are in a sequence to match the methodology. Each chapter provides detailed information on its topic.

- *Chapter 2 Literature Review* presents a comprehensive literature review of past research studies, currently available products (both software and hardware) and services, and a review of applications of small UAS solutions for surveying.
- *Chapter 3 Data Collection* describes the data collection at six sites, including the preliminary test sites at NC State University and the test sites coordinated by NCDOT.
- *Chapter 4 Data Processing* introduces the three SfM software used for the data processing, including their settings and parameters.
- *Chapter 5 Data Evaluation* presents the summarized findings and results from the data collection and data processing.
- *Chapter 6 Identify Causes of Inconsistencies* lists the identified causes of inconsistent results and the ways to mitigate their risks.
- *Chapter 7 Conclusion* presents the overall conclusions.
- *Chapter 9 Appendix* includes 1) entire set of results from data processing and evaluation, 2) guidelines and recommendations, 3) specifications, 4) accuracy prediction modeling, and 5) GCP spacing.

# Chapter 2 Literature Review

The first task of the proposed research was an examination of the current literature to identify past research studies, currently available products (both software and hardware) and services, and applications of small UAS solutions for surveying. The investigation included journal papers, conference papers, committee reports, technical reports, technical and implementation guidelines, product literature, and specifications produced by state DOTs. This task sought to fill the gaps in knowledge of this subject matter. The literature review is organized by topics that are relevant to the present work as follows: image-based 3D reconstruction, UAS applications in state DOTs, UAS accuracy documents, and impact factors of UAS-based photogrammetric surveying accuracy.

## 2.1 Image-based 3D Reconstruction: Concepts and Limitations

With the development of feature detection and matching, structure-from-motion (SfM) techniques, and multi-view stereo (MVS), 3D scene reconstruction from 2D images is now widely being used (Snavely et al., 2007). Feature detection and matching finds visual features (i.e., corners) from images and match corresponding features from different images. These techniques typically rely on concepts like random sample consensus (RANSAC) that randomly selects a set of features from two images, calculates root mean square error (RMSE), and repeats this process until RMSE is below a threshold. This means that feature detection and matching are designed to be inherently inconsistent even if two sets of images are collected using the same flight configuration and from the same site. Unless the two sets consist of the exact same images, the set of detected and matched features will be different.

The second step of 3D reconstruction is SfM, which creates a structure (i.e., scene) from a motion that is created by multiple sets of features among multiple images. Simply speaking, SfM estimates camera poses (i.e., positions and orientation) and triangulates 3D points from corresponding features. During this process, camera intrinsic (focal length, distortion coefficient, etc.) parameters are also estimated, self-calibrating the camera. SfM is followed by Bundle adjustment (BA) that optimizes as more images are processed (Förstner & Wrobel, 2016).

Multi-view stereo (MVS) is the general term that uses stereo correspondence as their main cue and for more than two images through a group of techniques (Seitz et al., 2006). MVS is used to fill in a sparsely created 3D point cloud from SfM, creating a dense point cloud.

## 2.2 UAS Applications in State DOTs

There have been many research efforts that utilize small UASs by state DOTs in different research fields with different sensors for various purposes. Table **2.1. Literature Review of Similar Projects by State DOTs (* Construction Applications)**Table 2.1 summarizes past efforts with their technical reports and ongoing efforts. 22 technical reports from state DOTs are listed here.

**Table 2.1. Literature Review of Similar Projects by State DOTs (* Construction Applications)**

| State DOT | Project Description | Sensors | | | Motivation for Research | | | | Drone Usage | | | | |
|---|---|---|---|---|---|---|---|---|---|---|---|---|---|
| | | Camera | LiDAR | Thermal | Applicability Evaluation | Inspection | Equipment and Workflow | Literature Review | Inspection | Traffic Monitor | Collision Reconstructio | Surveying* | Mapping* |
| Florida (June 2015) (Otero, 2015) | Proof of Concept for Using Unmanned Aerial Vehicles for High Mast Pole and Bridge Inspections | X | - | - | X | X | X | - | X | - | - | - | - |

| | | | | | | | | | | | | | | | | |
|---|---|---|---|---|---|---|---|---|---|---|---|---|---|---|---|---|
| GDOT (April 2019) (Irizarry and Johnson, 2019) | This project aimed to develop guidelines for integrating UASs in GDOT operations based on the experience and lessons learned from field tests with UAS technology on selected tasks performed by several groups within GDOT. | X | - | - | X | X | - | - | X* | - | - | X* | - |
| IDOT (August 2017) (Dorafshan et al., 2017) | Fatigue crack detection under bridge inspection. Including a rich literature review. | X | - | X | X | X | X | X | X | - | - | - | - |
| INDOT (March 2020) (Hubbard, S, and Hubbard, B. 2020) | This document provides an overview of UAS applications that may be appropriate for INDOT, as well as a description of the regulations that affect UAS operation as described in 14 CFR Part 107. | X | | | X | - | - | X | X* | - | - | X* | - |
| KDOT (August 2016) (Mcguire et al., 2016) | A literature review on the commercial companies currently using UASs and research done by other DOTs. | X | - | - | X | - | - | X | X | X | X | X* | X* |
| MassDOT (December 2019) (Plotnikov et al. 2019) | Central to the conduct of this research was a review of current procedures used in state DOT bridge and rail inspections and the experiences of these state DOTs in integrating UAS technologies into such inspections. Based on this review, the UMass research team developed and tested practical procedures and protocols to guide MassDOT in the integration of UAS technologies into bridge and rail inspections. | X | - | - | X | - | - | - | X | - | - | - | - |
| MDOT (April 2015 (Brooks et al., 2014) | Testing and evaluating five main UAS platforms with a combination of sensors to assess critical transportation infrastructure and issues such as bridges, confined spaces, traffic flow, and roadway assets. | X | X | X | X | - | - | - | X | X | - | - | - |
| MDOT (May 2018) (Brooks et al., 2018) | Testing and evaluating five main UAS platforms with a combination of sensors to determine how to implement them into MDOT workflows. Field demonstrations were completed at bridges, a construction site, road corridors, and along highways. | X | X | X | X | - | - | - | X | X | - | - | - |
| Minnesota DOT (July 2015) (Lovelace, B., and Zink, J. 2015) | Evaluate technologies and studies safety concerns for bridge inspection | X | - | - | X | X | - | - | X | - | - | - | - |
| Minnesota DOT (July 2018) (Wells, J., and Lovelace, B. 2018) | Improving the Quality of Bridge Inspections Using UAS. This is phase III. Phase II focused on the rules and regulations, drone hardware, and the ability of drones to collect quality inspection data. | X | - | - | X | X | X | - | X | - | - | - | - |
| Missouri DOT (May 2018) (Lercel et al. 2018) | Explores the adoption of UAS technology at the national and state levels – focusing on the role of transportation agencies, activities, policies, and strategies promoting safe UAS operations and economic growth. | - | - | - | X | - | - | - | - | - | - | - | - |
| Montana DOT (March 2017) (Beal, 2017) | Describes the equipment and workflows used to collect imagery of the Lincoln Rd. | X | - | - | - | - | X | - | - | - | - | X* | - |
| New England Transportation Consortium – MassDOT, Rhode Island DOT, NHDOT, Maine DOT, CDOT, VDOT (March 2021) (Mallela et al. 2021) | This research aims to provide guidance to New England state DOTs regarding effective practices when incorporating UAS into daily operations. | X | - | - | X | - | - | - | X | X | - | X* | X* |
| NCDOT (May 2018) (Eyerman et al., 2018) | Evaluates the suitability of using UAS to perform low-light collision scene reconstructions | X | - | - | X | - | X | - | - | - | X | - | - |
| NCDOT (January 2020) (Gray et al., 2020) | This information was synthesized into authoritative guidance on UAS platforms, payloads, flight operations, and the UAS regulatory environment. | X | X | X | X | - | - | - | - | - | - | - | X |
| NHDOT (June 2019) (O'Neil-Dunne and Estabrook 2019) | Evaluates UAS related technologies for a broad range of applications in the NHDOT. | X | - | - | X | - | - | - | X* | X | - | - | X |
| NYSDOT (June 2017) (Kamga et al., 2017) | Assess the existing capabilities of UAS and UGS technologies for responding to highway incidents, including field surveying, accident information collection and reconstruction, and other related requirements to clearing a highway incident. It also explores other transportation applications such as bridge inspection, traffic monitoring, road construction, and maintenance worker safety. | X | - | - | X | - | - | X | X | X | - | - | X |
| ODOT (February 2018 (Gillins et al., 2018) | Evaluate the use of UAS in bridge inspection | X | - | - | X | X | X | X | X | - | - | - | - |
| ODOT (March 2018) (Hurwitz et al., 2018) | Simulator study on the effects that drones used for bridge inspections and other highway-related uses have on the traveling public. | X | - | - | X | - | - | - | X | - | - | - | - |
| SCDOT (December 2019) (Bausman, D, and Commert, G 2019) | This report outlines the findings of a study to explore the benefits of UAS technology when deployed at the SCDOT, specifically focused on the areas of land surveying and bridge inspection. | X | - | - | X | X | - | - | X | - | - | X* | - |
| Texas A&M Transportation Institute (TTI, December 2017) ( (Stevens & Blackstock, 2017) | Conducts the demonstration over two days to monitor traffic, detect incidents, respond to incidents, provide situational awareness, and investigate crash scene mapping capabilities. | X | - | - | X | - | X | - | - | X | - | - | - |
| USDOT – Arkansas DOT, Connecticut DOT, and Florida DOT (October 2016) (Gillins et al. 2016) | Investigate the use of UAS technology as a tool for assisting with a bridge inspection | X | - | - | - | X | - | X | X | - | - | - | - |

*Florida Department of Transportation (FDOT)* (2015) utilized small UAS equipped with high-definition cameras for structural inspection in limited fields, such as indoor, underside bridge sections, and high mast luminaires. Preliminary results showed that potential cost savings in man-hours and safety risks were achieved by using small UAS instead of conventional methods. Moreover, the effectiveness and accuracy of structural health evaluations were also improved (Otero et al., 2015).

*Georgia Department of Transportation (GDOT)* (2019) developed a set of guidelines for the UAS operations based on the experience and lessons learned from field tests with UAS technology on selected tasks performed by several groups within GDOT. The field tests included two airports, two rail segments, one road construction site, and two bridges from the Construction, Bridge Maintenance, and Intermodal groups. Various data was collected during the field tests, consisting of images, infrared images, and videos. Flights were performed in both manual and automated modes (Irizarry and Johnson, 2019).

*Idaho Department of Transportation (IDOT)* (2017) studied the applications of UAS for bridge inspection, with emphasis on under bridge inspection and fatigue crack detection using three UASs (3DR Iris, Goose, DJI Mavic). An in-service bridge in Ashton, Idaho, was inspected using the proposed UAS to detect fatigue cracks. The results showed that digital image processing methods could be utilized to assist the inspector in finding concrete cracks. IDOT found that real-time and automated visual concrete crack detection is possible and is effective with 90% accuracy (Dorafshan et al., 2017).

*Indiana Department of Transportation (INDOT)* (2020) presented an overview of UAS applications that may be appropriate for their operations using the Quality Function Deployment (QFD) method. INDOT considered the technical feasibility, ease of adoption, stakeholder acceptance, underway activities, contribution to its mission, and goals. Also, an estimate of the benefits and costs of using drones was made, based on findings from other agencies and projections for INDOT (Hubbard and Hubbard, 2020).

The *Kansas Department of Transportation (KDOT)* (2016) discussed the potential applications, concerns, and specific equipment of UAS usage with commercial companies using drones to provide a justified recommendation of if it is beneficial to implement UAS into the KDOT routine operations. According to KDOT's report, applying UASs for bridge inspection, radio tower inspection, surveying, road mapping, high-mast light tower inspection, stockpile measurement, and aerial photography is beneficial (Mcguire et al., 2016).

*Massachusetts Department of Transportation (Mass DOT)* (2019) reviewed current procedures used in state DOT bridge and rail inspections and the experiences of these state DOTs in integrating UAS technologies into such inspections. Based on those reviews, a set of practical procedures and protocols were developed and tested to enable Mass DOT to integrate UAS technologies into bridge and rail inspections (Plotnikov et al., 2019).

*Michigan Department of Transportation (MDOT)* (2014) tested and evaluated five main UAS platforms with a combination of optical, thermal, and LiDAR sensors to assess some critical transportation infrastructure and issues, such as bridges, confined spaces, traffic flow, and roadway assets. Through the project, two bridges, two pump stations, two traffic sites, and a roadway asset site were selected and evaluated via UAV-based imaging. The results demonstrated that UAS technologies provide many advantages to help MDOT cost-effectively assess, manage, and maintain its resources, benefitting its staff and the traveling public. Also, MDOT developed an Implementation Action Plan (IAP) with a series of seven ideas for potential follow-on research, including 1) formal crash scene

imaging, 2) slope stability assessment, 3) aerial imaging to meet MDOT survey support, 4) optimal methods to store and share large UAV- based data sets, 5) improvements to UAV-based thermal imaging, 6) multi-sensor high-accuracy UAV positioning, and 7) UAV traffic monitoring for traffic operation centers (Brooks et al. 2014).

In 2018, the *MDOT* project continued to test and evaluate five main UAV platforms with a combination of optical, thermal, and LiDAR sensors to determine how to implement them into MDOT workflows. Field demonstrations were completed at bridges, construction sites, road corridors, and highways, with data being processed and analyzed using customized algorithms and tools. Additionally, a cost-benefit analysis was conducted, comparing manual and UAV-based inspection methods. This project proved that implementing UAV technologies into MDOT workflows could provide many benefits to MDOT and the motoring public, such as advantages in improved cost-effectiveness, operational management, and timely maintenance of Michigan's transportation infrastructure (Brooks et al., 2018).

*Minnesota Department of Transportation (MNDOT)* (2015) studied the effectiveness of adopting UAS to inspect bridges safely. Four bridges located in Minnesota were selected to be investigated by the project team as case studies. The results demonstrated that UASs could be utilized as a tool to safely and effectively inspect the bridge, especially the larger bridges, compared to other methods such as aerial work platforms (AWP) and rope access. Defects could be detected through the images collected by UAS. Measurements could be estimated from images, but tactile functions, such as cleaning, sounding, measuring, and testing, equivalent to a hands-on inspection, cannot be replicated using UASs (Lovelace and Zink, 2015).

In 2018, *MNDOT* and Collins Engineers identified new drone technology and methods to address the limitations of the previous phases. For instance, the ability to inspect very tight areas and confined spaces were investigated. To achieve this, they used a collision-tolerant drone with a cage around the drone to access such challenging areas. Also, they implemented UAS technology on 39 bridges for inspection. The results demonstrated that drone technology and processing software are effective tools to improve the quality of bridge inspections and improve safety and reduce costs (Wells and Lovelace, 2018).

*Missouri Department of Transportation (MODOT)* (2018) investigated the utilization of UAS technology at the national and state levels. The national level was a macro look at the broader UAS application across the country. At the state level, they evaluated five states within the same central United States region as Missouri (Iowa, Kansas, Minnesota, North Dakota, and Oklahoma). The micro-level research focused on the states' strategies, policies, activities, and the role of state agencies regarding UAS adoption. The results showed that many state DOTs were adopting UAS technology in various projects while developing policies and procedures to support safe and legal UAS operations. Moreover, the feasibility of adopting UASs in Missouri was evaluated in this study. The use of UAS can assist in economic growth. In the end, strategic opportunities and recommendations that can help Missouri to prepare for future UASs adoption opportunities were proposed (Lercel et al., 2018).

*Montana Department of Transportation (MTDOT)* (2017) presented the equipment and workflows for collecting imagery of the Lincoln Rd. MDT Section yard. Moreover, a rectified orthomosaic map, point cloud (LAS file), and a Digital Surface Model (DSM) were processed using Pix4D. Stockpile volumes were measured, and a visualization video clip was created. In addition, FAA regulations were discussed in this report. For example, aircraft must be registered and must weigh less than 55 pounds. Operations must be directly performed or supervised by someone who has a remote pilot airman certificate with a small UAS pilot rating (Beal, 2017).

*New England Transportation Consortium (NETC)* (2021) provided guidance to New England State DOTs regarding effective practices when incorporating UAS into daily operations. The state DOTs included Massachusetts, Rhode Island, New Hampshire, Maine, Connecticut, and Vermont. NETC reviewed existing New England DOT operational manuals and policy directives to evaluate the adequacy of the guidelines against key requirements to support UAS missions. Also, NETC conducted implementation plans for six use cases based on information available from existing guidelines and case study interviews with New England State DOTs. These implementation procedures were derived from a holistic understanding of mission objectives, existing capabilities, and appropriate planning and operations strategies. The procedures acted as supplementary guidelines for the UAS use cases, along with the existing standard operating procedures and policy documents in place at the DOTs (Mallela et al., 2021)

*North Carolina Department of Transportation (NCDOT)* (2018) evaluated the suitability of using UASs to perform low-light collision scene reconstruction. The results showed that UASs could provide evidence-grade images in some low-light conditions when supplemented with appropriate external lighting equipment. Moreover, UASs could provide report-grade images that would add value to collision scene reports in most low-light conditions (Eyerman et al., 2018).

In 2020, *NCDOT* developed an agency authoritative guidance on UAS platforms, payloads, flight operations, and the UAS regulatory environment to use UAS for mapping wetlands along potential road corridors. The products of this research enabled the NCDOT to compare airframes and payloads, to estimate UAS operational costs, to plan and conduct regulatory compliant UAS flight operations, post-process data into useful forms, and rapidly and properly scope the potential for integrating UAS into wetland mapping efforts (Gray et al. 2020).

*New Hampshire Department of Transportation (NHDOT)* (2019) evaluated UAS applications on the specific needs of the NHDOT, including 1) different types of transportation projects that could be added by UAS, 2) the capabilities and limitations of utilizing UAS in various transportation projects, 3) the policies, procedures, staffing, and information technology infrastructure required for NHDOT to fully implement UAS technology. In this report, eight case studies, including accident reconstruction, airport runway and airport inspection, bridge inspection, construction monitoring, dam/emergency management, traffic monitoring, rail mapping and bridge inspection, and rock slope inspection, were implemented for the purpose of evaluating the applicability of UAS for NHDOT (O'Neil-Dunne and Estabrook, 2019).

*New York State Department of Transportation (NYSDOT)* (2017) presented the feasibility of applying automated systems, such as UASs and unmanned ground systems (UGSs), for transportation-related operations. NYSDOT discussed some studies and specifications of UASs for roadway mapping and showed some applications and specifications of UASs for structural systems monitoring, including confined spaces, bridges, and other transportation infrastructure. Also, the use of UASs for traffic monitoring was presented, such as monitoring of road and traffic conditions and management of traffic incidents. Finally, applications about applying UGSs on road construction improvement and work safety maintenance were discussed (Kamga et al., 2017).

*Oregon Department of Transportation (ODOT)* (2018) evaluated the effectiveness of inspecting bridges with small UAS. ODOT documented the capability and limitations from structural inspections with UAS. Also, ODOT investigated the utilization of UAS on some wireless communication tower inspections. The findings of this research were used in conjunction with data provided by ODOT to perform a cost-benefit analysis for the use of UAS in bridge inspection (Gillins et al., 2018).

In 2018, *ODOT* conducted another study to investigate the potential distraction caused by hovering a UAS cross a roadway to determine the distance from the edge of the roadway where UAS operation around the highway could degrade driving performance due to a visual and cognitive distraction. In this project, three independent variables were evaluated in a randomized, partially counterbalanced factorial experiment design focused on driver distraction caused by UAS operations near the roadway: 1) lateral offset, 2) flight path, and 3) land use. The results showed that the closer the UAS operation to the roadway, the longer drivers spent watching the UASs. Moreover, in rural environments, UAS operations could cause more distraction (Hurwitz et al., 2018).

*South Carolina Department of Transportation (SCDOT)* (2019) explored the benefits of UAS technology deployed at the SCDOT, specifically focusing on the areas of land surveying and bridge inspection. The results of a drone-based land survey experiment found that given common field conditions, survey points could be within 0.022 *ft* (XY), 0.003 *ft* (Z), and 0.048 *ft* (XYZ) of the true location. Moreover, this report also found that the computed stockpile volume estimates could range between 1.5% and 3.3% of actual. Also, using drones could more efficiently reduce the need for under-bridge inspection trucks, adequately documenting bridge conduction, keeping the bridge inspection engineers away from traffic, making the process nearly invisible to the traveling public, and reducing costs. This report also elaborated on a proof-of-concept experiment conducted to evaluate the possibility of inspecting a bridge remotely via a 4G cellular live stream broadcast (Bausman and Commert, 2019).

According to the state DOTs reports, digital cameras (often known as RGB cameras), LiDAR, and the thermal camera are widely used with UAS for different research purposes, including structure inspection, feasibility identification of UAS implementation for state DOT UAS operations, and testing the workflow for UAS usage. 21 out of 22 reports present the research conducted using RGB cameras. Compared to LiDAR and thermal cameras, UAS photogrammetry has a relatively low cost but provides high-resolution products.

Besides, UAS is popular in structure inspection, traffic monitoring and management, collision reconstruction, surveying, and mapping. UAS can be utilized in the structure inspection to check the quality of the structure, such as bridge inspection, building inspection, high mast tower inspection, and confined space inspection. Also, UAS can be applied to monitor the traffic and provide information for traffic management. Moreover, surveying and mapping, especially construction surveying and mapping, is another major area for UAS applications. UAS can be adopted in construction to survey and map the construction sites' terrains and estimate the earthwork and stockpile volumes. Furthermore, UAS can monitor the construction progress and track changes by capturing pictures from different times.

Thus, generating consistent results and ensuring the UAS data quality in preconstruction and construction is essential.

### 2.3 UAS Accuracy Documents

This section presents three accuracy documents that are used to evaluate the UAS-based photogrammetric surveying data based on the NCDOT requirements. Those accuracy documents are 1) Federal Geographic Data Committee (FGDC) Geospatial Positioning Accuracy Standards Part 3: National Standard for Spatial Data Accuracy, 2) 21 North Carolina Administrative Code (NCAC) 56 .1606 Specifications for Survey, and 3) American Society for Photogrammetry and Remote Sensing (ASPRS) Positional Accuracy Standards for Digital Geospatial Data. Each of them is documented in detail in the following subsection.

### *2.3.1 Federal Geographic Data Committee (FGDC) Geospatial Positioning Accuracy Standards Part 3: National Standard for Spatial Data Accuracy*

The National Standard for Spatial Data Accuracy is suitable for fully georeferenced maps and digital geospatial data in either raster, point, or vector format. It is derived from sources such as aerial photographs, satellite imagery, and ground surveys. A common language for reporting accuracy is offered to facilitate the identification of spatial data for geographic applications. The purpose of this standard is to implement a statistical and testing methodology for estimating the positional accuracy of points on maps and in digital geospatial data with respect to georeferenced ground positions of higher accuracy. There are two ways to report the horizontal accuracy at a 95% confidence level in this accuracy standard: Case 1 and Case 2. Case 1 is computing accuracy according to National Standard for Spatial Data Accuracy (NSSDA) when the RMSE in easting and northing directions are equal. Case 2 is approximating circular standard error when RMSE in easting and northing directions are not equal. The vertical accuracy is reported at a 95% confidence level according to NSSDA.

### *2.3.2 21 North Carolina Administrative Code (NCAC) 56.1606 Specifications for Survey*

This document presents the specifications for topographic and planimetric mapping, including ground, airborne, and spaceborne surveys. This set of specifications classifies horizontal accuracy into five categories from Class AA to Class D and classifies vertical accuracy into three categories from Class A to Class C. Table 2.2 lists the specified class categories in horizontal and vertical directions.

**Table 2.2 Accuracy Categories**

| Directions | Class | Relative Accuracy |
|---|---|---|
| Horizontal | AA | $\leqslant$ 0.1 *ft* (0.033 *m*) |
| | A | $\leqslant$ 1.64 *ft* (0.5 *m*) |
| | B | $\leqslant$3.28 *ft* (1.0 *m*) |
| | C | $\leqslant$ 6.56 *ft* (2.0 *m*) |
| | D | $\leqslant$ 16.40 *ft* (5.0 *m*) |
| Vertical | A | < 0.10 times the square root of the number of miles run from the reference datum |
| | B | < 0.20 times the square root of the number of miles run from the reference datum |
| | C | < 0.30 times the square root of the number of miles run from the reference datum |

### *2.3.3 American Society for Photogrammetry and Remote Sensing (ASPRS) Positional Accuracy Standards for Digital Geospatial Data*

This accuracy standard specifies positional accuracy for digital orthoimagery digital planimetric data, and digital elevation data. Based on RMSE values, accuracy classes have been revised and upgraded from the 1990 standard to address the higher accuracies achievable with newer technologies. The standard also includes additional accuracies measurements, such as orthoimagery seam lines, aerial triangulation (AT) accuracy, LiDAR relative swath-to-swath accuracy, minimum Nominal Pulse Density (NPD), horizontal accuracy or elevation data, delineation of low confidence areas for vertical data, and the required number and spatial distribution of checkpoints according to the project area. Table 2.3 indicates the accuracy classes in both horizontal and vertical directions that are used in this research.

**Table 2.3 ASPRS Positional Accuracy Standards for Horizontal and Vertical Directions**

| Horizontal Accuracy (*cm*) | | | | | Vertical Accuracy Non-Vegetated Vertical Accuracy (NVA) (*cm*) | | |
|---|---|---|---|---|---|---|---|
| Class | $RMSE_X$ and $RMSE_Y$ | $RMSE_R$ | At the 95% Confidence Level | Approximate GSD of Source Imagery | Class | $RMSE_Z$ NVA | NVA at 95% Confidence Level |
| X-*cm* | ≤ X | ≤ 1.414*X | ≤ 2.448*X | | X-*cm* | ≤ X | ≤ 1.96*X |
| 0.63 | 0.63 | 0.9 | 1.5 | 0.31 to 0.63 | | | |
| 1.25 | 1.25 | 1.8 | 3.1 | 0.63 to 1.25 | 1.0 | 1.0 | 2.0 |
| 2.5 | 2.5 | 3.5 | 6.1 | 1.25 to 2.5 | 2.5 | 2.5 | 4.9 |

### *2.3.4 North Carolina Department of Transportation*

NCDOT accepts the abovementioned accuracy standards for evaluating the UAS-based photogrammetric surveying accuracy. FGDC Geospatial Positioning Accuracy Standards defines the process and methodology for testing geospatial product accuracy standards. It includes formulas and specifies higher-order surveys are necessary for a minimum of 20 independent checkpoints.

21 NCAC 56 .1606 sets forth the specifications for airborne surveys, including topographic mapping, planimetric mapping, photogrammetric mapping, and digital data production. Horizontal accuracy class definition is applicable if one chooses to adopt a class definition. The vertical accuracy class definition is applicable to control surveys, but it is not directly applicable to assessing the vertical accuracy of airborne surveys. Moreover, the horizontal accuracy class values have too large a range to define large-scale aerial survey data adequately.

Thus, ASPRS Positional Accuracy Standards incorporate the FGDC Geospatial Positioning Accuracy Standard process and methodology for assessing centimeter-level geospatial product accuracy. This standard is the primary standard used to assess geospatial product accuracy in this project.

## 2.4 Impact Factors of UAS-based Photogrammetric Surveying Accuracy

According to previous studies, numerous flight configuration impact factors can influence the accuracy of UAS-based photogrammetric surveying, including flight heights, image overlaps, UAS platforms, and GCP quantity and distributions. This section presents the related studies on the influence of impact factors on UAS-based photogrammetric surveying accuracy. Table 2.4 summarizes the research conducted by various authors and impact factors for accuracy checking. 40 articles from major journals in the related field are summarized. The following subsections discuss the impact factors that influence UAS-based photogrammetric surveying accuracy. In Table 2.4, the first column identifies the author of the research papers. The second column describes the nature of the research. The third major heading specifies the impact factors.

## Table 2.4 Overview of the Related Research

* F: Flight Height, G: GCP Quantity and Distribution, C: Camera Setting, I: Image Acquisition, M: Georeferencing Methods

| Authors | Research Description | Factors | | | | |
|---|---|---|---|---|---|---|
| | | F | G | C | I | M |
| Alfio et al., 2020 | Evaluate the impact of image formats and levels of JPEG compression in UAS-based photogrammetric accuracy. | | | | X | |
| Anders et al., 2020 | Evaluate the influence of flight height and area coverage orientations on the DSM and orthophoto accuracies for flood damage assessment. | X | | | | |
| Agüera-Vega et al., 2017b | Evaluate the impact of flight heights, terrain types, and GCP quantities on DSM and orthoimage accuracy in UAS-based photogrammetry. | X | X | | | |
| Agüera-Vega et al., 2017a | Evaluate the impact of GCP quantities on UAS-based photogrammetry DSM and orthoimage accuracies. | | X | | | |
| Barba et al., 2019 | Propose an algorithm to calculate the sparse point cloud roughness using associated angular interval. | | X | | | |
| Benassi et al., 2017 | Analyze the impact of UAS blocks and georeferencing methods on accuracy and repeatability. | | | | | X |
| Benjamin et al., 2020 | Evaluate the influence of additional GCPs on spatial accuracy when AT is applied for georeferencing. | | X | | | |
| Burdziakowski & Bobkowska, 2021 | Analyze the influence of photogrammetric process elements on the quality of UAS-based photogrammetric accuracy to identify artificial lighting at night. | | | X | | |
| B. T. Fraser & Congalton, 2018 | Provide a solution for data collection and processing of UAS application in a complex forest environment. | X | | | | |
| Catania et al., 2020 | Evaluate the impact of GNSS receivers of techniques features and working modes on positioning accuracy. | | | | | X |
| Domingo et al., 2019 | Evaluate the impact of image resolution, camera type, and side overlap on predicted biomass model accuracy. | | | X | X | |
| Ferrer-González et al., 2020 | Identify the GCP quantities and distributions to generate a high accuracy for a corridor-shaped site. | | X | | | |
| Gerke & Przybilla, 2016 | Evaluate the impact of cross flight patterns, GCP distributions, and RTK-GNSS on camera self-calibration and bundle block adjustment quality. | | X | | | X |
| Gindraux et al., 2017 | Evaluate the effect of the location and quantity of GCPs on UAS-based DSMs in Glaciers. | | X | | | |
| Harwin et al., 2015 | Evaluate the influence of camera calibration methods as well as quantities and distributions of GCPs on UAS photogrammetry accuracy. | | X | X | | |
| James et al., 2017 | Analyze the influence of the ground control quality and quantity on DEM accuracy using a Monte Carlo Method. | | X | | | |
| Jurjević et al., 2020 | Evaluate the influence of image block orientation methods on the accuracy of estimated forest attributes, especially the plot mean tree height. | | | | | X |
| Kalacska et al., 2020 | Analyze the influence of different UAS platforms on positional and within-model accuracies without GCPs. | | | | | X |
| Lee et al., 2021 | Evaluate the impact of flight height, image overlap, GCPs quantities and distribution, and time of survey on snow depth measurement. | X | X | | | |
| Losè et al., 2020 | Provide operational guidelines and best practices of direct georeferencing methods on positional accuracy. | | | | | X |
| Martínez-Carricondo et al., 2018 | Evaluate the impact of GCP quantities and distributions on UAS-based photogrammetry DSM and orthoimage accuracies. | | X | | | |
| Martinez et al., 2020 | Assess the influence of GNSS with PPK on the UAS-based accuracy in building surveying applications. | | | | | X |
| Oniga et al., 2018 | Provide a solution about the optimal GCP quantity to generate high precision 3D models. | | X | | | |
| Padró et al., 2019 | Evaluate the geometric accuracy of using four different georeferencing techniques. | | | | | X |
| Ridolfi et al., 2017 | Provide information on the optimal GCP deployment for dam structures and high-rise structures. | | X | | | |
| Ruzgiene et al., 2015 | Assess the influence of numbers of GCPs on DSM accuracy. | | X | | | |
| Sanz-Ablanedo et al., 2018 | Analyze the influence of the quantities and numbers of GCPs on 3D model accuracy. | | X | | | |
| Seifert et al., 2019 | Provide scientific evidence of the impact of flight height, image overlap, and image resolution on forest area reconstruction. | X | | | X | |
| Stott et al., 2020 | Analyze the influence of GCP quantities on UAS photogrammetric mapping accuracy using the RTK-GNSS system. | | X | | | |
| Taddia et al., 2020 | Evaluate the quality of photogrammetric models and DTMs using PPK and RTK modes in coastline areas. | | | | | X |
| Tomaštík et al., 2019 | Assess the influence of RTK/PPK on geospatial accuracies of photogrammetric products in forest areas. | | | | | X |
| Tomaštík et al., 2017. | Assess the influence of different grades of tree covers and GCP quantities and distributions on UAS-based point clouds in forest areas. | | X | | | |
| Toth et al., 2015 | Evaluate the influence of camera sensor types and configurations and SfM processing tools on UAS mapping accuracy. | | | X | | |
| Wang et al., 2019 | Assess the impact of flight height, image overlap, GCP quantities, and construction site conditions on measurement accuracy. | X | X | | X | |
| Yang et al., 2016 | Evaluate the influence of low-height UAS photogrammetry systems on stable images, data processing, and accuracy. | | | | X | |
| Yu et al., 2020 | Analyze 3D model and DSM accuracies to determine the optimal GCP quantities in various terrain types. | | X | | | |
| Zimmerman et al., 2020 | Analyze the impact of flight heights and quantities and distribution of GCPs on survey error. | X | X | | | |
| Zhang et al., 2020 | Evaluate the impact of image parameters on the close-range UAS-based photogrammetric inspection accuracy. | | | | X | |
| Zhou et al., 2018 | Investigate three corridor aerial image block issues, including focal length error, a gradually varied focal length, and rolling shutter effects. | | | X | | |

### *2.4.1 Flight Heights*

Studies indicate that flight heights can impact the accuracy of the UAS-based photogrammetry. Fraser and Congalton (2018) demonstrated the impacts of flight height on SfM processing completeness. Three different flight heights were used, including 164 *ft*, 328 *ft*, and 394 *ft* above the forest canopy. The results showed that superior performance was generated using the 328 *ft* flight height.

Anders et al. (2020) conducted research to assess the accuracy of UAS image data using different flight heights (413-771 *ft*) in a semi-arid and medium-relief area with flood damage. The assessment was with respect to the mean absolute errors (MAE) of the vertical and horizontal accuracies of the generated digital surface model (DSM). The results indicated that the MAE in the vertical direction increased with an increase in flight heights, while the MAE in the horizontal direction remained stable.

### *2.4.2 Image Overlap*

Previous research showed that varying image overlaps could influence the accuracy of UAS-based photogrammetry. Lee et al. (2021) studied the influence of image overlap on the accuracy of UAV-photogrammetry-based snow depth distribution maps. This research applied three different image overlaps a 90% forward overlap by 81% side overlap, an 80% forward overlap by 72% side overlap, and a 70% forward overlap by 63% side overlap. The results demonstrated that accuracy would be improved when increasing the image overlap.

### *2.4.3 GCP Quantities and Distribution*

Previous research showed consistent results regarding the influence of the number and location of GCPs used to assess accuracy. Increasing the numbers of GCPs would improve accuracy in both horizontal and vertical directions. Also, well-distributed GCPs could generate more accurate results than using randomly distributed GCPs.

Research conducted by Barba et al. (2019) and Ruzgiene et al. (2015) determined that using GCPs would yield better accuracy than without using GCPs. Sanz-Ablanedo et al. (2018) conducted a study using 3465 different combinations of GCPs in BA to answer the question about the best placement of GCPs to achieve the desired accuracy. Results demonstrated that the accuracy achieved by using evenly distributed GCPs could be twice as high as using arbitrarily distributed GCPs and that utilizing the medium to high numbers of GCPs (such as 3 GCPs per 100 photos) could obtain the desired accuracy. Agüera-Vega et al. (2017a) investigated the impact of various numbers of ground control points on DSM and orthoimages. The numbers 4, 5, 6, 7, 8, 9, 10, 15, and 20 GCPs were adopted in the research. The optimal accuracy was derived using 15 or more GCPs. The generated accuracies from 15 and more GCPs had no noticeable difference.

### *2.4.4 Georeferencing Methods*

Besides the impact factors mentioned in the above subsections, some researchers also studied the other impact factor that affects UAS-based photogrammetric surveying accuracy, global navigation satellite systems (GNSS) with georeferencing methods. Catania et al. (2020) compared positional accuracy using various GNSS receivers for mapping in agriculture. Their study demonstrated that GNSS receivers carried out with an external antenna could yield better positioning accuracy.

### *2.4.5 Multiple Factors*

Out of those 40 papers, eight analyzed the influence of multiple impact factors on UAS-based photogrammetric surveying accuracy. None of them studied relative influences among these factors. Domingo et al. (2019) evaluated the impact of image resolution, camera type, and side overlap on the prediction accuracy of biomass terrain types using multiple linear regression models. Two different image resolutions (0.33 and 0.19 *ft* GSD), two camera types (NIR and RGB), and two different side overlap levels (70 and 80%) were assessed in their research. The results indicated that using the NIR camera could generate higher prediction errors than the RGB camera. A fine resolution improved the prediction accuracy regardless of the camera types. Also, increasing the side overlap decreased the prediction accuracy. However, there is no significant difference in image resolution, camera type, and side overlap on the accuracy of the 95% confidence level.

Wang et al. (2019) conducted research to assess the accuracy of the positional errors under various flight parameters, consisting of four flight heights (30 *ft* (18 *m*), 60 *ft* (27 *m*), 90 *ft* (37 *m*), and 150 *ft* (46*m*)), two overlaps (70% and 90%), six different quantities of GCPs (zero, one, four, eight, twelve, and sixteen) and varying construction materials (sand, clay, fine grade gravel, and coarse grade gravel). In their research, multiple comprehensive comparisons and multiple regression analyses were used to observe the significance of the impact factors. The results showed that increasing the numbers of GCPs and image overlap would improve the accuracy. Also, this research indicated that the quantity of GCPs had the most significant influence on the accuracy at a 95% confidential level. However, it was necessary to obtain a balance among all factors because no single factor is able to improve the accuracy if others do not also perform well.

Seifert et al. (2019) researched the influence of image overlap, flight height, and camera sensor resolution on accuracy using a multivariate generalized additive model to set flight parameters for UAS-based surveying in forest areas optimally. Five different flight heights ranging from 25m to 100m (82 *ft*, 131 *ft*, 164 *ft*, 246 *ft*, and 328 *ft*), four different image-side overlaps (67%, 55%, 45%, and 35%), and five various image resolutions (3840*2160 (100%), 2880*1620 (75%), 1920*1080 (50%), 960*540 (25%), and 768*432 (20%)) were utilized in this research. The results showed that low flight heights and high image overlaps could generate high accuracy with great reconstruction details and precision.

Agüera-Vega et al. (2017b) carried a case study to evaluate the influence of flight heights, terrain morphologies, and the number of GCPs on DSM and orthoimage accuracies. Five terrain morphologies, four flight heights (164 *ft*, 262 *ft*, 328 *ft*, and 394 *ft*), three different numbers of GCPs (3, 5, 10) were considered in this research. The results of this research indicated that the quantity of GCPs was the most important factor affecting both horizontal and vertical accuracies. Increasing the numbers of GCPs would improve both horizontal and vertical accuracies. However, the result of terrain morphology was the opposite. The terrain morphology did not influence either horizontal or vertical accuracies. Although flight height did not influence horizontal accuracy, it impacted vertical accuracy. Vertical accuracy decreased as flight altitude increased.

Zimmerman et al. (2020) conducted research using three different flight heights (220 *ft*, 299 *ft*, and 381 *ft*), six different quantities of GCPs (5, 7, 9, 11, 13, and 15), and nine different types of GCP distributions on DSM accuracy in a complex and developed coastline. The results indicated that both horizontal and vertical accuracies increased as flight heights or the number of GCPs increased. For the GCP distributions, the accuracy was highest when GCPs were located in the corner, both high and low elevations of the study site.

Harwin et al. (2015) performed research about the accuracy assessment of the quantities of GCPs and the camera calibration methods. Similar to other research, their results also showed that accuracy would be improved with increasing GCP quantities. Moreover, the results presented that when capturing nadir images, there was no noticeable difference between using pre-calibration and self-calibration. However, when processing oblique images, adopting self-calibration could yield higher horizontal accuracy than pre-calibration.

According to the above literature, most previous research focused on flight height, GCP quantities, and image overlap but not image quality and focal length of the camera lenses. Besides, most previous research simply assessed the accuracy through results comparisons using different impact factor values.

## 2.5 Discussion

### *2.5.1 UAS Applications*

Table 2.1 summarized the state DOT reports we reviewed by identifying the following:

1) The types of sensors used in the study,
2) The motivation for the research, and
3) The applications for which the UAS was used.

As previously summarized in Section 2.2 and Table 2.1, RGB cameras (non-metric) are the most widely used sensor equipped with UAS for various research purposes due to their low cost but high effectiveness. Moreover, UAS-based photogrammetry can be used in many research fields, including inspection, traffic monitoring and management, collision reconstruction, and construction surveying and mapping based on users' requirements.

### *2.5.2 Accuracy Standards*

ASPRS (2015) Positional Accuracy Standards is the most comprehensive standard for assessing geospatial product accuracy from airborne surveys. It incorporates the 1990 ASPRS Accuracy Standards for Large-Scale Maps and the 1999 FGDC Geospatial Positioning Accuracy Standard. Compared to accuracy classes in 21 NCAC 56 .1606, ASPRS (2015) Positional Accuracy Standards provides more detailed classifications on the centimeter levels.

### *2.5.3 UAS Impact Factors*

Section 2.4 indicates the impact factors that can influence the UAS-based photogrammetric surveying accuracy, including flight height, image overlap, GCP quantity and distribution, and georeferencing method used for data processing.

Flight height can impact accuracy. However, the influence of flight height on accuracy is not consistent since the utilized UAS platforms, site conditions, and environmental conditions are different. The results of the influence of GCP quantity and image overlap are consistent. Increasing the image overlap and the number of GCPs will improve the accuracy. Besides, using different georeferencing methods can also affect the accuracy.

Georeferencing methods can be classified into two groups: direct georeferencing method and indirect georeferencing methods. The direct georeferencing method does not require GCP and AT to process aerial photography into ground coordinates. Direct georeferencing using two devices, GPS and IMU.

GPS records the camera coordinates (X, Y, Z), and IMU records the camera orientation. Both parameters merged into exterior orientation parameters. For example, Real-Time Kinematic (RTK) and Post-Processing Kinematic (PPK) belong to direct georeferencing. Indirect georeferencing relies on known locations, such as coordinates. Thus, the indirect georeferencing method uses GCPs. According to research, using either indirect georeferencing or direct georeferencing methods can achieve the desired accuracy level.

# Chapter 3 Data Collection

To develop the guidelines, recommendations, and specifications, data collection and evaluation at different sites with various terrain types are essential. This chapter presents the data collections at six sites, including two preliminary test sites on the NCSU campus and four main test sites coordinated by NCDOT. Three different sensors were used to collect the data. Those sensors are UAS non-metric camera, terrestrial laser scanner (TLS), and Light Detection and Ranging (LiDAR). The following sections describe the specifications of the used sensors and the data collection information.

## 3.1 UAS, TLS, and LiDAR Specifications

This section introduces the specifications of UAS, TLS, and LiDAR used for data collection.

### *3.1.1 UAS Specifications*

DJI Inspire 2 with DJI Zenmuse X5S camera and Olympus M.Zuiko 25*mm* and 17*mm* focal length lenses were used for the UAS data collection (Figure 3.1). The resolution of the camera is 5280 x 3956 pixels. The pixel size is 3.28 x 3.28 $\mu m$.

**Figure 3.1 DJI Inspire II**

### *3.1.2 TLS Specifications*

Leica ScanStation P50 was used to collect the TLS data at the track facility and Lake Raleigh sites (Figure 3.2). This TLS is the newest premium member of the ScanStation P-series 3D terrestrial laser scanner that can maximize productivity by scanning inaccessible places at a safe position on site, reducing time in the field with fewer setups. The scanning of this TLS can cover up to 3,280 *ft* at 1 million points per second with a 360° horizontal and 290° vertical field of view (FOV). The measurement accuracy is around 3 *mm*.

**Figure 3.2 Leica ScanStation P50**

### *3.1.3 LiDAR Specifications*

MdLiDAR3000 LiDAR data collection was performed at the NCDOT coordinated four sites. Microdrones md4-3000 airframe with Riegl miniVUX-1UAV LiDAR sensor and Trimble APX20 IMU is used (Figure 3.3). The accuracy of mdLiDAR3000 LiDAR is from 0.033 to 0.098 ft for both horizontal and vertical directions.


**Figure 3.3 MdLiDAR3000 LiDAR**

## 3.2 Field Tests for Data Collection

For quick evaluation and preliminary study of geospatial products for non-metric sensors, the following two small sites at NCSU were chosen for a series of data collection - an open terrain with a facility and vegetation and an open terrain with a vertical structure and a lake. A UAS and a TLS were used to collect data from the preliminary sites on the NCSU campus.

The following four primary test sites were also larger and were arranged by NCDOT for data collection and evaluation - a facility site with open terrain filled with vegetation, two construction sites, and one rock slope site. At the latter sites, LiDAR data was also collected in addition to non-metric images. 40 data collections were performed at NCSU sites for building a prediction model that is detailed in

Appendix IV. Two data collections were performed at each primary test site at different times for various data evaluations – test of the MR model, GCP spacing analysis, and preparing specifications, recommendations, and guidelines. A UAS and LiDAR were used to collect data at the four primary test sites.

### *3.2.1 Track Facility Site on NCSU*

The first preliminary site was the track facility site on the NCSU campus, located in Raleigh, North Carolina. The size of this site is 1.21 *acres*. Two types of GCPs were used for the data collection - Propeller Aeropoints and the traditional surveying points (PK nails). Aeropoints produce high-precision GCPs more efficiently and cost-effectively than traditional surveys. They are GNSS-based receivers integrated GPS and precision post-processing, designed for use with small drones for fast, highly accurate photogrammetry-based surveying. Aeropoints are capable of recording hours of GNSS data to provide georeferencing corrections for surveying data with centimeter precision. This data is uploaded for processing by Propeller's proprietary PPK algorithms. Thus, Aeropoints can provide accurate results. The accuracy of Aeropoints can be within 0.1 *ft*. 10 traditionally surveyed points, and 15 Aeropoints were evenly distributed, as shown in Figures 3.4 and 3.5.

In addition to these target-based control points, TLS data (i.e., 3D laser scans) was collected by the NCDOT's Locations and Surveys Unit. The TLS data was used as additional checkpoints for data evaluation.

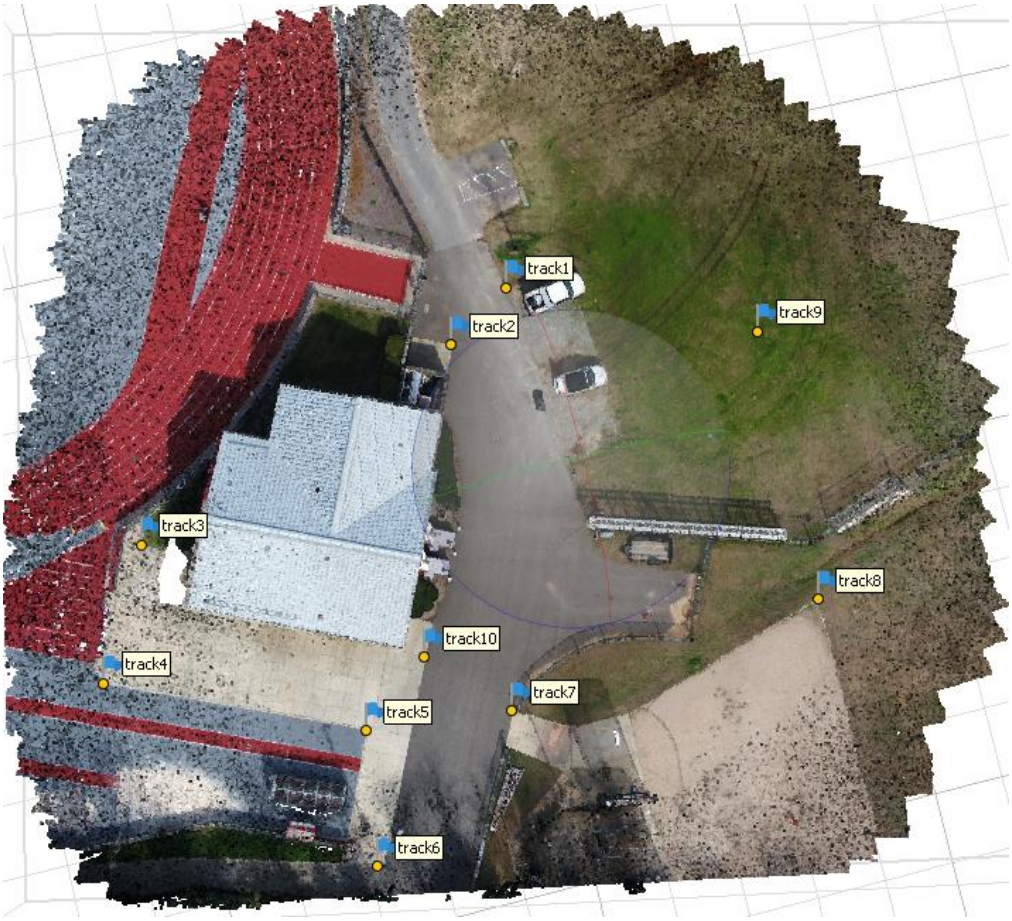


**Figure 3.4 Track Facility Surveying GCPs Layout**

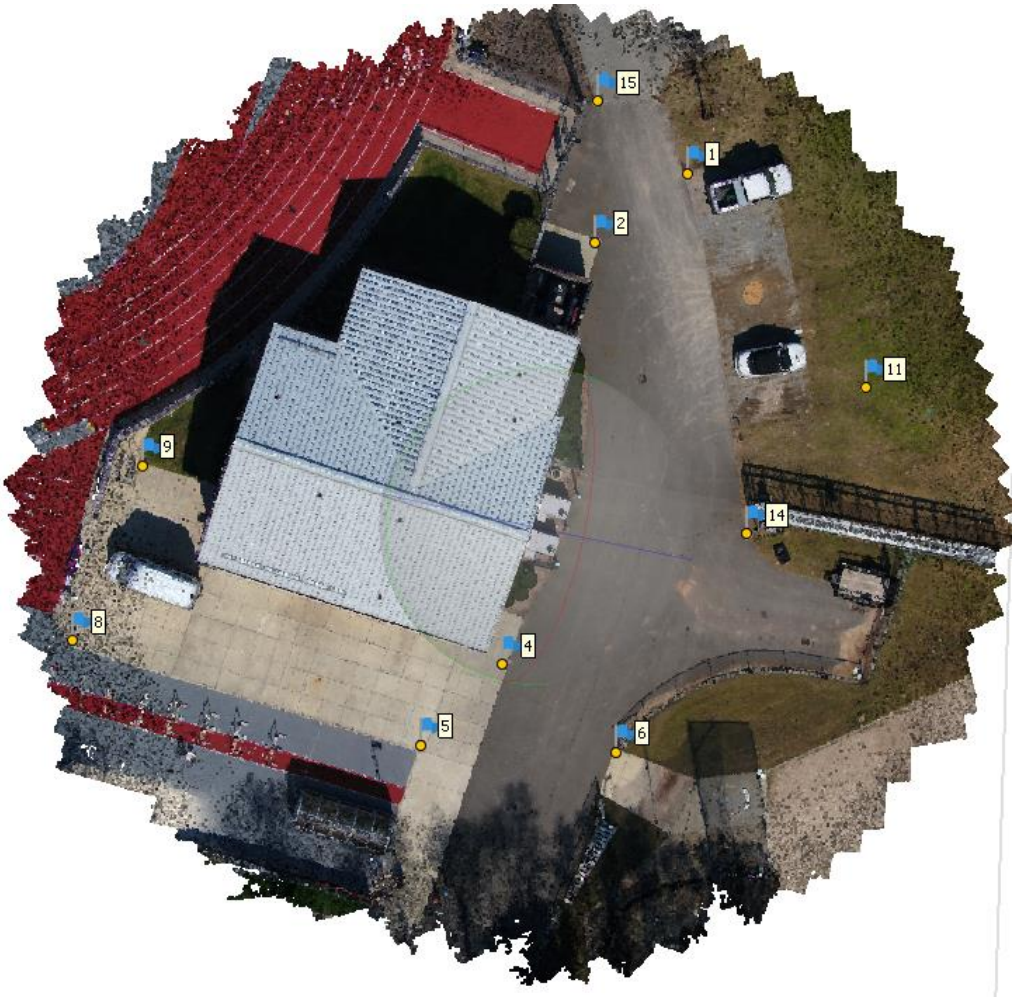


**Figure 3.5 Track Facility Aeropoints Layout**

To build the MR models, 40 flight missions were conducted at the track facility site from January 19th, 2021, to January 24th, 2021, with four different flight heights, five different image overlaps, two different focal lengths of lenses. The UAS image data was collected using a DJI Inspire II drone with a DJI Zenmuse X5S Camera and an Olympus M.Zuiko 25*mm* and 17*mm* focal length lenses. The following are the detailed flight configurations used to collect the data at the track facility site.

- Flight Heights: 40*m* (131*ft*), 50*m* (164*ft*), 60*m* (197*ft*), and 70*m* (229*ft*)
- Image Overlap: 50%, 60%, 70%, 80%, and 90%
- Focal Length: 17*mm* and 25*mm*

A total of 4425 images were collected for all flight missions. The number of collected images for every flight mission was from 20 to 539. The average image quality of every image data set was between 0.18 and 1.01. The quality of each image was calculated based on the comparison of the contrast gradients in the most peculiar areas between the original image and the Gaussian blur filter applied image through the Agisoft Metashape Estimate Image Quality tool. Table 3.1 lists those 40 flight missions with detailed information.

**Table 3.1 Flight Configuration at Track Facility Site**

| Flight No. | Focal Length (*mm*) | Flight Height (*m*) | Overlap (%) | Average Image Quality | Num. of Images |
|---|---|---|---|---|---|
| 1 | 25 | 40 | 90 | 0.88 | 539 |
| 2 | 25 | 40 | 80 | 0.23 | 161 |
| 3 | 25 | 40 | 70 | 0.30 | 94 |
| 4 | 25 | 40 | 60 | 0.22 | 57 |
| 5 | 25 | 40 | 50 | 0.96 | 48 |
| 6 | 25 | 50 | 90 | 0.29 | 473 |
| 7 | 25 | 50 | 80 | 0.90 | 156 |
| 8 | 25 | 50 | 70 | 0.24 | 64 |
| 9 | 25 | 50 | 60 | 0.63 | 48 |
| 10 | 25 | 50 | 50 | 0.25 | 39 |
| 11 | 25 | 60 | 90 | 0.60 | 391 |
| 12 | 25 | 60 | 80 | 0.34 | 86 |
| 13 | 25 | 60 | 70 | 0.95 | 47 |
| 14 | 25 | 60 | 60 | 0.28 | 30 |
| 15 | 25 | 60 | 50 | 0.18 | 22 |
| 16 | 25 | 70 | 90 | 0.32 | 120 |
| 17 | 25 | 70 | 80 | 0.40 | 98 |
| 18 | 25 | 70 | 70 | 0.31 | 39 |
| 19 | 25 | 70 | 60 | 0.33 | 30 |
| 20 | 25 | 70 | 50 | 0.58 | 20 |
| 21 | 17 | 40 | 90 | 0.49 | 345 |
| 22 | 17 | 40 | 80 | 1.01 | 148 |
| 23 | 17 | 40 | 70 | 0.48 | 55 |
| 24 | 17 | 40 | 60 | 1.01 | 46 |
| 25 | 17 | 40 | 50 | 0.63 | 35 |
| 26 | 17 | 50 | 90 | 0.92 | 321 |
| 27 | 17 | 50 | 80 | 0.37 | 77 |
| 28 | 17 | 50 | 70 | 0.37 | 48 |
| 29 | 17 | 50 | 60 | 0.63 | 31 |
| 30 | 17 | 50 | 50 | 0.63 | 21 |
| 31 | 17 | 60 | 90 | 0.43 | 226 |
| 32 | 17 | 60 | 80 | 0.63 | 85 |
| 33 | 17 | 60 | 70 | 0.65 | 48 |
| 34 | 17 | 60 | 60 | 0.92 | 28 |
| 35 | 17 | 60 | 50 | 0.51 | 23 |
| 36 | 17 | 70 | 90 | 0.49 | 171 |
| 37 | 17 | 70 | 80 | 0.40 | 75 |
| 38 | 17 | 70 | 70 | 0.50 | 30 |
| 39 | 17 | 70 | 60 | 0.39 | 30 |
| 40 | 17 | 70 | 50 | 0.42 | 20 |

### *3.2.2 Lake Raleigh Site on NCSU*

The second preliminary site was the Lake Raleigh site on the NCSU campus, located in Raleigh, North Carolina. The size of this site is 0.96 *acres*. 10 traditional surveying points were evenly distributed and used for the data collection. Figure 3.6 shows the layout of surveying GCPs.

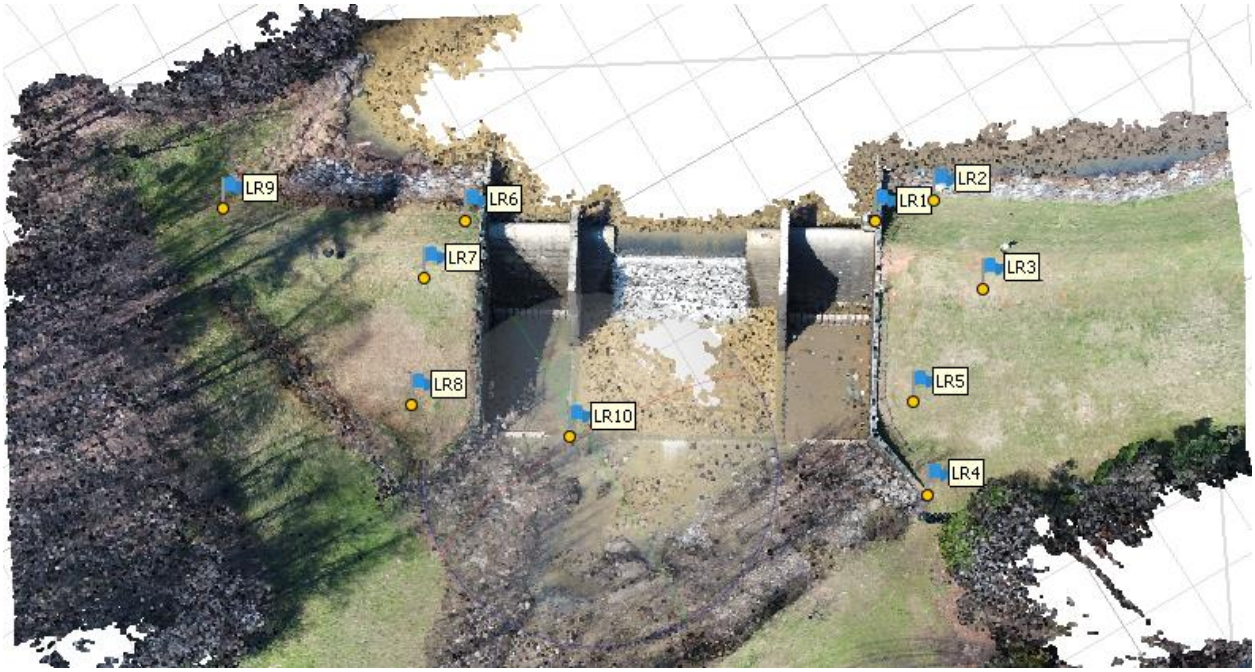


**Figure 3.6 Lake Raleigh Surveying Points Layout**

The UAS data was collected on February 9th, 2020, with different flight configurations using survey control points. Oblique images in different flight heights (262 *ft*, 230 *ft*, 197 *ft*, and 164 *ft*) were captured through automatic flights with circular paths using the Pix4D capture application. Nadir images in 328 *ft* flight height were captured through an automatic flight with a double grid path using the Pix4D capture application. Table 3.2 shows the detailed flight configurations.

**Table 3.2 Flight Configuration at Lake Raleigh Site**

| Flight No. | Flight Path | Flight Height (*ft*) | Camera Angle (°) | Image Overlap (%) | Focal Length (*mm*) | Num. of Images |
|---|---|---|---|---|---|---|
| 1 | Circular | 262 | 4 | - | 25 | 90 |
| 2 | Circular | 197 | 4 | - | 25 | 90 |
| 3 | Double Grid | 328 | - | 90 Forward & 80 Side | 25 | 63 |
| 4 | Circular | 230 | 4 | - | 17 | 90 |
| 5 | Circular | 164 | 4 | - | 17 | 90 |

In addition to these target-based control points, TLS data was collected by the NCDOT's Locations and Surveys Unit. The TLS data was used as additional checkpoints for data evaluation. In Lake Raleigh, a total of six setups were established to scan the sites.

### *3.2.3 Butner NCDOT/NCEM UAS Test Site*

The first NCDOT coordinated site was the Butner NCDOT/NCEM UAS Test site, located in Butner, North Carolina. The size of this site is 11.32 *acres*. 39 traditional surveying points were used in the project for data processing and evaluation shown in Figure 3.7.


**Figure 3.7 Butner Site Surveying Points Layout**

Two times data collection was performed on February 3rd, 2020, and February 25th, 2021, using survey control points. Nadir images were captured through an automatic flight with a single grid and a double grid path. Different flight configurations were used to collect the data. Table 3.3 shows the detailed flight configurations.

**Table 3.3 Flight Configuration at Butner Site**

| Time | Flight No. | Flight Path | Flight Height (*ft*) | Image Overlap (%) | Focal Length (*mm*) | Num. of Images |
|---|---|---|---|---|---|---|
| 02/03/2020 | 1 | Single Grid | 394 | 90 | 17 | 243 |
| 02/25/2021 | 2 | Double Grid | 380 | 90 | 25 | 684 |
| | 3 | Double Grid | 280 | 80 | 17 | 280 |

In addition, on March 17th, 2020, and March 8th, 2021, SDC visited the Butner site to collect data using LIDAR. They focused on the leaf-off area to investigate LiDAR penetration through trees. Different flight configurations were used to capture the LiDAR data. Table 3.4 lists the LiDAR flight configurations.

**Table 3.4 LiDAR Configuration at Butner Site**

| Time | Flight No. | Flight Height (*ft*) | Field of View (FOV) (°) | Overlap (%) |
|---|---|---|---|---|
| 03/17/2020 | 1 | 295 | 80 | 40 |
| | 2 | 295 | 56 | 40 |
| | 3 | 229 | 56 | 40 |
| 03/08/2021 | 4 | 197 | 56 | 60 |

### *3.2.4 U2412-A Construction Site*

The second NCDOT coordinated site was the U2412-A construction site, located in High Point, North Carolina. The size of this site is 34.67 *acres*. 10 Aeropoints and 24 traditional surveying points were used for the UAS data collection. Figure 3.8 shows the locations of Aeropoints and surveying GCPs on the site.

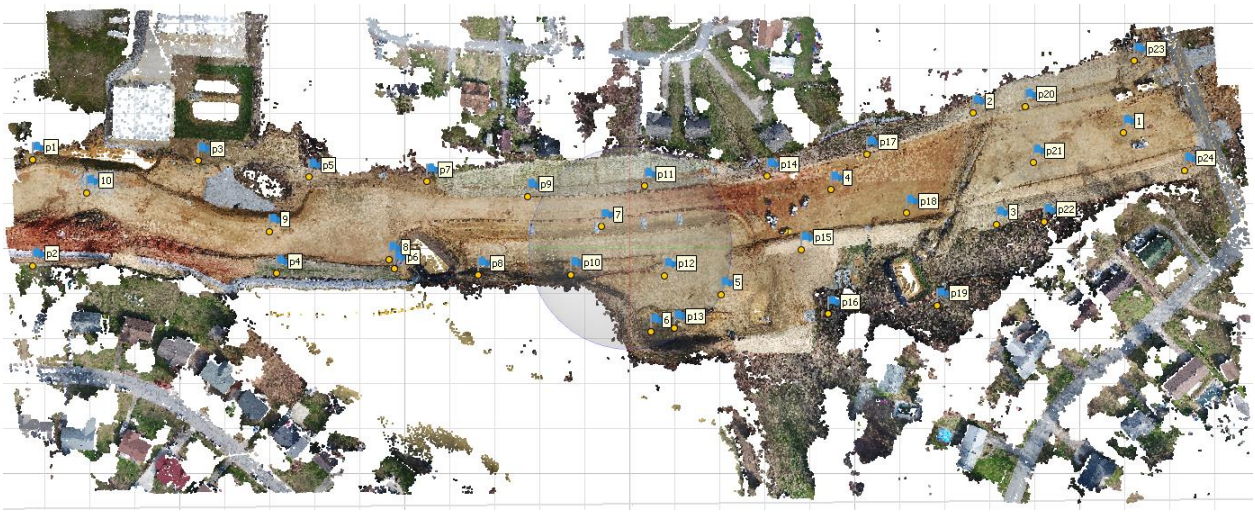


**Figure 3.8 U2412-A Construction Site Aeropoints and Surveying Points Layout**

The UAS data was collected on February 17th, 2020. Nadir images were captured with an 80% forward and an 80% side overlap using a 25 *mm* lens. The flight height was 361 *ft*. An automatic single grid path flight was performed using the Pix4D capture application. 203 images were captured.

Moreover, on February 17th, 2020, SDC visited the U-2414A construction site and collected the LiDAR data. Three different flight configurations were used to capture the LiDAR data. **Error! Reference source not found.**Table 3.5 lists the LiDAR flight configurations.

**Table 3.5 LiDAR Configuration at U2412-A Construction Site**

| Time | Flight No. | Flight Height (*ft*) | Field of View (FOV) (°) | Overlap (%) |
|---|---|---|---|---|
| 02/17/2020 | 1 | 295 | 80 | 50 |
| | 2 | 246 | 80 | 50 |
| | 3 | 197 | 80 | 50 |

### *3.2.5 R2303-E Pit Site*

The third NCDOT coordinated site was the R2303-E pit site, located in Clinton, North Carolina. The size of this site is 29.01 *acres*. 15 Aeropoints and 14 traditional surveying points were evenly distributed on the site.Figure **3.6 Lake Raleigh** Figure 3.9 shows the locations of Aeropoints and surveying GCPs on the site.


**Figure 3.9 R2303-E Pit Site Aeropoints and Surveying Points Layout**

The UAS data collection was performed on October 23rd, 2020, and November 21st, 2020. One set of data was collected using a 25 *mm* focal lens and a single grid at 400 *ft* (the highest flight for the drone) with 90% by 90% image overlap. Since the size of the site is large (29.01 *acres*), the Nadir images were captured through automatic flights with a single grid path using the Pix4D capture application. 1115 images and 1112 images were collected during two flight missions.

Additionally, the LiDAR data was collected on November 21st, 2020, by SDC. One set of data was collected using a 229 *ft* flight height, 60% overlap, and 80° FOV.

### *3.2.6 I-26 Rock Slope Site*

The last NCDOT coordinated site was the I-26 rock slope site, located in Mars Hill, North Carolina. The size of this site is 16.85 *acres*. 31 traditional surveying points were distributed on the site for UAS data collection. Figure 3.10 **Figure 3.6 Lake Raleigh** shows the locations of surveying GCPs on the site.

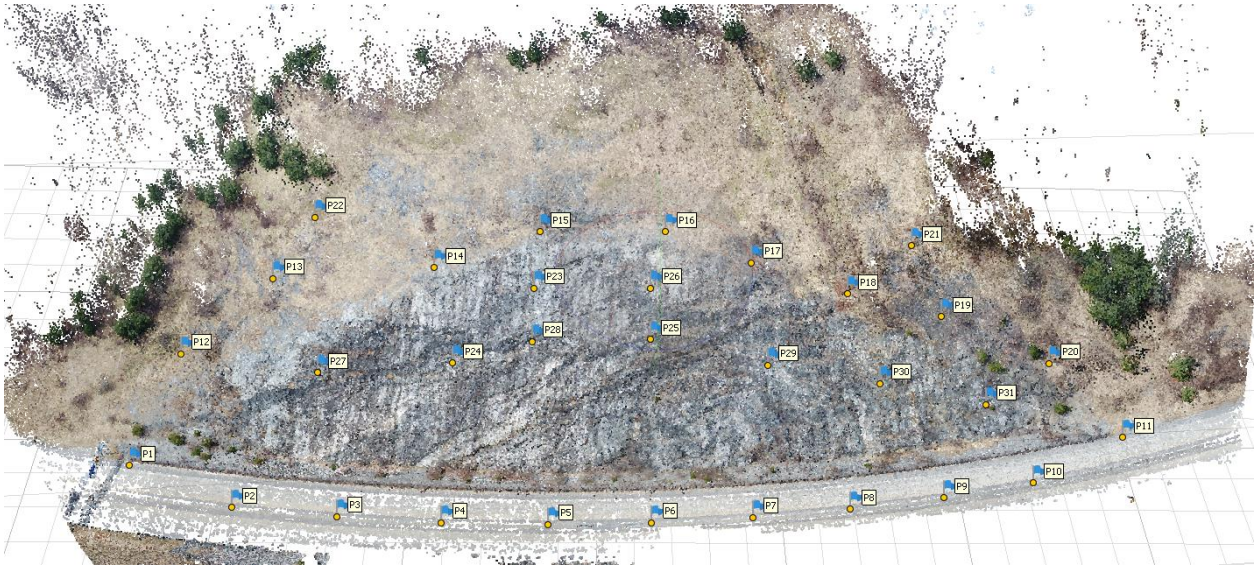


**Figure 3.10 I-26 Rock Slope Site Surveying Points Layout**

The UAS data collection was performed manually on September 30th, 2020, and March 9th, 2021. The data was manually collected since there was no autopilot mode or auto path for vertical surfaces. A 17 *mm* focal length of the lens was used to ensure sufficient image overlap. The image overlap was between 75% to 90%. On September 30th, 2020 and March 9th, 2021, the highest flight heights were 361 *ft* and 393 *ft*. 620 images and 729 images were collected on September 30th, 2020 and March 9th, 2021, respectively.

Also, the LiDAR data collection was performed manually on September 30th, 2020 and March 9th, 2021 by SDC. Two sets of data were collected on both data collection. Table 3.6 lists the LiDAR flight configurations.

**Table 3.6 LiDAR Configuration at I-26 Rock Slope Site**

| Time | Flight No. | Flight Height (*ft*) | Field of View (FOV) (°) | Overlap (%) |
|---|---|---|---|---|
| 09/30/2020 | 1 | 262 | 80 | 50 |
| 03/09/2021 | 2 | 262 | 56 | 60 |

# Chapter 4 Data Processing

This chapter describes the SfM commercial software products that were used for data processing. In consultant with the NCDOT, this research focused on three software products: Agisoft Photoscan, Pix4DMapper, and Trimble UASMaster.

## 4.1 Data Processing in Agisoft Photoscan

This section presents the workflow, and the parameters of Agisoft used for this research. 13 steps were involved in the data processing.

1. Import photos
2. Manually remove images that are obvious 'outliers' (e.g., images that have been taken before take-off, etc.)
3. Convert GPS coordinates of your geotagged images (WGS84) to match the coordinate system of GCPs, which will be imported later.
4. Estimate image quality.
    ***a.*** Disable all images that have an image quality below ***0.5***
5. Generate masks if necessary.
6. Align photos
    a. Quality ***HIGH***,
    b. Pair preselection: ***REFERENCE***,
    c. Key point limit: ***40,000***,
    d. Tie point limit: ***4,000***,
    e. Adaptive camera model fitting: ***YES***.
7. Import list of GCPs (also include the X/Y/Z accuracy values)
8. Verify and link markers to images (use FILTER BY MARKERS by right-clicking on GCP). Mark each GCP in at least 3-6 images. When finished, press the UPDATE button in the reference pane.
9. Uncheck all images in the reference pane and also uncheck checkpoints.
10. Clean sparse point cloud (MODEL > ***GRADUAL SELECTION***).
    a. Reprojection error: ***0.5,*** and
    b. Reconstruction uncertainty: **10**.
11. Adjust your bounding box
12. Optimize camera alignment (magic wand button)
13. Build dense cloud
    a. ***HIGH*** or ***MEDIUM*** quality

The coordinate used was NAD83 National Spatial Reference System 2011 (NAD83 (2011)/ North Carolina (ftUS)). As seen in Figure 4.1, for the camera calibration and optimization, the marker accuracy and camera accuracy were set as ***0.0164*** *ft* and ***0.065*** *ft*, respectively, based on the Agisoft Manual. The marker and tie point accuracies were set at ***0.1*** *pixels* and ***0.5*** *pixels*, separately (Agisoft, 2021).

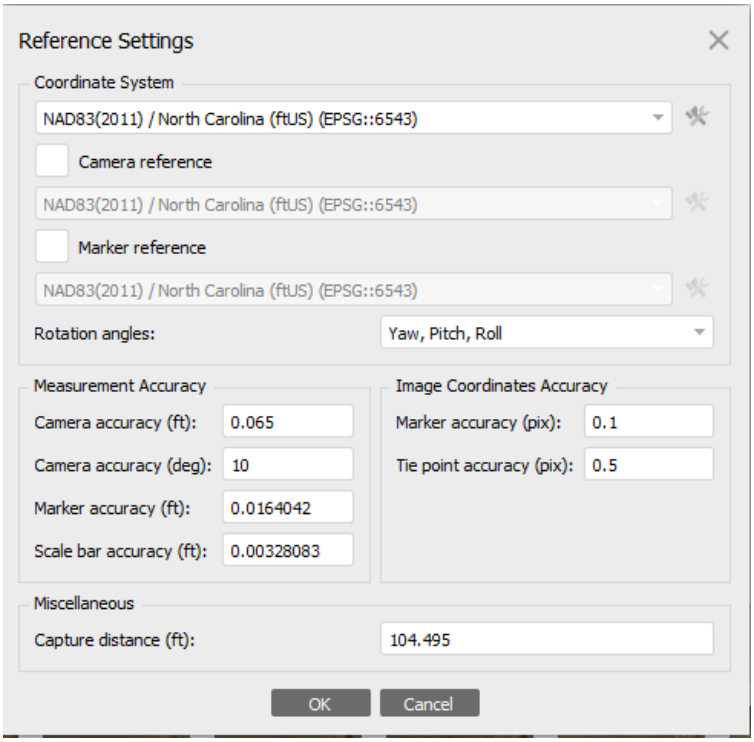


**Figure 4.1 Agisoft Setting**

## 4.2 Data Processing in Pix4DMapper

This section presents the workflow and the parameters of Pix4D used for this research. Five major steps were involved in the data processing.

1. Import Images and convert GPS coordinates of your geotagged images (WGS84) to match the coordinate system of GCPs, which will be imported later.
2. Import a list of GCPs (also include the X/Y/Z accuracy values) and link markers to images using Basic Editor.
3. Initial processing
    a. Targeted number of points as ***Automatic***,
    b. Calibration method as ***Standard***,
    c. Optimize ***all*** the internal and external parameters.
4. Manually removing or adding tie points (If necessary).
5. Build dense point cloud and mesh
    a. Use ***Original*** image scale,
    b. ***High*** point density, and
    c. Minimum number ***6*** of matching for point cloud densification.

With regard to the Pix4D, the coordinate used was NAD83 National Spatial Reference System 2011 (NAD83 (2011)/ North Carolina (ftUS)). Markers Accuracy for GCPs/Checkpoints was ***0.02*** *ft* (default setting), that was corresponding to the parameters of Agisoft.

## 4.3 Data Processing in Trimble UASMaster

This section presents the workflow and the parameters of the UASMaster used for this research. Five major steps were involved in the data processing based on the UASMaster manual.

1. Project preparation

    a. Import images.
    b. Import GCPs and checkpoints (also include the X/Y/Z accuracy values).
    c. Set the coordinate system of the project as the coordinate system of GCPs.
2. 3D reconstruction
    a. Extraction level: ***High*** or ***Highest*** based on the project
    b. Feature density: ***Normal Density***
    c. Distortion coefficients: ***Radial (K1-K3) & Decentering (P1 and P2)***
    d. ***Check*** Calibrate camera
3. Measure
    a. Link markers to images
4. Camera Calibration
    a. Principle point: ***Free***
    b. Focal length: ***Free***
    c. Distortion coefficients: number of symmetric radial distortion coefficients: ***3***
    d. Balance radial distortion: number of decentering distortion coefficients: ***2***
5. Generate Report

# Chapter 5 Data Evaluation

This chapter shows the results of UAS data processing using different software at the four NCDOT coordinated sites in both horizontal and vertical directions. The data evaluation results are based on the 21 NCAC 56 .1606 Specifications for Survey and ASPRS Positional Accuracy Standards for Digital Geospatial Data.

Based on 21 NCAC 56 specifications for surveying, horizontal accuracy is generally classified as five classifications from Class AA to Class D. Vertical accuracy is classified as three classifications from Class A to Class C. However, the horizontal accuracy class values have too large of a range to adequately define large-scale aerial survey data. Vertical accuracy classes listed in 21 NCAC 56 .1606 are based on ground survey techniques and cannot be applied to error measures such as RMSE or Non-Vegetated Vertical Accuracy (NVA) used for airborne surveying techniques. Thus, in 2015, ASPRS Positional Accuracy Standards for Digital Geospatial Data published new horizontal and vertical standards that combine the previous standards. The new standards can classify the horizontal and vertical accuracies on centimeter levels. However, this report still shows the horizontal accuracy in letter classes (Class AA to Class D according to 21NCAC document) per NCDOT request.

Moreover, the LiDAR data accuracy was assessed in the vertical direction. Additionally, two quantitative research methods used in this research to evaluate the results are presented. The first one is data evaluation of the influence of flight configuration impact factors on accuracy using multiple regression (MR) analysis. The second one is on the influence of distribution and separation distance on accuracy.

## 5.1 Data Evaluation at Butner NCDOT/NCEM UAS Test Site

Both UAS data and LiDAR data were evaluated at the Butner site. The checkpoints were used as independent points to check the positional accuracy of UAS 3D point model accuracy in horizontal and vertical directions under non-vegetation areas. LiDAR data was used to assess the positional accuracy under both vegetation and non-vegetation areas.

### *5.1.1 UAS Data Evaluation*

For flight 1 collected on February 3rd, 2020, 243 images with 19 GCPs and 20 checkpoints were used for data processing. A local coordinate system (NAD 1983 North Carolina State Plane US Feet 3200) was adopted. The GSD was 0.053 *ft* (1.63 *cm*). For flight 2 collected on February 25th, 2021, 684 images were collected and processed. 13 GCPs and 20 checkpoints were chosen. The average GSD was 0.052 *ft* (1.60 *cm*). For flight 3 collected on February 25th, 2021, 280 images were collected and processed. 12 GCPs and 20 checkpoints were chosen. The average GSD was 0.054 *ft* (1.65 *cm*). Table 5.1 lists the summarized results. The detailed information is available in Appendix I. The results show Class A for the horizontal accuracy for all three software. Also, the NVA 95% ranges from 0.125 *ft* to 0.149 *ft*.

**Table 5.1 Summarized Results of Butner Site**

| Time | Flight No. | Software | Horizontal Accuracy Class | Non-vegetated Vertical Accuracy 95% (*ft*) | RMSE R (*ft*) | Case 1 95% (*ft*) | Case 2 95% (*ft*) |
|---|---|---|---|---|---|---|---|
| 02/03/2020 | 1 | Agisoft | A | 0.135 | 0.069 | 0.120 | 0.115 |
| | | Pix4D | A | 0.140 | 0.074 | 0.127 | 0.127 |
| | | UASMaster | A | 0.149 | 0.079 | 0.136 | 0.136 |
| 02/25/2021 | 2 | Agisoft | A | 0.125 | 0.082 | 0.141 | 0.141 |
| | | Pix4D | A | 0.136 | 0.080 | 0.138 | 0.138 |
| | | UASMaster | A | 0.132 | 0.083 | 0.144 | 0.144 |
| | 3 | Agisoft | A | 0.131 | 0.084 | 0.145 | 0.144 |
| | | Pix4D | A | 0.136 | 0.081 | 0.140 | 0.140 |
| | | UASMaster | A | 0.139 | 0.081 | 0.141 | 0.141 |

### *5.1.2 LiDAR Data Evaluation*

For the Butner site LiDAR processing, 13 control points were used to merge all scans. The same set of checkpoints were used to assess the LiDAR accuracy. Regarding the data collected on March 08$^{th}$, 2021, 15 control points were used to process and merge all the scans. Table 5.2 lists the summarized accuracy results for LiDAR evaluation at the Butner site. Compared with UAV photogrammetry, LiDAR has higher accuracy in the Z direction, especially in the vegetation areas. The detailed results are available for review in Appendix I.

**Table 5.2 Summarized LiDAR Result at Butner Site**

| Time | Flight No. | Mean (*ft*) | Standard Deviation (*ft*) | RMSEZ (*ft*) | Non-vegetated Vertical Accuracy 95% (*ft*) |
|---|---|---|---|---|---|
| 03/17/2020 | 1 | -0.001 | 0.051 | 0.050 | 0.098 |
| | 2 | -0.004 | 0.057 | 0.056 | 0.109 |
| | 3 | -0.002 | 0.057 | 0.055 | 0.109 |
| 03/08/2021 | 4 | -0.05 | 0.039 | 0.038 | 0.074 |

## 5.2 Data Evaluation at U2412-A Construction Site

Both UAS data and LiDAR data were evaluated at the U2412-A construction site. The checkpoints were used as independent points to check the positional accuracy of UAS 3D point model accuracy in horizontal and vertical directions under non-vegetation areas. LiDAR data was used to assess the positional accuracy under both vegetation and non-vegetation areas.

### *5.2.1 UAS Data Evaluation*

For the UAS data processing, 203 images with 4 GCPs and 20 checkpoints were used during the data processing. A local coordinate system (NAD 1983 North Carolina State Plane US Feet 3200) was adopted. The GSD was 0.053 *ft* (1.63 *cm*). Table 5.3 lists the summarized results. The detailed information is available in Appendix I.

**Table 5.3 Summarized Results of U2412-A Construction Site**

| Time | Flight No. | Software | Horizontal Accuracy Class | Non-vegetated Vertical Accuracy 95% (*ft*) | RMSE R (*ft*) | Case 1 95% (*ft*) | Case 2 95% (*ft*) |
|---|---|---|---|---|---|---|---|
| 02/17/2020 | 1 | Agisoft | A | 2.421 | 0.183 | 0.317 | 0.297 |
| | | Pix4D | A | 2.242 | 0.169 | 0.293 | 0.271 |
| | | UASMaster | A | 2.669 | 0.199 | 0.344 | 0.343 |

### *5.2.2 LiDAR Data Evaluation*

Regarding the data collected on February 17th, 2020, 26 control points were used to merge all scans. Unlike photogrammetry, there is no optimization and/or change of points adjustment using control points. Thus, control points were simply used for merging each scan into a single model. The following accuracies were calculated using 20 checkpoints. Table 5.4 lists the summarized accuracy results for LiDAR evaluation at the U2412-A construction site. Compared with UAV photogrammetry, LiDAR has higher accuracy in the Z direction, especially in vegetation areas. The detailed results are available for review in Appendix I.

**Table 5.4 Summarized LiDAR Result at the U2412-A Construction Site**

| Flight No. | Mean (*ft*) | Standard Deviation (*ft*) | RMSEZ (*ft*) | Non-vegetated Vertical Accuracy 95% (*ft*) |
|---|---|---|---|---|
| 1 | -0.004 | 0.073 | 0.072 | 0.140 |
| 2 | -0.006 | 0.063 | 0.062 | 0.122 |
| 3 | -0.015 | 0.052 | 0.053 | 0.104 |

## 5.3 Data Evaluation at R-2303 E Pit Site

This section describes the data evaluation results for the R-2303 E pit site collected on both dates for UAS and LiDAR.

### *5.3.1 UAS Data Evaluation*

1115 images were collected from October 23rd, 2020, and processed using the three software. 13 points were used as GCPs with 20 checkpoints during the data processing. GSD was 0.0663 *ft* (2.02 *cm*). 1112 images were collected on November 21st, 2020, and processed using the three software. Nine GCPs were chosen. GSD was 0.0672 *ft* (2.05 *cm*). The results for 20 checkpoints were summarized in Table 5.5. The results show Class A for horizontal accuracy. The NVA 95% is between 0.133 *ft* and 0.180 *ft*. The detailed preliminary results are available in Appendix I.

**Table 5.5 Summarized Checkpoints Accuracy at the R-2303 E Pit Site**

| Time | Flight No. | Software | Horizontal Accuracy Class | Non-vegetated Vertical Accuracy 95% (*ft*) | RMSE R (*ft*) | Case 1 95% (*ft*) | Case 2 95% (*ft*) |
|---|---|---|---|---|---|---|---|
| 10/23/2020 | 1 | Agisoft | A | 0.133 | 0.070 | 0.120 | 0.120 |
| | | Pix4D | A | 0.136 | 0.077 | 0.134 | 0.134 |
| | | UASMaster | A | 0.145 | 0.082 | 0.141 | 0.140 |
| 11/21/2020 | 2 | Agisoft | A | 0.165 | 0.086 | 0.149 | 0.148 |
| | | Pix4D | A | 0.173 | 0.092 | 0.159 | 0.159 |
| | | UASMaster | A | 0.180 | 0.079 | 0.138 | 0.136 |

### *5.3.2 LiDAR Data Evaluation*

To avoid any confusion and satisfy NCDOT's interest in a direct comparison of accuracy between LiDAR and photogrammetry, the NCSU team has coordinated with SDC to use the same set of control points and checkpoints (refer to Appendix I). Twelve control points and 20 checkpoints were used. The mean and standard deviation of an elevation difference of checkpoints is -0.080 *ft* and 0.070 *ft*. The RMSE Z of control points is 0.105 *ft*, and the NVA at 95% is 0.207 *ft*. The detailed results are available for review in Appendix I.

## 5.4 Data Evaluation at I-26 Rock Slope Site

This section describes the data evaluation results for the I-26 rock slope site collected on both dates for UAS and LiDAR.

### *5.4.1 UAS Data Evaluation*

620 images collected on September 30th, 2020, were processed using Agisoft, Pix4D, and UASMaster. The average ground sample distance (GSD) was 0.069 *ft* (2.10 *cm)* with the range from 0.031 *ft* (0.94 *cm*) to 0.126 *ft* (3.85 *cm*). 729 images collected on March 09th, 2021, were processed using Agisoft, Pix4D, and UASMaster. The average GSD was 0.067 *ft* (2.04 *cm),* ranging from 0.020 *ft* (0.62 *cm*) to 0.175 *ft* (5.34 *cm*).

The control points on the panel pavement were observed using a virtual reference station (VRS) due to safety reasons. Thus, there was a 0.122 ft bias between the VRS observed elevations and the static scan elevations using a total station. Moreover, all other panel points' elevations were established using a total station and are more accurate than the VRS observed elevations. To reduce the influence of the 0.122 *ft* bias between the VRS observed elevations and the static scan elevations at panel points, the GPS observed coordinates were used as horizontal coordinates and used static scan elevations instead of VRS observed elevations vertical coordinates. Thus, the panel points were treated as full control points resulting in a total of 20 checkpoints. The overall results for all checkpoints are summarized in Table 5.6.

The results show Class A quality for the horizontal accuracy. There is no obvious difference among the results obtained from the three software. Compared with the September 30th, 2020, data collection results at the I-26 Rock Surface, the March 9th, 2021, results improved since the accuracy of the checkpoints on the road increased.

**Table 5.6 Summarized Checkpoint Accuracy at the I-26 Rock Surface Site**

| Time | Flight No. | Software | Horizontal Accuracy Class | Non-vegetated Vertical Accuracy 95% (*ft*) | RMSE R (*ft*) | Case 1 95% (*ft*) | Case 2 95% (*ft*) |
|---|---|---|---|---|---|---|---|
| 09/30/2020 | 1 | Agisoft | A | 0.326 | 0.154 | 0.267 | 0.266 |
| | | Pix4D | A | 0.288 | 0.179 | 0.311 | 0.310 |
| | | UASMaster | A | 0.424 | 0.170 | 0.295 | 0.294 |
| 03/09/2021 | 2 | Agisoft | A | 0.113 | 0.077 | 0.133 | 0.133 |
| | | Pix4D | A | 0.118 | 0.075 | 0.131 | 0.130 |
| | | UASMaster | A | 0.119 | 0.079 | 0.137 | 0.137 |

Table 5.7 summarizes the results from both flights data collection. The accuracy for the checkpoints on the road increased because the reprojection images of the points on the road (collected this time) increased from 5 images (collected for the first site visit) to at least 20 images. The results show that the number of reprojection images could significantly impact the accuracy. Increasing the number of reprojection images of the points can increase the accuracy in both horizontal and vertical directions. The error is high (>0.5 *ft* in the vertical direction) if the reprojection image numbers are less than 5. The detailed preliminary results are available in Appendix I. This lesson is related to the guidelines of GCP displacement, which is presented in Appendix II.

**Table 5.7 Summarized Checkpoint Accuracy both at the I-26 Rock Surface Site on September 30th, 2020, and March 9th, 2021**

| Checkpoint Area | Software | Data Collection Time | Horizontal Accuracy Class | Non-vegetated Vertical Accuracy 95% (*ft*) | RMSE R (*ft*) | Case 1 95% (*ft*) | Case 2 95% (*ft*) |
|---|---|---|---|---|---|---|---|
| Whole Area | Pix4D | 09/30/2020 | A | 0.288 | 0.179 | 0.311 | 0.310 |
| | | 03/09/2021 | A | 0.118 | 0.075 | 0.131 | 0.130 |
| | Agisoft | 09/30/2020 | A | 0.326 | 0.154 | 0.267 | 0.266 |
| | | 03/09/2021 | A | 0.113 | 0.077 | 0.133 | 0.133 |
| | UASMaster | 09/30/2020 | A | 0.424 | 0.170 | 0.295 | 0.294 |
| | | 03/09/2021 | A | 0.119 | 0.079 | 0.137 | 0.137 |
| Checkpoints above the Road (Area 1 in Figure 9.16) | Pix4D | 09/30/2020 | A | 0.113 | 0.092 | 0.159 | 0.159 |
| | | 03/09/2021 | A | 0.111 | 0.077 | 0.133 | 0.133 |
| | Agisoft | 09/30/2020 | A | 0.083 | 0.086 | 0.149 | 0.149 |
| | | 03/09/2021 | A | 0.127 | 0.071 | 0.123 | 0.123 |
| | UASMaster | 09/30/2020 | A | 0.103 | 0.091 | 0.158 | 0.158 |
| | | 03/09/2021 | A | 0.104 | 0.079 | 0.136 | 0.136 |
| Checkpoints on the Road (Area 2 in Figure 9.16) | Pix4D | 09/30/2020 | A | 0.462 | 0.276 | 0.478 | 0.477 |
| | | 03/09/2021 | A | 0.129 | 0.072 | 0.125 | 0.124 |
| | Agisoft | 09/30/2020 | A | 0.539 | 0.207 | 0.358 | 0.348 |
| | | 03/09/2021 | A | 0.079 | 0.078 | 0.135 | 0.135 |
| | UASMaster | 09/30/2020 | A | 0.690 | 0.261 | 0.451 | 0.450 |
| | | 03/09/2021 | A | 0.143 | 0.079 | 0.137 | 0.136 |

### *5.4.2 LiDAR Data Evaluation*

Regarding the data collected on September 30th, 2020, 29 control points were used to merge all scans. Unlike photogrammetry, there is no optimization and/or change of points adjustment using control points. Thus, control points were simply used for merging each scan into a single model. Regarding the data collected on March 09th, 2021, 11 control points were used to merge all scans. The following accuracies were calculated using 20 checkpoints. Table 5.8 summarizes the LiDAR results at the I-26 rock slope site. The detailed results are available for review in Appendix I. Compared with UAV photogrammetry, LiDAR has higher accuracy in the Z direction for the rock surface surveying.

**Table 5.8 Summarized LiDAR Result at the I-26 Rock Slope Site**

| Time | Flight No. | Mean (*ft*) | Standard Deviation (*ft*) | RMSEZ (*ft*) | Non-vegetated Vertical Accuracy 95% (*ft*) |
|---|---|---|---|---|---|
| 09/30/2020 | 1 | -0.070 | 0.098 | 0.119 | 0.233 |
| 03/09/2021 | 2 | 0.028 | 0.064 | 0.068 | 0.133 |

## 5.5 LiDAR Point Cloud Penetration Analysis

The NCSU team analyzed the LiDAR penetration through trees for the Butner data using MATLAB, ArcGIS Pro, and CloudCompare (3D point cloud visualization software). Since the ground in the Butner site is on a slope, to better analyze the penetration of the LiDAR, the NCSU Research team selected four study areas in different locations in the tree area. According to the results, the average point density is 1.25 *point/sq.ft*, and the standard deviation is 0.15 *point/sq.ft*. There is no obvious difference in ground point density in various locations. The detailed information is available in Appendix I.

### 5.6 Multiple Regression Analysis of Impact Factors on Accuracy

The NCSU team has identified the relationships among different configuration factors on the UAS-based photogrammetric survey accuracy. The influence factors included flight height, average image quality, flight overlap, GCP numbers, and focal length.

The results show that image overlap and GCP quantity have more significance than other impact factors on vertical accuracy. Image overlap has greater significance than other impact factors on horizontal accuracy. The detailed information is available in Appendix IV.

### 5.7 Ground Control Points Quantity and Spacing Evaluation

This research aims to analyze the influence of numbers and spacing of GCPs on different levels of accuracy for preconstruction and construction sites. The Butner and U2412-A construction sites' UAS and LiDAR data were used in this research. Three different numbers of GCPs with various separation distances were used at Butner (4, 6, and 9 GCPs) and U2412-A construction sites (4, 6, and 8 GCPs).

The results showed that GCP spacing has a direct impact on the local accuracies. This finding indicates that GCP spacing needs to be carefully considered when determining the number of GCPs. For example, the research team had to fly near the maximum allowed flight height – 361 *ft* because the site was large. For this site, GCP spacing of 262 *ft* or less can yield the horizontal and vertical accuracies of 3 GSD. These research findings were limited to the flight heights and hardware from the test sites (therefore, specific GSD). NCDOT can build its own GCP spacing data with varying GSD values using the details of this study in Appendix V.

## Chapter 6 Identify Causes of Inconsistencies and Develop Ways to Mitigate Risk

This chapter introduces the identified causes of inconsistencies. Also, ways to mitigate the risks are developed. The causes consist of camera calibration, image quality, camera exposure parameters, motion blur, the number and distribution of GCPs, site conditions, weather conditions, and light conditions. The recommendations for mitigating the causes of inconsistencies are included in Appendix I: Guidelines and Recommendations for UAS-based Photogrammetric Surveying Accuracy.

1. Camera Calibration:
   There are two ways to calibrate cameras: pre-calibration before the mission for each camera or calibration as part of structure-from-motion (SfM). When pre-calibration is performed, all camera settings should be fixed. Any change to the fixed camera settings (including autofocus and zoom) can cause inconsistent results. If autofocus is used or if camera settings will be changed during flight or after calibration is performed, calibration during SfM should be used. Moreover, pre-calibration should be performed multiple times to make sure that consistent intrinsic parameters are achieved.

2. Image Quality:
   Image quality can also affect the consistency of results. Images with poor quality can significantly influence alignment results. For example, Figure 6.1 shows the same maker from two images with different quality values (0.923 and 0.575) from Agisoft. The quality value is calculated based on the sharpness level of the most focused part of the picture. Picking the GCP location of the target from images with poor quality can be easily off by a few pixels. Thus, poor-quality images should be excluded from photogrammetric processing. Moreover, if the software does not automatically identify image qualities, the user should manually inspect images to identify and remove low-quality images.

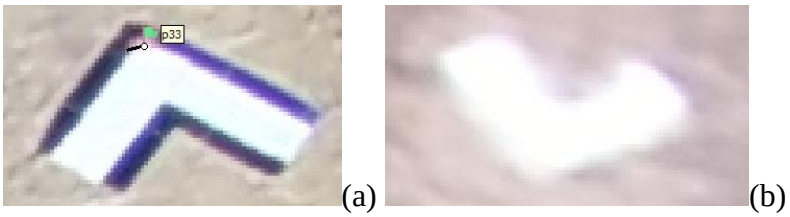

(a) (b)

**Figure 6.1 Zoom-in Images with Different Quality Values**

3. Camera Exposure Parameters:
   The camera exposure parameters (i.e., shutter speed, lens aperture, and International Organization for Standardization (ISO) values) considerably impact image quality. Thus, high shutter speed and different ISO values should be chosen to ensure image quality depending on weather and lighting conditions.

4. Motion Blur:
   A level of motion blur will inversely affect the accuracy of the measurement. However, small quantities of blur did not significantly affect the accuracy as long as the target was detected and successfully measured. What really matters are GSD and selection errors that may happen due to blurriness. The selection error in pixel times GSD gives the selection error in real-world units (i.e., inches, cm, etc.). Therefore, the expected selection error in the real-world unit should give the surveyor/pilot an expected maximum accuracy.

5. The Number and Distribution of Ground Control Points:
   The number and distribution of GCPs can influence the AT and eventually affect the accuracy of results. The accuracy results will be improved if the number of GCPs is increased. Moreover, evenly distributing the GCPs can guarantee the reliability of the point cloud.

   Thus, when possible, using enough GCPs and evenly distributing them can generate reliable results.

6. Site Conditions:
   Site conditions can also affect accuracy. The results at different sites (of different sizes) with the same number and distribution of GCPs can differ. For example, the results of using 4 GCPs at the track facility site and at the U2412-A construction site are different. The U2412-A construction site resulted in relatively poor accuracy when the same number of GCPs were used.

   Thus, suitable flight configurations should be designed, taking site conditions into consideration.

7. Weather Conditions:
   Some weather conditions, such as windy weather, can worsen accuracy. Ultra-lightweight drone platforms are especially prone to wind and vibration problems. Wind during the data acquisition activity can cause imprecise image recording direction and, eventually, insufficient image overlap. Moreover, wind can lead to vibration from the UAV's rotor-engine and shifter, which increases the image blurriness.

   Thus, the flight mission should be conducted under ideal weather conditions. If flying under less than ideal conditions, image quality should be checked after each flight to ensure its quality. If needed, more flights may be necessary to make sure the site being surveyed is sufficiently covered with good quality images. Blurry images should not be included for SfM.

8. Light Conditions:
   Lighting conditions may also cause inconsistent results. Glare and dark images can affect feature detection, and matching and they can also affect the number of automatic tie points. The camera setting should be adjusted to ensure good quality images under different lighting conditions.

# Chapter 7 Conclusions

UAS and photogrammetry technologies are widely used together for various civil engineering applications due to their cost-effectiveness, efficiency, and ability to generate survey-grade surveying. However, they often generate inconsistent and unreliable surveying results when using "black box" commercial software. Moreover, there are no guidelines to guarantee data quality. Therefore, this research focused on developing a comprehensive set of guidelines, specifications, and recommendations for producing survey-grade geospatial products using UAS solutions for applications in preconstruction, construction, and sloped sites.

The guidelines will enable NCDOT to produce more reliable and consistent survey results and evaluate them for potential improvement on accuracy. The specifications will enable NCDOT to estimate reasonable survey accuracy given a set of hardware and site constraints.

Moreover, an MR model was developed to evaluate the level of significance of five main flight configuration factors on accuracy. Those five impact factors were flight height, image overlap, GCP quantity, the focal length of the camera lens, and average image quality. Furthermore, the MR model was used to predict survey accuracy. For NCDOT to implement, they will have to build their own may model using their own set of hardware. Additionally, research on the influence of GCP spacing and quantity on survey accuracy was conducted using different numbers of and distances between GCPs.

The following conclusions are made based on the research findings.

- GSD, the accuracy of GCP coordinates, and accuracy GCP selection in SfM software dictate the maximum accuracy.
- The maximum accuracy in horizontal and vertical directions is expected of 1 to 3 GSD.
- The maximum accuracy is also limited by the accuracy of GCP coordinates, which depend on the type of surveying equipment used.
- NCDOT may benefit from building its own MR model for predicting the expected accuracy on horizontal and vertical directions on various terrains.
- Among five impact factors, image overlap has the highest-level significance in both horizontal and vertical directions. GCP quantity has a greater influence on vertical direction.
- GCP spacing affects surveying accuracy. The number of GCPs needs to be determined by considering the maximum spacing that will allow the desired maximum accuracy. For example, GCP spacing for a flight height of 361 *ft* and 25 *mm* camera should be equal to or less than 262 *ft* in order to achieve the accuracy of 3 GSD.

This research was a systematic approach to the implementation of UASs with non-metric cameras. The produced guidelines, specifications, and recommendations that result from this research will enable this implementation to be accomplished, allowing NCDOT to produce consistent and reliable survey-grade geospatial products.

## Chapter 8 Reference


Agisoft, (2021), Agisoft Metashape User Manual: Professional Edition, Version 1.7

Agüera-Vega, F., Carvajal-Ramírez, F., & Martínez-Carricondo, P. (2017a). Assessment of photogrammetric mapping accuracy based on variation ground control points number using unmanned aerial vehicle. *Measurement: Journal of the International Measurement Confederation*, *98*, 221–227. https://doi.org/10.1016/j.measurement.2016.12.002

Agüera-Vega, F., Carvajal-Ramírez, F., & Martínez-Carricondo, P. (2017b). Accuracy of Digital Surface Models and Orthophotos Derived from Unmanned Aerial Vehicle Photogrammetry. *Journal of Surveying Engineering*, *143*(2), 04016025. https://doi.org/10.1061/(asce)su.1943-5428.0000206

Alfio, V. S., Costantino, D., & Pepe, M. (2020). Influence of image tiff format and jpeg compression level in the accuracy of the 3d model and quality of the orthophoto in uav photogrammetry. *Journal of Imaging*, *6*(5). https://doi.org/10.3390/jimaging6050030

Anders, N., Smith, M., Suomalainen, J., Cammeraat, E., Valente, J., & Keesstra, S. (2020). Impact of flight altitude and cover orientation on Digital Surface Model (DSM) accuracy for flood damage assessment in Murcia (Spain) using a fixed-wing UAV. *Earth Science Informatics*, *13*(2), 391–404. https://doi.org/10.1007/s12145-019-00427-7

Barba, S., Barbarella, M., di Benedetto, A., Fiani, M., Gujski, L., & Limongiello, M. (2019). Accuracy assessment of 3d photogrammetric models from an unmanned aerial vehicle. *Drones*, *3*(4), 1–19. https://doi.org/10.3390/drones3040079

Barry, P. and Coakley, S. (2013), Accuracy of UAV photogrammetry compared with network RTK GPS. *International Architecture Photogrammetry Remote Sensing*, Melbourne, Australia

Bausman, D, and Commert, G. (2019), "*Unmanned Aircraft Systems Impact on Operational Efficiency and Connectivity, Final Report.*" South Carolina Department of Transportation.

Beal, F. (2017). *Unmanned Aerial Vehicle (UAV) Mapping Demonstration*. Montana Department of Transportation. https://www.mdt.mt.gov/other/webdata/external/Research/DOCS/RESEARCH_PROJ/UAV/REF_MAT/MAP_DEMO.pdf

Benassi, F., Dall'Asta, E., Diotri, F., Forlani, G., Cella, U. M. di, Roncella, R., & Santise, M. (2017). Testing accuracy and repeatability of UAV blocks oriented with gnss-supported aerial triangulation. *Remote Sensing*, *9*(2). https://doi.org/10.3390/rs9020172

Benjamin, A. R., Dennis O'brien, ;, Barnes, G., Wilkinson, B. E., & Volkmann, W. (2020). *Improving Data Acquisition Efficiency: Systematic Accuracy Evaluation of GNSS-Assisted Aerial Triangulation in UAS Operations*. https://doi.org/10.1061/(ASCE)SU.1943

Bolkas, D. (2019). Assessment of GCP Number and Separation Distance for Small UAS Surveys with and without GNSS-PPK Positioning. *Journal of Surveying Engineering*, *145*(3), 04019007. https://doi.org/10.1061/(asce)su.1943-5428.0000283

Brooks, C. N., Dobson, R. J., Dean, D. B., Banach, D., Oommen, T., Havens, T. C., Ahlborn, T. M., Cook, S. J., & Clover, A. (2014). Evaluating the use of unmanned aerial vehicles for transportation purposes: A michigan demonstration. *21st World Congress on Intelligent Transport Systems, ITSWC 2014: Reinventing Transportation in Our Connected World*.

Brooks, C., Dobson, R., Banach, D., Onmmen, T., Zhang, K., Mukherjee, T., Havens, T., Ahlborn, T., Ahlborn, R., Escobar-Wolf, R. Bhat, C., Zhao, S., Lyu, Q, and Marion, N. (2018). "*Implementation of Unmanned Aerial Vehicles (UAVs) for Assessment of Transportation Infrastructure - Phase II*." Michigan Department of Transportation.

Burdziakowski, P., & Bobkowska, K. (2021). Uav photogrammetry under poor lighting conditions—accuracy considerations. *Sensors*, *21*(10). https://doi.org/10.3390/s21103531

Catania, P., Comparetti, A., Febo, P., Morello, G., Orlando, S., Roma, E., & Vallone, M. (2020). Positioning accuracy comparison of GNSS receivers used for mapping and guidance of agricultural machines. *Agronomy*, *10*(7). https://doi.org/10.3390/agronomy10070924

Domingo, D., Ørka, H. O., Næsset, E., Kachamba, D., & Gobakken, T. (2019). Effects of UAV Image Resolution, Camera Type, and Image Overlap on Accuracy of Biomass Predictions in a Tropical Woodland. *Remote Sensing 2019, Vol. 11, Page 948*, *11*(8), 948. https://doi.org/10.3390/RS11080948

Dorafshan, S., Maguire, M., Hoffer, N., & Coopmans, C. (2017). *Fatigue Crack Detection Using Unmanned Aerial Systems in Under-Bridge Inspection*. IDAHO TRANSPORTATION DEPARTMENT. https://digitalcommons.usu.edu/cee_facpub/3588

Eyerman, J., Mooring, B., & Catlow, M. (2018). *North Carolina Study of Drone Use in Collision Reconstruction Continues*. North Carolina Department of Transportation (NCDOT). https://www.rti.org/sites/default/files/resources/rti-publication-file-f7d8d062-a878-4106-8f04-8977f984d559.pdf

Federal Geographic Data Committee, (1998). "Geospatial Positioning Accuracy Standards Part 3: National Standard for Spatial Data Accuracy." *Federal Geographic Data Committee*

Ferrer-González, E., Agüera-Vega, F., Carvajal-Ramírez, F., & Martínez-Carricondo, P. (2020). UAV photogrammetry accuracy assessment for corridor mapping based on the number and distribution of ground control points. *Remote Sensing*, *12*(15). https://doi.org/10.3390/RS12152447

Förstner, W., & Wrobel, B. P. (2016). *Bundle Adjustment*. 643–725. https://doi.org/10.1007/978-3-319-11550-4_15

Fraser, B. T., & Congalton, R. G. (2018). Issues in Unmanned Aerial Systems (UAS) data collection of complex forest environments. *Remote Sensing*, *10*(6). https://doi.org/10.3390/rs10060908

Gerke, M., & Przybilla, H. J. (2016). Accuracy analysis of photogrammetric UAV image blocks: Influence of onboard RTK-GNSS and cross flight patterns. *Photogrammetrie, Fernerkundung, Geoinformation*, *2016*(1), 17–30. https://doi.org/10.1127/pfg/2016/0284

Gillins, D., Parrish, C., Gillins, M., & Simpson, C. (2018). *Eyes in the Sky: Bridge Inspections With Unmanned Aerial Vehicles*. Oregon Department of Transportation. https://doi.org/FHWA-OR-RD-18-11

Gindraux, S., Boesch, R., & Farinotti, D. (2017). Accuracy assessment of digital surface models from Unmanned Aerial Vehicles' imagery on glaciers. *Remote Sensing*, *9*(2). https://doi.org/10.3390/rs9020186

Gray, J, Mitasova, H, Austin, R, and Blank, G. (2020), "*Final Report: UAS Roadmap*", North Carolina Department of Transportation.

Harwin, S., Lucieer, A., & Osborn, J. (2015). The impact of the calibration method on the accuracy of point clouds derived using unmanned aerial vehicle multi-view stereopsis. *Remote Sensing*, *7*(9), 11933–11953. https://doi.org/10.3390/rs70911933

Hubbard, S, and Hubbard, B. (2020), "*Investigation of Strategic Deployment Opportunities for Unmanned Aerial Systems (UAS) at INDOT*", Indiana Department of Transportation.

Hurwitz, D., Olsen, M., & Barlow, Z. (2018). *Driving Distraction Due to Drones*. Oregon Department of Transportation. https://doi.org/FHWA-OR-RD-18-12

Irizarry, J, and Johnson, E. (2019), "*Field-Test-Based Guideline Development for the Integration of Unmanned Aerial Systems (UASs) in GDOT Operations*", Georgia Department of Transportation.

James, M. R., Robson, S., d'Oleire-Oltmanns, S., & Niethammer, U. (2017). Optimising UAV topographic surveys processed with structure-from-motion: Ground control quality, quantity and

bundle adjustment. *Geomorphology*, *280*, 51–66. https://doi.org/10.1016/j.geomorph.2016.11.021

Jurjević, L., Gašparović, M., Milas, A. S., & Balenović, I. (2020). Impact of UAS image orientation on accuracy of forest inventory attributes. *Remote Sensing*, *12*(3). https://doi.org/10.3390/rs12030404

Kalacska, M., Lucanus, O., Arroyo-Mora, J. P., Laliberté, É., Elmer, K., Leblanc, G., & Groves, A. (2020). Accuracy of 3d landscape reconstruction without ground control points using different uas platforms. *Drones*, *4*(2), 1–26. https://doi.org/10.3390/drones4020013

Kamga, C., Sapphire, J., Cui, Y., Moghimidarzi, B., & Khryashchev, D. (2017). *Exploring Applications for Unmanned Aerial Systems and Unmanned Ground Systems in Enhanced Incident Management, Bridge Inspection, and Other Transportation-related Operations*. University Transportation Research Center. https://doi.org/C-15-01

Lee, S., Park, J., Choi, E., & Kim, D. (2021). Factors influencing the accuracy of shallow snow depth measured using uav-based photogrammetry. *Remote Sensing*, *13*(4), 1–20. https://doi.org/10.3390/rs13040828

Lercel, D., Steckel, R., and Pestka, J. (2018). *"Unmanned Aircraft Systems: An Overview of Strategies and Opportunities for Missouri."* Missouri Department of Transportation

Losè, L. T., Chiabrando, F., & Tonolo, F. G. (2020). Boosting the timeliness of UAV large scale mapping. Direct georeferencing approaches: Operational strategies and best practices. *ISPRS International Journal of Geo-Information*, *9*(10). https://doi.org/10.3390/ijgi9100578

Lovelace, B., and Zink, J. (2015). "*Unmanned Aerial Vehicle Bridge Inspection Demonstration Project.*" Minnesota Department of Transportation

Mallela, J, Wheeler, P, Sankaran, B, Choi, C, Gensib, E, Tetreault, R, and Hardy, D. (2021), "*Integration of UAS into Operations Conducted by New England Departments of Transportation – Develop Implementation Procedures for UAS applications (Task 4 Report)*", New England Transportation Consortium

Martinez, J. G., Albeaino, G., Gheisari, M., Volkmann, W., & Alarcón, L. F. (2020). UAS Point Cloud Accuracy Assessment Using Structure from Motion–Based Photogrammetry and PPK Georeferencing Technique for Building Surveying Applications. *Journal of Computing in Civil Engineering*, *35*(1), 05020004. https://doi.org/10.1061/(ASCE)CP.1943-5487.0000936

Martínez-Carricondo, P., Agüera-Vega, F., Carvajal-Ramírez, F., Mesas-Carrascosa, F. J., García-Ferrer, A., & Pérez-Porras, F. J. (2018). Assessment of UAV-photogrammetric mapping accuracy based on variation of ground control points. *International Journal of Applied Earth Observation and Geoinformation*, *72*, 1–10. https://doi.org/10.1016/j.jag.2018.05.015

Mcguire, M., Rys, M., & Rys, A. (2016). *A Study of How Unmanned Aircraft Systems Can Support the Kansas Department of Transportation's Efforts to Improve Efficiency, Safety, and Cost Reduction*. https://doi.org/K-TRAN: KSU-15-3

O'Neil-Dunne, J., & Estabrook, E. (2019). *"The Integration of Unmanned Aircraft Systems to Increase Safety and Decrease Costs of Transportation Projects and Related Tasks."* New Hampshire Department of Transportation (NHDOT).

Oniga, E., Breaban, A., & Statescu, F. (2018). *Determining the optimum number of ground control points for obtaining high precision results based on UAS images.* 5165. https://doi.org/10.3390/ecrs-2-05165

Otero, L. D. (2015). *Proof of Concept for using Unmanned Aerial Vehicles for High Mast Pole and Bridge Inspections*. Florida Department of Transportation, Research Center. https://doi.org/BDV28 TWO 977-02

Padró, J. C., Muñoz, F. J., Planas, J., & Pons, X. (2019). Comparison of four UAV georeferencing methods for environmental monitoring purposes focusing on the combined use with airborne and satellite remote sensing platforms. *International Journal of Applied Earth Observation and Geoinformation*, *75*, 130–140. https://doi.org/10.1016/j.jag.2018.10.018

Photogrammetric Engineering & Remote Sensing, (2015). "ASPRS Positional Accuracy Standards for Digital Geospatial Data." *Photogrammetric Engineering & Remote Sensing*, doi: 10.14358/PERS.81.3.A1-A26

Pix4D, (2019), *What is accuracy in an aerial mapping project?*

Plotnikov, M, Ni, D, and Price, D. (2019), "*The Application of Unmanned Aerial Systems In Surface Transportation - Volume II-A: Development of a Pilot Program to Integrate UAS Technology to Bridge and Rail Inspections*", Massachusetts Department of Transportation.

Ridolfi, E., Buffi, G., Venturi, S., & Manciola, P. (2017). Accuracy analysis of a dam model from drone surveys. *Sensors (Switzerland)*, *17*(8). https://doi.org/10.3390/s17081777

Ruzgiene, B., Berteška, T., Gečyte, S., Jakubauskiene, E., & Aksamitauskas, V. Č. (2015). The surface modelling based on UAV Photogrammetry and qualitative estimation. *Measurement: Journal of the International Measurement Confederation*, *73*, 619–627. https://doi.org/10.1016/j.measurement.2015.04.018

Sanz-Ablanedo, E., Chandler, J. H., Rodríguez-Pérez, J. R., & Ordóñez, C. (2018). Accuracy of Unmanned Aerial Vehicle (UAV) and SfM photogrammetry survey as a function of the number and location of ground control points used. *Remote Sensing*, *10*(10). https://doi.org/10.3390/rs10101606

Seifert, E., Seifert, S., Vogt, H., Drew, D., van Aardt, J., Kunneke, A., & Seifert, T. (2019). Influence of drone altitude, image overlap, and optical sensor resolution on multi-view reconstruction of forest images. *Remote Sensing*, *11*(10). https://doi.org/10.3390/rs11101252

Seitz, S. M., Curless, B., Diebel, J., Scharstein, D., & Szeliski, R. (2006). A comparison and evaluation of multi-view stereo reconstruction algorithms. *Proceedings of the IEEE Computer Society Conference on Computer Vision and Pattern Recognition*, *1*, 519–526. https://doi.org/10.1109/CVPR.2006.19

Snavely, N., Seitz, S. M., & Szeliski, R. (2007). Modeling the World from Internet Photo Collections. *International Journal of Computer Vision 2007 80:2*, *80*(2), 189–210. https://doi.org/10.1007/S11263-007-0107-3

Stevens, C., & Blackstock, T. (2017). *Demonstration of Unmanned Aircraft Systems Use for Traffic Incident Management (UAS-TIM) Final Report Demonstration of Unmanned Aircraft Systems Use for Traffic Incident Management ( UAS-TIM )*. Texas A&M Transportation Institute. https://doi.org/PRC 17-69 F

Stott, E., Williams, R. D., & Hoey, T. B. (2020). Ground control point distribution for accurate kilometre-scale topographic mapping using an rtk-gnss unmanned aerial vehicle and sfm photogrammetry. *Drones*, *4*(3), 1–21. https://doi.org/10.3390/drones4030055

Taddia, Y., Stecchi, F., & Pellegrinelli, A. (2020). Coastal mapping using dji phantom 4 RTK in post-processing kinematic mode. *Drones*, *4*(2), 1–19. https://doi.org/10.3390/drones4020009

Tomaštík, J., Mokroš, M., Saloš, S., Chudỳ, F., & Tunák, D. (2017). Accuracy of photogrammetric UAV-based point clouds under conditions of partially-open forest canopy. *Forests*, *8*(5). https://doi.org/10.3390/f8050151

Tomaštík, J., Mokroš, M., Surový, P., Grznárová, A., & Merganič, J. (2019). UAV RTK/PPK method-An optimal solution for mapping inaccessible forested areas? *Remote Sensing*, *11*(6). https://doi.org/10.3390/RS11060721

Toth, C., Jozkow, G., & Grejner-Brzezinska, D. (2015). Mapping with Small UAS: A Point Cloud Accuracy Assessment. *Journal of Applied Geodesy*, *9*(4), 213–226. https://doi.org/10.1515/jag-2015-0017

Wang, X., Chen, J. C., & Dadi, G. B. (n.d.). *Factors Influencing Measurement Accuracy of Unmanned Aerial Systems (UAS) and Photogrammetry in Construction Earthwork*.

Wells, J., and Lovelace, B. (2018). "*Improving the Quality of Bridge Inspections Using Unmanned Aircraft Systems (UAS)*." Minnesota Department of Transportation, <http://www.dot.state.mn.us/research/reports/2018/201826.pdf>.

Yang, Y., Lin, Z., & Liu, F. (2016). Stable imaging and accuracy issues of low-altitude unmanned aerial vehicle photogrammetry systems. *Remote Sensing*, *8*(4). https://doi.org/10.3390/rs8040316

Yu, J. J., Kim, D. W., Lee, E. J., & Son, S. W. (2020). Determining the optimal number of ground control points for varying study sites through accuracy evaluation of unmanned aerial system-based 3d point clouds and digital surface models. *Drones*, *4*(3), 1–19. https://doi.org/10.3390/drones4030049

Zhang, D., Watson, R., Dobie, G., MacLeod, C., Khan, A., & Pierce, G. (2020). Quantifying impacts on remote photogrammetric inspection using unmanned aerial vehicles. *Engineering Structures*, *209*. https://doi.org/10.1016/j.engstruct.2019.109940

Zhou, Y., Rupnik, E., Faure, P. H., & Pierrot-Deseilligny, M. (2018). GNSS-assisted integrated sensor orientation with sensor pre-calibration for accurate corridor mapping. *Sensors (Switzerland)*, *18*(9). https://doi.org/10.3390/s18092783

Zimmerman, T., Jansen, K., & Miller, J. (2020). Analysis of UAS flight altitude and ground control point parameters on DEM accuracy along a complex, developed coastline. *Remote Sensing*, *12*(14). https://doi.org/10.3390/rs12142305

# Chapter 9  Appendices

## Appendix I: Detailed Information of Data Evaluation of Each Data Collection on Each Site

This Appendix presents detailed information on data evaluation, including both UAS photogrammetry and LiDAR data evaluation.

### *Data Evaluation at Butner NCDOT/NCEM UAS Test Site*

This section describes the detailed information of UAS photogrammetry and LiDAR accuracy results at the Butner site.

### ***UAS Data Evaluation***

*Flight No. 1 Collected on February 3rd, 2020*

In this flight mission, a total of 243 images were collected using a single grid with 279 *ft* flight height, 17 *mm* focal length of the lens, and an 85% forward overlap, and a 70% side overlap. The GSD was 0.053 *ft*. 19 points were control points (C301, C304, C306, C316, C319, C320, P401, P402, P406, P407, P410, P413, P419, P421, P422, PID214, PID216, PID217, and PID223). 20 points were checkpoints (C307, C308, C309, P403, P404, P405, P408, P409, P411, P415, P416, P417, P418, PID204, PID205, PID207, PID208, PID222, PID224, and PID225). Figure 9.1 shows the distribution of the GCPs and checkpoints. The red points are control points, and the yellow points are checkpoints. Tables 9.1 through 9.3 show the detailed results of each flight mission using every software.


**Figure 9.1 GCPs and Checkpoints Layout**

**Table 9.1 Checkpoints Accuracy Results from Agisoft**

| Point | X error (*ft*) | Y error (*ft*) | Z error (*ft*) |
|---|---|---|---|
| C307 | -0.017 | 0.039 | -0.015 |
| C308 | 0.020 | -0.007 | -0.070 |
| C309 | -0.037 | 0.164 | 0.072 |
| P403 | 0.035 | -0.036 | 0.007 |
| P404 | 0.007 | 0.038 | -0.096 |
| P405 | -0.052 | -0.002 | -0.075 |
| P408 | 0.011 | 0.128 | -0.117 |
| P409 | 0.022 | -0.019 | 0.022 |
| P411 | 0.053 | -0.016 | 0.020 |
| P415 | 0.025 | 0.081 | -0.058 |
| P416 | 0.036 | 0.036 | -0.095 |
| P417 | -0.009 | -0.013 | -0.006 |
| P418 | 0.054 | -0.015 | 0.010 |
| PID204 | -0.008 | 0.108 | -0.068 |
| PID205 | 0.018 | 0.048 | -0.079 |
| PID207 | 0.056 | 0.018 | 0.012 |
| PID208 | 0.009 | 0.006 | -0.052 |
| PID222 | -0.005 | 0.043 | -0.129 |
| PID224 | -0.061 | 0.024 | 0.103 |
| PID225 | 0.017 | -0.019 | -0.023 |
| **Parameter** | **X error (*ft*)** | **Y error (*ft*)** | **Z error (*ft*)** |
| **No. Points =** | 20 | 20 | 20 |
| **Min (*ft*) =** | -0.061 | -0.036 | -0.129 |
| **Max (*ft*) =** | 0.056 | 0.164 | 0.103 |
| **Mean (*ft*) =** | 0.009 | 0.030 | -0.032 |
| **Std Dev (*ft*) =** | 0.033 | 0.054 | 0.062 |
| **RMSE (*ft*) =** | 0.033 | 0.061 | 0.069 |
| **NVA 95% (*ft*) =** | | | 0.135 |
| **RMSE R (*ft*) =** | 0.069 | | |
| **Case 1 95% CE (*ft*) =** | 0.120 | | |
| **Case 2 ~ CE (*ft*) =** | 0.115 | | |

**Table 9.2 Checkpoints Accuracy Results from Pix4D**

| Point | X error (*ft*) | Y error (*ft*) | Z error (*ft*) |
|---|---|---|---|
| C307 | 0.030 | 0.063 | 0.095 |
| C308 | -0.040 | -0.066 | -0.061 |
| C309 | -0.046 | -0.034 | -0.064 |
| P403 | -0.056 | -0.046 | 0.072 |
| P404 | 0.030 | 0.088 | -0.065 |

| | | | |
|---|---|---|---|
| P405 | -0.011 | -0.067 | 0.059 |
| P408 | -0.019 | -0.032 | 0.062 |
| P409 | -0.067 | -0.044 | -0.066 |
| P411 | -0.024 | 0.072 | -0.080 |
| P415 | -0.037 | 0.039 | -0.069 |
| P416 | -0.056 | -0.025 | 0.083 |
| P417 | 0.087 | -0.006 | 0.083 |
| P418 | -0.033 | 0.048 | -0.057 |
| PID204 | -0.043 | -0.037 | -0.078 |
| PID205 | 0.081 | 0.054 | 0.051 |
| PID207 | 0.068 | -0.052 | -0.081 |
| PID208 | 0.059 | 0.045 | 0.059 |
| PID222 | -0.072 | 0.096 | 0.074 |
| PID224 | 0.033 | -0.031 | -0.060 |
| PID225 | 0.015 | -0.048 | 0.093 |
| **Parameter** | **X error (*ft*)** | **Y error (*ft*)** | **Z error (*ft*)** |
| **No. Points =** | 20 | 20 | 20 |
| **Min (*ft*) =** | -0.072 | -0.067 | -0.081 |
| **Max (*ft*) =** | 0.087 | 0.096 | 0.095 |
| **Mean (*ft*) =** | -0.005 | 0.001 | 0.003 |
| **Std Dev (*ft*) =** | 0.051 | 0.055 | 0.073 |
| **RMSE (*ft*) =** | 0.050 | 0.054 | 0.071 |
| **NVA 95% (*ft*) =** | | | 0.140 |
| **RMSE R (*ft*) =** | 0.074 | | |
| **Case 1 95% CE (*ft*) =** | 0.127 | | |
| **Case 2 ~ CE (*ft*) =** | 0.127 | | |

**Table 9.3 Checkpoints Accuracy Results from UASMaster**

| Point | X error (*ft*) | Y error (*ft*) | Z error (*ft*) |
|---|---|---|---|
| C307 | 0.040 | 0.045 | 0.075 |
| C308 | -0.024 | -0.007 | -0.021 |
| C309 | 0.008 | 0.008 | -0.057 |
| P403 | 0.013 | 0.028 | 0.073 |
| P404 | 0.040 | 0.043 | 0.010 |
| P405 | -0.004 | -0.083 | 0.094 |
| P408 | 0.010 | -0.064 | 0.010 |
| P409 | -0.041 | -0.091 | 0.005 |
| P411 | -0.072 | -0.087 | -0.123 |
| P415 | -0.051 | -0.093 | -0.103 |
| P416 | -0.041 | 0.019 | -0.051 |
| P417 | -0.029 | -0.088 | 0.027 |

| | | | |
|---|---|---|---|
| P418 | 0.053 | -0.131 | -0.059 |
| PID204 | -0.032 | -0.011 | 0.012 |
| PID205 | -0.039 | -0.033 | 0.033 |
| PID207 | 0.029 | 0.038 | 0.066 |
| PID208 | 0.025 | -0.033 | -0.045 |
| PID222 | 0.081 | 0.003 | -0.107 |
| PID224 | 0.127 | -0.058 | -0.178 |
| PID225 | 0.059 | -0.051 | -0.087 |
| **Parameter** | **X error (*ft*)** | **Y error (*ft*)** | **Z error (*ft*)** |
| **No. Points =** | 20 | 20 | 20 |
| **Min (*ft*) =** | -0.072 | -0.131 | -0.178 |
| **Max (*ft*) =** | 0.127 | 0.045 | 0.094 |
| **Mean (*ft*) =** | 0.008 | -0.032 | -0.021 |
| **Std Dev (*ft*) =** | 0.050 | 0.053 | 0.075 |
| **RMSE (*ft*) =** | 0.050 | 0.061 | 0.076 |
| **NVA 95% (*ft*) =** | | | 0.149 |
| **RMSE R (*ft*) =** | 0.079 | | |
| **Case 1 95% CE (*ft*) =** | 0.136 | | |
| **Case 2 ~ CE (*ft*) =** | 0.136 | | |

*Flight No. 2 Collected on February 25$^{th}$, 2021*

Flight mission 2 was conducted using a double grid path with a 25 *mm* focal length of the lens with 380 *ft* flight height and 90% image overlap. A total number of 684 images were collected and utilized during the process by Agisoft, Pix4D, and UASMaster. The GSD was 0.052 *ft*. 13 GCPs (UAS-2, UAS-3, C307, C319, P401, P403, P405, P415, P418, P421, PID204, PID 211, and PID 216) and 20 checkpoints (C301, C308, C309, C316, C320, P402, P404, P406, P407, P408, P509, P410, P413, P416, P417, P419, P422, PID301, PID208, and PID222) were chosen to build the model. Figure 9.2 shows the layout of the GCPs and checkpoints. The red points are control points, and the yellow points are checkpoints. The following Tables 9.4 through 9.6 show detailed results of data processing by three Agisoft, Pix4D, and UASMaster.


**Figure 9.2 The Layout of GCPs and Checkpoints**

**Table 9.4 Checkpoints Accuracy from Agisoft**

| Point | X error (*ft*) | Y error (*ft*) | Z error (*ft*) |
|---|---|---|---|
| C301 | -0.063 | 0.055 | 0.000 |
| C308 | 0.040 | -0.053 | 0.051 |
| C309 | 0.078 | -0.022 | 0.078 |
| C316 | -0.033 | 0.040 | 0.047 |
| C320 | 0.029 | 0.063 | 0.075 |
| P402 | -0.064 | 0.009 | 0.040 |
| P404 | 0.086 | 0.078 | 0.048 |
| P406 | 0.003 | -0.081 | -0.062 |
| P407 | -0.056 | -0.017 | -0.084 |
| P408 | -0.055 | 0.052 | -0.094 |
| P409 | 0.042 | 0.084 | -0.077 |
| P410 | 0.081 | -0.068 | -0.086 |
| P413 | 0.074 | 0.079 | 0.064 |

| | | | |
|---|---|---|---|
| P416 | -0.044 | -0.040 | -0.043 |
| P417 | 0.070 | -0.051 | -0.053 |
| P419 | -0.022 | 0.081 | 0.029 |
| P422 | 0.076 | -0.038 | 0.067 |
| PID207 | -0.034 | -0.076 | -0.070 |
| PID208 | 0.047 | -0.073 | -0.086 |
| PID222 | -0.023 | 0.046 | 0.031 |
| **Parameter** | **X error (*ft*)** | **Y error (*ft*)** | **Z error (*ft*)** |
| **No. Points =** | 20 | 20 | 20 |
| **Min (*ft*) =** | -0.064 | -0.081 | -0.094 |
| **Max (*ft*) =** | 0.086 | 0.084 | 0.078 |
| **Mean (*ft*) =** | 0.012 | 0.003 | -0.006 |
| **Std Dev (*ft*) =** | 0.056 | 0.061 | 0.065 |
| **RMSE (*ft*) =** | 0.056 | 0.060 | 0.064 |
| **NVA 95% (*ft*) =** | | | 0.125 |
| **RMSE R (*ft*) =** | 0.082 | | |
| **Case 1 95% CE (*ft*) =** | 0.141 | | |
| **Case 2 ~ CE (*ft*) =** | 0.141 | | |

**Table 9.5 Checkpoints Accuracy from Pix4D**

| Point | X error (*ft*) | Y error (*ft*) | Z error (*ft*) |
|---|---|---|---|
| C301 | 0.052 | -0.056 | -0.096 |
| C308 | -0.051 | 0.053 | -0.045 |
| C309 | -0.066 | -0.022 | -0.090 |
| C316 | 0.046 | -0.042 | -0.041 |
| C320 | -0.062 | 0.084 | 0.074 |
| P402 | 0.059 | 0.008 | -0.034 |
| P404 | -0.081 | -0.090 | -0.097 |
| P406 | -0.017 | 0.082 | 0.006 |
| P407 | 0.059 | 0.037 | -0.098 |
| P408 | -0.015 | -0.054 | 0.017 |
| P409 | -0.042 | -0.078 | 0.014 |
| P410 | -0.093 | 0.020 | -0.076 |
| P413 | 0.017 | -0.049 | 0.033 |
| P416 | 0.054 | 0.075 | -0.096 |
| P417 | -0.084 | 0.029 | -0.067 |
| P419 | 0.003 | -0.092 | -0.094 |
| P422 | 0.005 | 0.038 | 0.029 |
| PID207 | 0.039 | 0.070 | 0.047 |
| PID208 | -0.057 | -0.036 | -0.092 |
| PID222 | 0.015 | -0.083 | -0.093 |

| Parameter | X error (*ft*) | Y error (*ft*) | Z error (*ft*) |
|---|---|---|---|
| **No. Points =** | 20 | 20 | 20 |
| **Min (*ft*) =** | -0.093 | -0.092 | -0.098 |
| **Max (*ft*) =** | 0.059 | 0.084 | 0.074 |
| **Mean (*ft*) =** | -0.011 | -0.005 | -0.040 |
| **Std Dev (*ft*) =** | 0.053 | 0.062 | 0.058 |
| **RMSE (*ft*) =** | 0.053 | 0.060 | 0.070 |
| **NVA 95% (*ft*) =** | | | 0.136 |
| **RMSE R (*ft*) =** | 0.080 | | |
| **Case 1 95% CE (*ft*) =** | 0.138 | | |
| **Case 2 ~ CE (*ft*) =** | 0.138 | | |

**Table 9.6 Checkpoints Accuracy from UASMaster**

| Point | X error (*ft*) | Y error (*ft*) | Z error (*ft*) |
|---|---|---|---|
| C301 | -0.038 | -0.065 | 0.038 |
| C308 | 0.077 | -0.018 | 0.031 |
| C309 | -0.047 | 0.040 | -0.072 |
| C316 | -0.091 | -0.052 | 0.099 |
| C320 | 0.082 | -0.058 | 0.054 |
| P402 | -0.090 | -0.069 | 0.096 |
| P404 | -0.090 | 0.013 | -0.062 |
| P406 | -0.068 | 0.090 | -0.055 |
| P407 | -0.042 | -0.020 | 0.010 |
| P408 | -0.052 | -0.077 | -0.087 |
| P409 | -0.043 | -0.064 | -0.059 |
| P410 | -0.068 | 0.085 | -0.082 |
| P413 | -0.039 | 0.036 | -0.068 |
| P416 | -0.042 | 0.012 | 0.045 |
| P417 | -0.059 | 0.062 | -0.070 |
| P419 | 0.045 | -0.052 | -0.069 |
| P422 | -0.056 | -0.059 | 0.044 |
| PID207 | -0.045 | 0.033 | -0.011 |
| PID208 | -0.048 | 0.007 | -0.094 |
| PID222 | 0.059 | -0.083 | -0.095 |
| **Parameter** | **X error (*ft*)** | **Y error (*ft*)** | **Z error (*ft*)** |
| **No. Points =** | 20 | 20 | 20 |
| **Min (*ft*) =** | -0.091 | -0.083 | -0.095 |
| **Max (*ft*) =** | 0.082 | 0.090 | 0.099 |
| **Mean (*ft*) =** | -0.033 | -0.012 | -0.020 |
| **Std Dev (*ft*) =** | 0.054 | 0.056 | 0.066 |
| **RMSE (*ft*) =** | 0.062 | 0.056 | 0.067 |

| | | | |
|---|---|---|---|
| **NVA 95% (*ft*) =** | | | 0.132 |
| **RMSE R (*ft*) =** | 0.083 | | |
| **Case 1 95% CE (*ft*) =** | 0.144 | | |
| **Case 2 ~ CE (*ft*) =** | 0.144 | | |

*Flight No. 3 Collected on February 25th, 2021*

Flight mission 3 was conducted using a double grid path with a 17 *mm* focal length of the lens with 280 *ft* flight height and 80% image overlap. A total of 280 images were collected and utilized during the process by Agisoft, Pix4D, and UASMaster. 12 GCPs (UAS-2, UAS-3, C307, C319, P401, P403, P405, P415, P418, P421, PID 211, and PID 216) and 20 checkpoints (C301, C308, C309, C316, P402, P404, P406, P407, P408, P409, P410, P411, P413, P416, P417, P419, P422, PID209, PID222, and PID223) were chosen to build the model. Figure 9.3 shows the layout of the GCPs and checkpoints. The red points are control points, and the yellow points are checkpoints. The following Tables 9.7 through 9.9 show detailed results of data processing by three software.


**Figure 9.3 The Layout of GCPs and Checkpoints**

**Table 9.7 Checkpoints Accuracy from Agisoft**

| Point | X error (*ft*) | Y error (*ft*) | Z error (*ft*) |
|---|---|---|---|
| C301 | -0.039 | 0.036 | -0.029 |
| C308 | 0.074 | 0.070 | 0.079 |
| C309 | 0.056 | -0.059 | 0.087 |
| C316 | 0.075 | 0.024 | -0.068 |
| P402 | -0.034 | -0.003 | -0.012 |
| P404 | 0.064 | 0.080 | 0.079 |
| P406 | -0.044 | -0.066 | 0.015 |
| P407 | -0.052 | -0.050 | 0.045 |
| P408 | -0.049 | 0.010 | -0.070 |
| P409 | -0.067 | 0.023 | -0.090 |
| P410 | 0.073 | -0.078 | 0.037 |
| P411 | 0.028 | 0.039 | -0.069 |
| P413 | 0.070 | 0.093 | -0.004 |
| P416 | -0.078 | -0.099 | 0.058 |
| P417 | 0.051 | -0.069 | 0.045 |
| P419 | 0.024 | 0.092 | 0.061 |
| P422 | 0.066 | -0.078 | -0.087 |
| PID209 | -0.038 | 0.026 | -0.088 |
| PID222 | -0.049 | 0.052 | 0.096 |
| PID223 | -0.045 | 0.064 | 0.091 |
| **Parameter** | **X error (*ft*)** | **Y error (*ft*)** | **Z error (*ft*)** |
| **No. Points =** | 20 | 20 | 20 |
| **Min (*ft*) =** | -0.078 | -0.099 | -0.090 |
| **Max (*ft*) =** | 0.075 | 0.093 | 0.096 |
| **Mean (*ft*) =** | 0.004 | 0.005 | 0.009 |
| **Std Dev (*ft*) =** | 0.057 | 0.063 | 0.068 |
| **RMSE (*ft*) =** | 0.056 | 0.062 | 0.067 |
| **NVA 95% (*ft*) =** | | | 0.131 |
| **RMSE R (*ft*) =** | 0.084 | | |
| **Case 1 95% CE (*ft*) =** | 0.145 | | |
| **Case 2 ~ CE (*ft*) =** | 0.144 | | |

**Table 9.8 Checkpoints Accuracy from Pix4D**

| Point | X error (*ft*) | Y error (*ft*) | Z error (*ft*) |
|---|---|---|---|
| C301 | 0.008 | -0.046 | -0.096 |
| C308 | -0.068 | -0.005 | -0.058 |
| C309 | -0.058 | 0.011 | -0.074 |
| C316 | -0.071 | -0.043 | 0.030 |
| P402 | 0.039 | -0.023 | -0.015 |

| | | | |
|---|---|---|---|
| P404 | -0.088 | -0.063 | -0.082 |
| P406 | 0.015 | 0.081 | 0.007 |
| P407 | 0.055 | 0.065 | -0.080 |
| P408 | 0.056 | -0.033 | 0.002 |
| P409 | 0.007 | 0.007 | 0.078 |
| P410 | -0.094 | 0.093 | -0.085 |
| P411 | 0.047 | -0.001 | -0.073 |
| P413 | -0.051 | -0.076 | -0.042 |
| P416 | 0.045 | 0.042 | -0.075 |
| P417 | -0.091 | 0.062 | -0.046 |
| P419 | -0.034 | -0.097 | -0.068 |
| P422 | -0.081 | 0.056 | 0.091 |
| PID209 | 0.010 | -0.064 | 0.074 |
| PID222 | 0.045 | -0.083 | -0.094 |
| PID223 | 0.020 | -0.068 | -0.091 |
| **Parameter** | **X error (*ft*)** | **Y error (*ft*)** | **Z error (*ft*)** |
| **No. Points =** | 20 | 20 | 20 |
| **Min (*ft*) =** | -0.094 | -0.097 | -0.096 |
| **Max (*ft*) =** | 0.056 | 0.093 | 0.091 |
| **Mean (*ft*) =** | -0.015 | -0.009 | -0.035 |
| **Std Dev (*ft*) =** | 0.056 | 0.059 | 0.061 |
| **RMSE (*ft*) =** | 0.056 | 0.059 | 0.069 |
| **NVA 95% (*ft*) =** | | | 0.136 |
| **RMSE R (*ft*) =** | 0.081 | | |
| **Case 1 95% CE (*ft*) =** | 0.140 | | |
| **Case 2 ~ CE (*ft*) =** | 0.140 | | |

**Table 9.9 Checkpoints Accuracy from UASMaster**

| Point | X error (*ft*) | Y error (*ft*) | Z error (*ft*) |
|---|---|---|---|
| C301 | 0.049 | 0.042 | -0.072 |
| C308 | 0.061 | -0.085 | 0.065 |
| C309 | -0.078 | -0.032 | -0.091 |
| C316 | -0.007 | -0.097 | -0.045 |
| P402 | 0.053 | 0.037 | -0.050 |
| P404 | -0.069 | -0.082 | -0.077 |
| P406 | -0.052 | 0.070 | 0.034 |
| P407 | 0.049 | 0.040 | -0.065 |
| P408 | 0.048 | 0.012 | -0.081 |
| P409 | 0.081 | 0.087 | 0.072 |
| P410 | -0.070 | 0.080 | -0.088 |
| P411 | -0.042 | 0.088 | -0.065 |

| | | | |
|---|---|---|---|
| P413 | -0.042 | 0.044 | 0.077 |
| P416 | 0.060 | 0.053 | -0.050 |
| P417 | -0.070 | 0.056 | -0.059 |
| P419 | 0.026 | -0.061 | -0.097 |
| P422 | 0.052 | 0.005 | 0.006 |
| PID209 | -0.036 | 0.065 | -0.088 |
| PID222 | 0.056 | 0.036 | -0.079 |
| PID223 | 0.029 | 0.031 | -0.091 |
| **Parameter** | **X error (*ft*)** | **Y error (*ft*)** | **Z error (*ft*)** |
| **No. Points =** | 20 | 20 | 20 |
| **Min (*ft*) =** | -0.078 | -0.097 | -0.097 |
| **Max (*ft*) =** | 0.081 | 0.088 | 0.077 |
| **Mean (*ft*) =** | 0.005 | 0.019 | -0.042 |
| **Std Dev (*ft*) =** | 0.055 | 0.059 | 0.059 |
| **RMSE (*ft*) =** | 0.054 | 0.061 | 0.071 |
| **NVA 95% (*ft*) =** | | | 0.139 |
| **RMSE R (*ft*) =** | 0.081 | | |
| **Case 1 95% CE (*ft*) =** | 0.141 | | |
| **Case 2 ~ CE (*ft*) =** | 0.141 | | |

***LiDAR Data Evaluation***

*LiDAR Data Collected on March 17th, 2020*

Three LiDAR datasets were collected using the following different configurations:

- 295 *ft* flight height with 80° FOV with 40% overlap.
- 295 *ft* flight height with 56° FOV with 40% overlap.
- 229 *ft* flight height with 56° FOV with 40% overlap.

13 traditional surveyed points as GCPs and 20 checkpoints were used to merge the scans and evaluate the accuracy. The GCPs are C301, C305, C307, C308, C309, C311, C312, C313, C314, C315, C316, C319, and C320. The checkpoints are P401, P402, P403, P404, P405, P406, P407, P408, P409, P410, P415, P418, P422, PID201, PID204, PID207, PID222, PID223, PID224, and PID225. Table 9.10 shows the detailed results of each LiDAR mission.

**Table 9.10 Surveyed Checkpoint Accuracy Statistics for SDC's LiDAR Flight at Butner on March 17th, 2020**

| Flight No. | | Flight 1 | | Flight 2 | | Flight 3 | |
|---|---|---|---|---|---|---|---|
| | Surveyed (*ft*) | LiDAR(*ft*) | Difference | LiDAR(*ft*) | Difference | LiDAR(*ft*) | Difference |
| P401 | 358.78 | 358.720 | -0.060 | 358.750 | -0.030 | 358.650 | -0.130 |
| P402 | 359.42 | 359.320 | -0.100 | 359.260 | -0.160 | 359.340 | -0.080 |
| P403 | 362.98 | 362.920 | -0.060 | 362.910 | -0.070 | 362.990 | 0.010 |
| P404 | 363.29 | 363.270 | -0.020 | 363.340 | 0.050 | 363.200 | -0.090 |
| P405 | 361.13 | 361.140 | 0.010 | 361.080 | -0.050 | 361.090 | -0.040 |
| P406 | 359.54 | 359.580 | 0.040 | 359.580 | 0.040 | 359.550 | 0.010 |

| | | | | | | | |
|---|---|---|---|---|---|---|---|
| P407 | 361.84 | 361.760 | -0.080 | 361.850 | 0.010 | 361.880 | 0.040 |
| P408 | 362.24 | 362.260 | 0.020 | 362.200 | -0.040 | 362.200 | -0.040 |
| P409 | 362.67 | 362.620 | -0.050 | 362.660 | -0.010 | 362.660 | -0.010 |
| P410 | 361.88 | 361.890 | 0.010 | 361.830 | -0.050 | 361.850 | -0.030 |
| P415 | 359.16 | 359.260 | 0.100 | 359.270 | 0.110 | 359.280 | 0.120 |
| P418 | 363.18 | 363.150 | -0.030 | 363.140 | -0.040 | 363.200 | 0.020 |
| P422 | 357.95 | 357.950 | 0.000 | 357.930 | -0.020 | 357.940 | -0.010 |
| PID201 | 359.92 | 359.990 | 0.070 | 359.960 | 0.040 | 359.990 | 0.070 |
| PID204 | 358.73 | 358.750 | 0.020 | 358.770 | 0.040 | 358.760 | 0.030 |
| PID207 | 360.63 | 360.640 | 0.010 | 360.650 | 0.020 | 360.650 | 0.020 |
| PID222 | 361.85 | 361.910 | 0.060 | 361.880 | 0.030 | 361.850 | 0.000 |
| PID223 | 362.75 | 362.790 | 0.040 | 362.750 | 0.000 | 362.770 | 0.020 |
| PID224 | 362.8 | 362.800 | 0.000 | 362.830 | 0.030 | 362.810 | 0.010 |
| PID225 | 362.8 | 362.810 | 0.010 | 362.820 | 0.020 | 362.850 | 0.050 |
| **Min (*ft*) =** | | | -0.100 | | -0.160 | | -0.130 |
| **Max (*ft*) =** | | | 0.100 | | 0.110 | | 0.120 |
| **Mean (*ft*) =** | | | -0.001 | | -0.004 | | -0.002 |
| **Std Dev (*ft*) =** | | | 0.051 | | 0.057 | | 0.057 |
| **RMSE (*ft*) =** | | | 0.050 | | 0.056 | | 0.055 |
| **NVA 95% (*ft*) =** | | | 0.098 | | 0.109 | | 0.109 |

*LiDAR Data Collected on March 8th, 2021*

One LiDAR dataset was collected using 197 *ft* flight height with 80° FOV with 40% overlap. 15 traditional surveyed points were used as GCPs to merge the scans. The GCPs are C301, C304, C305, C306, C307, C308, C309, C311, C312, C313, C314, C315, C316, C319, and C320. 20 checkpoints (C301, C308, C309, C316, C320, P402, P404, P406, P407, P408, P409, P410, P413, P416, P417, P419, P422, PID207, PID208, and PID222) were used. Table 9.11 shows the detailed results of this LiDAR mission.

**Table 9.11 LiDAR Checkpoints Information at Butner Site on March 08th, 2021**

| Checkpoints | Known Z | LiDAR Z | Difference |
|---|---|---|---|
| C301 | 363.290 | 363.250 | -0.040 |
| C308 | 358.600 | 358.600 | 0.000 |
| C309 | 365.350 | 365.380 | 0.030 |
| C316 | 359.810 | 359.830 | 0.020 |
| C320 | 357.590 | 357.580 | -0.010 |
| P402 | 359.420 | 359.380 | -0.040 |
| P404 | 363.290 | 363.340 | 0.050 |
| P406 | 359.540 | 359.570 | 0.030 |
| P407 | 361.840 | 361.850 | 0.010 |
| P408 | 362.240 | 362.200 | -0.040 |
| P409 | 362.670 | 362.620 | -0.050 |
| P410 | 361.880 | 361.850 | -0.030 |
| P413 | 367.750 | 367.700 | -0.050 |
| P416 | 359.540 | 359.580 | 0.040 |
| P417 | 361.960 | 362.050 | 0.090 |
| P419 | 361.290 | 361.270 | -0.020 |
| P422 | 357.950 | 357.900 | -0.050 |

| | | | |
|---|---|---|---|
| PID207 | 360.630 | 360.630 | 0.000 |
| PID208 | 365.160 | 365.150 | -0.010 |
| PID222 | 361.850 | 361.830 | -0.020 |
| **Min (*ft*) =** | | | -0.050 |
| **Max (*ft*) =** | | | 0.090 |
| **Mean =** | | | -0.005 |
| **Std Dev. (*ft*) =** | | | 0.039 |
| **RMSE (*ft*) =** | | | 0.038 |
| **NVA 95% (*ft*)** | | | 0.074 |

Moreover, the LiDAR point cloud penetration was analyzed through trees for the Butner data using MATLAB, ArcGIS Pro, and CloudCompare (3D point cloud visualization software). Figure 9.4 shows the LiDAR point cloud in the Butner site. The size of this study site is around 1,386,951 *sq.ft*.

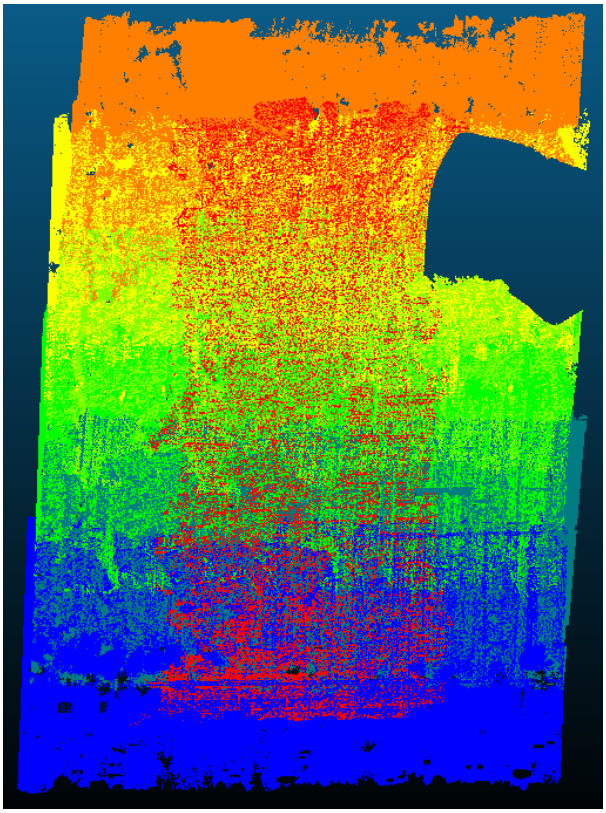

**Figure 9.4 LiDAR Point Cloud with only Vegetation**

The height of the point cloud varies between 328.26 *ft* and 458.29 *ft*. The NCSU team segmented the point cloud by 3 *ft* with 44 layers in MATLAB. However, the ground in the Butner site is with a slope. To better analyze the penetration of the LiDAR, the NCSU Research team selected four study areas in different locations in the tree area. Figure 9.5 shows the selected study areas in the tree area. Figures 9.6 (a), (b), (c), and (d) list the 3D point clouds in those four study areas. The red points mean the ground points; the green points are tree points. Figures 9.7 (a) and (b) show the top-down view of 3D ground points and 3D tree points in tree area 1. Figures 9.8 (a) and (b) show the top-down view of 3D ground points and 3D tree points in tree area 2. Figures 9.9 (a) and (b) show the top-down view of 3D ground points and 3D tree points in tree area 3. Figures 9.10 (a) and (b) show the top-down view of 3D ground points and 3D tree points in tree area 4.

Table 9.12 shows the basic information of those four study areas, including the ground elevations, point counts in both grounds and the tree, ground areas, and the ground point density in the areas.

According to the table, the average point density is 1.25 *point/sq.ft*, and the standard deviation is 0.15 *point/sq.ft*. Tree area 3 has a higher point density, while tree area 1 has a relatively lower point density. However, there is no obvious difference in ground point density in various locations.

Thus, overall, the performances of the LiDAR penetration in the Butner site in different locations are consistent. The points, for the most part, are evenly distributed.

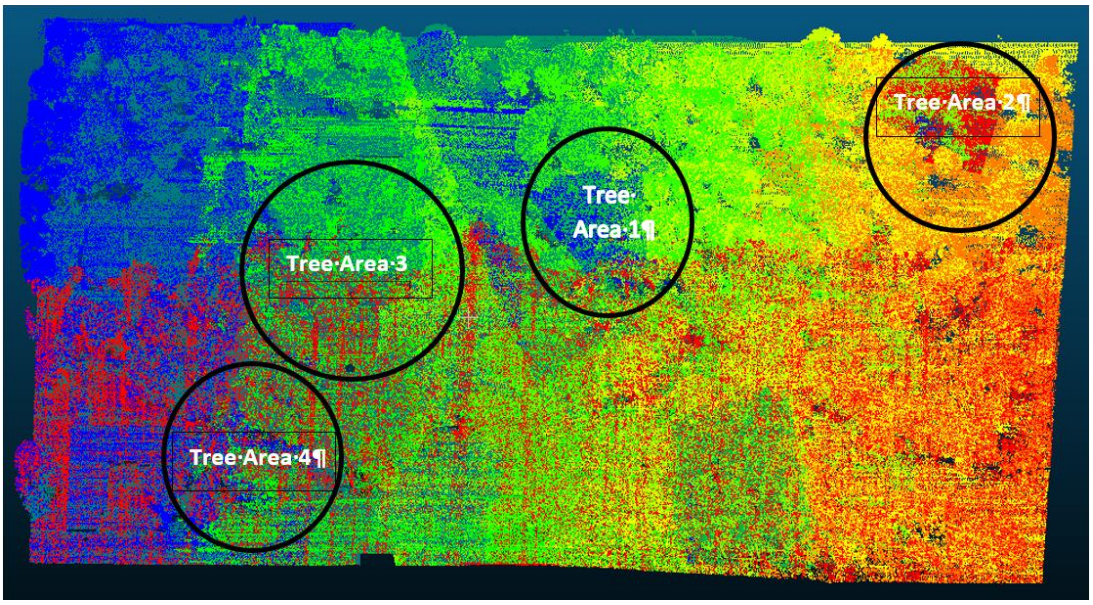


**Figure 9.5 Study Areas in the Trees Area**

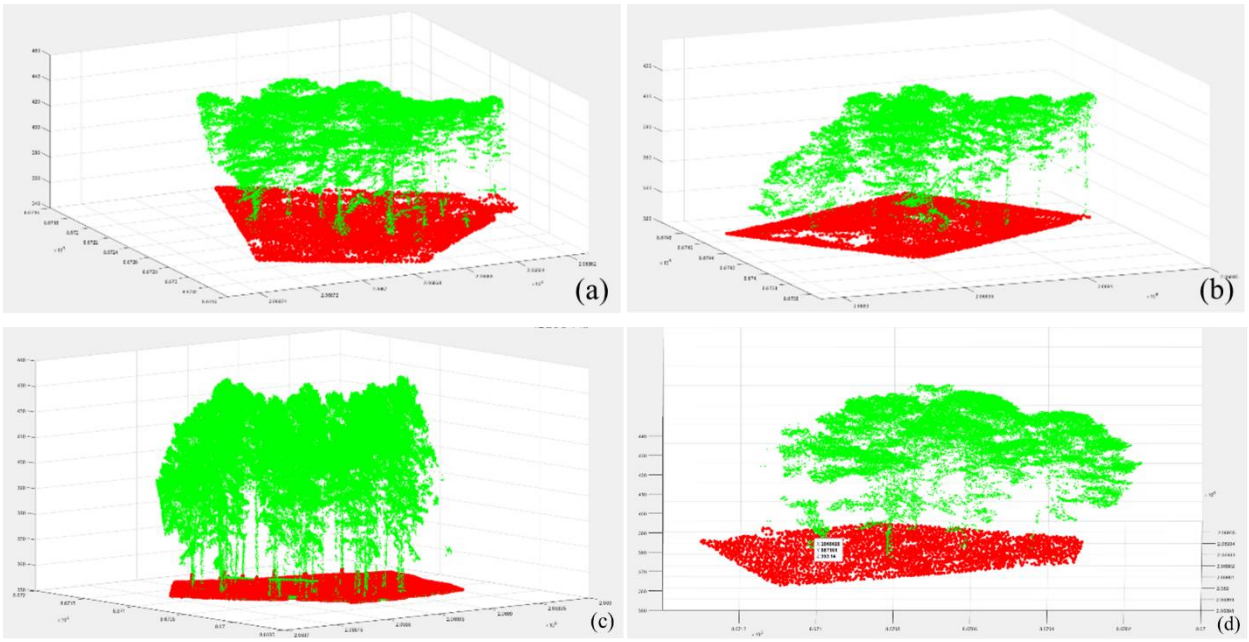


**Figure 9.6 Tree Area; (a) Tree Area 1; (b) Tree Area 2; (c) Tree Area 3; (d) Tree Area 4**

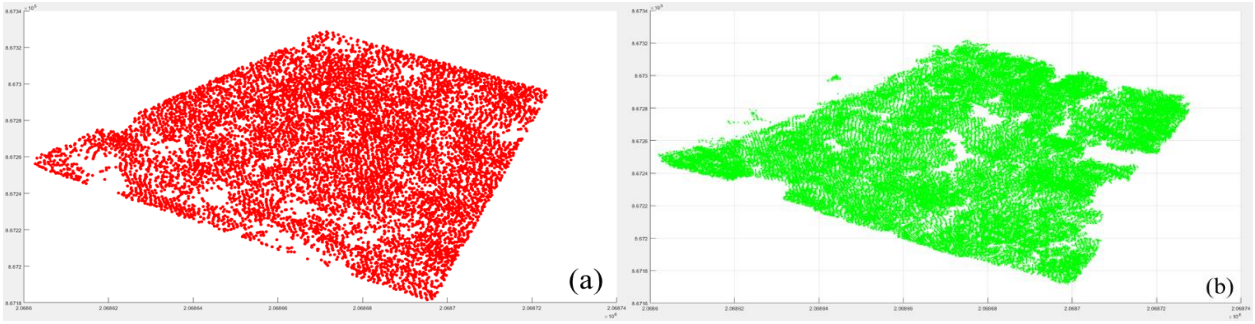


**Figure 9.7 Point Cloud in Tree Area 1; (a) Top Down View of Ground Point; (b) Top Down View of Tree Point**

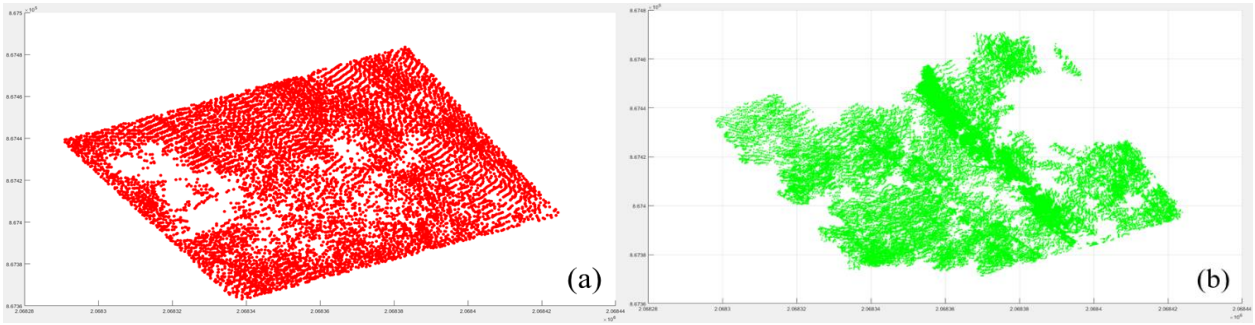


**Figure 9.8 Point Cloud in Tree Area 2; (a) Top Down View of Ground Point; (b) Top Down View of Tree Point**

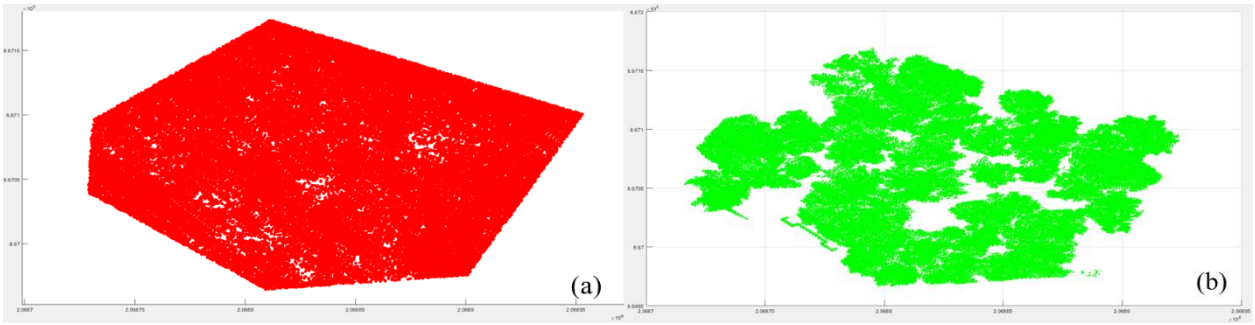


**Figure 9.9 Point Cloud in Tree Area 3; (a) Top Down View of Ground Point; (b) Top Down View of Tree Point**

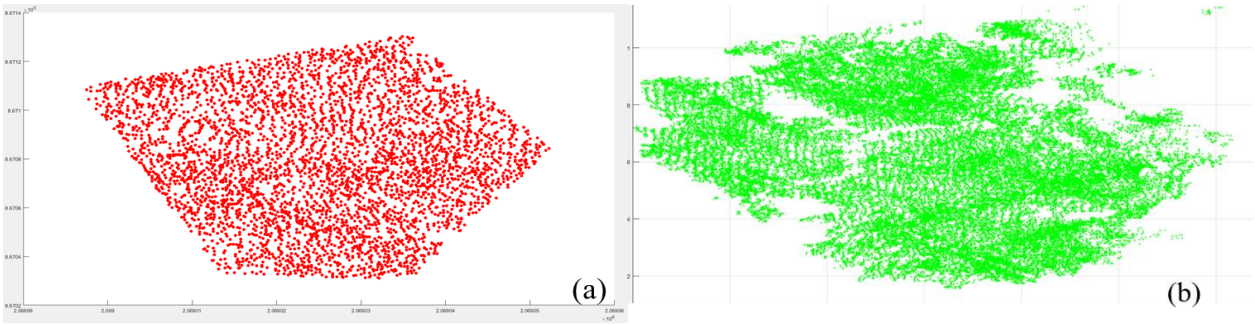


**Figure 9.10 Point Cloud in Tree Area 4; (a) Top Down View of Ground Point; (b) Top Down View of Tree Point**

**Table 9.12 Information of LiDAR Penetration in Different Locations**

| Study Areas | Elevation | Ground Point | Point on the Tree | Total Points | Area (*sq.ft*) | Ground Point Density in Area (*point/sq.ft*) |
|---|---|---|---|---|---|---|
| Tree Area 1 | 343 | 9,988 | 124,339 | 134,327 | 8,425 | 1.19 |
| Tree Area 2 | 332 | 9,732 | 77,601 | 87,333 | 8,585 | 1.13 |
| Tree Area 3 | 350 | 41,136 | 289,615 | 330,751 | 27,935 | 1.47 |
| Tree Area 4 | 352 | 4,307 | 62,135 | 66,442 | 3,550 | 1.21 |
| Total | | 65,163 | 553,690 | 618,853 | 48,495 | |
| **Average** | | 16,291 | 138,423 | 154,713 | 12,124 | **1.25** |
| **Standard Deviation** | | | | | | **0.15** |

***Data Evaluation at U2412-A Construction Site***

This section describes the detailed information of UAS photogrammetry and LiDAR accuracy results at the U2412-A construction site.

***<u>UAS Data Evaluation</u>***

This flight mission was performed on February 17th, 2020. Nadir images were captured with an 80% forward overlap and an 80% side overlap using a 25 *mm* lens. The flight height was 361 *ft*. An automatic single grid path flight was performed using the Pix4D capture application. A total of 203 images were collected. The average GSD was 0.053 *ft*. For the UAS data processing, 4 surveying GCPs (P3, P4, P20, and P22) were used during the data processing. Points p1, p2, p5, p6, p7, p8, p9, p10, p11, p12, p13, p14, p15, p16, p17, p18, p19, p21, p23, and p24 were checkpoints. A local coordinate system (NAD 1983 North Carolina State Plane US Feet 3200) was adopted. The GSD was 0.053 *ft* (1.63 *cm*). Figure 9.11 shows the layout of the GCPs and checkpoints. The red points are control points, and the yellow points are checkpoints. Tables 9.13 to 9.15 show the detailed results of each flight mission using every software.

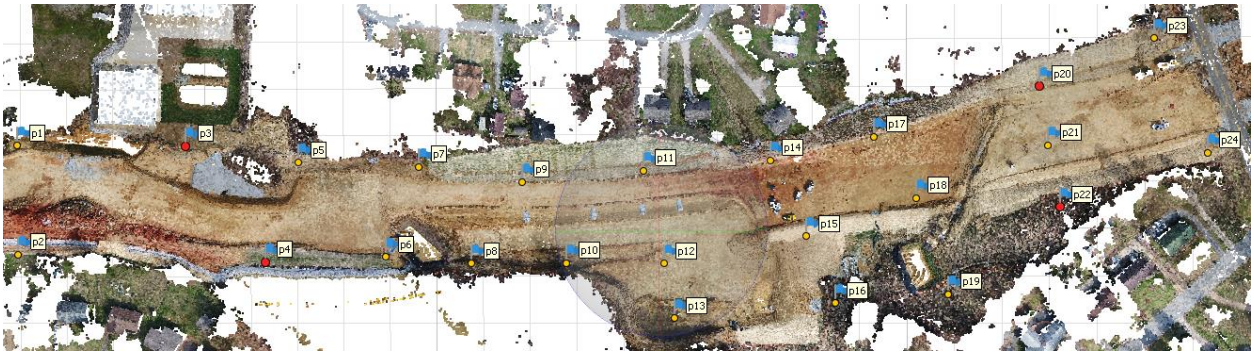


**Figure 9.11 The Layout of GCPs and Checkpoints**

**Table 9.13 Checkpoints Accuracy Table from Agisoft**

| Point | X error (*ft*) | Y error (*ft*) | Z error (*ft*) |
|---|---|---|---|
| P1 | -0.328 | 0.109 | -2.114 |
| P2 | -0.146 | 0.001 | -2.025 |
| p5 | -0.118 | 0.067 | 0.653 |
| p6 | 0.066 | -0.038 | 0.908 |
| p7 | -0.096 | 0.033 | 1.354 |
| p8 | 0.115 | -0.006 | 1.304 |
| p9 | 0.029 | 0.076 | 1.595 |
| p10 | 0.213 | 0.012 | 1.301 |
| p11 | 0.106 | 0.061 | 1.570 |
| p12 | 0.198 | 0.062 | 1.299 |
| p13 | 0.280 | 0.102 | 0.860 |
| p14 | 0.095 | -0.020 | 1.383 |
| p15 | 0.121 | 0.053 | 1.038 |
| p16 | 0.313 | 0.235 | 0.596 |
| p17 | 0.005 | -0.034 | 1.292 |
| p18 | 0.100 | 0.044 | 0.960 |
| p19 | 0.224 | 0.097 | -0.044 |
| p21 | 0.032 | 0.043 | 0.138 |
| p23 | -0.148 | 0.004 | -0.588 |
| p24 | 0.072 | 0.018 | -1.319 |
| **Parameter** | **X error (*ft*)** | **Y error (*ft*)** | **Z error (*ft*)** |
| **No. Points =** | 20 | 20 | 20 |
| **Min (*ft*) =** | -0.328 | -0.038 | -2.114 |
| **Max (*ft*) =** | 0.313 | 0.235 | 1.595 |
| **Mean (*ft*) =** | 0.057 | 0.046 | 0.508 |
| **Std Dev (*ft*) =** | 0.161 | 0.062 | 1.155 |
| **RMSE (*ft*) =** | 0.167 | 0.076 | 1.235 |
| **NVA 95% (*ft*) =** | | | 2.421 |
| **RMSE R (*ft*) =** | 0.183 | | |
| **Case 1 95% CE (*ft*) =** | 0.317 | | |
| **Case 2 ~ CE (*ft*) =** | 0.297 | | |

**Table 9.14 Checkpoints Accuracy Table from Pix4D**

| Point | X error (*ft*) | Y error (*ft*) | Z error (*ft*) |
|---|---|---|---|
| P1 | 0.108 | -0.020 | -2.030 |
| P2 | 0.155 | 0.068 | -1.985 |
| p5 | 0.137 | 0.053 | 0.469 |

| | | | |
|---|---|---|---|
| p6 | 0.310 | 0.036 | 0.895 |
| p7 | 0.120 | 0.073 | 1.150 |
| p8 | 0.209 | 0.062 | 1.286 |
| p9 | 0.152 | 0.060 | 1.418 |
| p10 | -0.068 | 0.050 | 1.279 |
| p11 | -0.152 | 0.057 | 1.534 |
| p12 | -0.230 | -0.001 | 1.148 |
| p13 | -0.183 | -0.041 | 0.845 |
| p14 | 0.098 | 0.003 | 1.279 |
| p15 | 0.167 | -0.056 | 0.881 |
| p16 | 0.170 | -0.184 | 0.432 |
| p17 | -0.200 | 0.070 | 1.007 |
| p18 | 0.069 | -0.030 | 0.943 |
| p19 | 0.046 | -0.107 | -0.005 |
| p21 | 0.080 | -0.004 | 0.041 |
| p23 | -0.068 | 0.036 | -0.591 |
| p24 | -0.130 | 0.010 | -1.103 |
| **Parameter** | **X error (*ft*)** | **Y error (*ft*)** | **Z error (*ft*)** |
| **No. Points =** | 20 | 20 | 20 |
| **Min (*ft*) =** | -0.230 | -0.184 | -2.030 |
| **Max (*ft*) =** | 0.310 | 0.073 | 1.534 |
| **Mean (*ft*) =** | 0.040 | 0.007 | 0.445 |
| **Std Dev (*ft*) =** | 0.155 | 0.067 | 1.081 |
| **RMSE (*ft*) =** | 0.156 | 0.065 | 1.144 |
| **NVA 95% (*ft*) =** | | | 2.242 |
| **RMSE R (*ft*) =** | 0.169 | | |
| **Case 1 95% CE (*ft*) =** | 0.145 | | |
| **Case 2 ~ CE (*ft*) =** | 0.144 | | |

**Table 9.15 Checkpoints Accuracy Results from UASMaster**

| Point | X error (*ft*) | Y error (*ft*) | Z error (*ft*) |
|---|---|---|---|
| P1 | 0.215 | -0.033 | 2.043 |
| P2 | 0.433 | 0.129 | 2.312 |
| p5 | 0.105 | 0.044 | -0.801 |
| p6 | 0.076 | 0.021 | -0.944 |
| p7 | 0.097 | 0.094 | -1.441 |
| p8 | 0.094 | 0.066 | -1.265 |
| p9 | 0.024 | 0.068 | -1.709 |
| p10 | -0.008 | 0.011 | -1.435 |

| | | | |
|---|---|---|---|
| p11 | -0.040 | 0.047 | -1.841 |
| p12 | 0.044 | -0.067 | -1.450 |
| p13 | 0.035 | -0.167 | -1.123 |
| p14 | -0.013 | 0.083 | -1.687 |
| p15 | 0.063 | -0.081 | -1.288 |
| p16 | 0.184 | -0.492 | -0.871 |
| p17 | -0.002 | 0.096 | -1.328 |
| p18 | 0.099 | -0.099 | -0.928 |
| p19 | 0.132 | -0.267 | -0.249 |
| p21 | 0.008 | 0.007 | -0.127 |
| p23 | -0.126 | 0.118 | 0.714 |
| p24 | -0.002 | 0.009 | 1.468 |
| **Parameter** | **X error (*ft*)** | **Y error (*ft*)** | **Z error (*ft*)** |
| **No. Points =** | 20 | 20 | 20 |
| **Min (*ft*) =** | -0.126 | -0.492 | -1.841 |
| **Max (*ft*) =** | 0.433 | 0.129 | 2.312 |
| **Mean (*ft*) =** | 0.071 | -0.021 | -0.597 |
| **Std Dev (*ft*) =** | 0.116 | 0.149 | 1.256 |
| **RMSE (*ft*) =** | 0.133 | 0.147 | 1.362 |
| **NVA 95% (*ft*) =** | | | 2.669 |
| **RMSE R (*ft*) =** | 0.199 | | |
| **Case 1 95% CE (*ft*) =** | 0.344 | | |
| **Case 2 ~CE (*ft*) =** | 0.343 | | |

***LiDAR Data Evaluation***

LiDAR data was collected on February 17th, 2020, using the following three different configurations:

- 295 *ft* flight height with 80° FOV and 50% overlap.
- 295 *ft* flight height with 80° FOV and 50% overlap.
- 295 *ft* flight height with 80° FOV and 50% overlap.

24 points were used to merge all the scans. Table 9.16 shows the detailed results of each LiDAR dataset using 20 checkpoints. 20 checkpoints are p3, p4, p5, p6, p7, p8, p9, p10, p11, p12, p13, p14, p15, p16, p17, p18, p28, p20, p21, and p22.

**Table 9.16 Surveyed Checkpoint Accuracy Statistics for SDC's LiDAR Flight at U2412-A Construction Site**

| Flight No. | | Flight 1 | | Flight 2 | | Flight 3 | |
|---|---|---|---|---|---|---|---|
| | Surveyed (*ft*) | LiDAR(*ft*) | Difference | LiDAR(*ft*) | Difference | LiDAR(*ft*) | Difference |
| p1 | 839.542 | 839.4 | -0.142 | 839.49 | -0.052 | 839.5 | -0.042 |
| p2 | 853.865 | 853.93 | 0.065 | 853.88 | 0.015 | 853.97 | 0.105 |
| p5 | 842.422 | 842.46 | 0.038 | 842.46 | 0.038 | 842.44 | 0.018 |
| p6 | 836.967 | 837.07 | 0.103 | 837.02 | 0.053 | 837.03 | 0.063 |
| p7 | 842.249 | 842.24 | -0.009 | 842.17 | -0.079 | 842.22 | -0.029 |
| p8 | 843.278 | 843.3 | 0.022 | 843.25 | -0.028 | 843.17 | -0.108 |
| p9 | 840.531 | 840.57 | 0.039 | 840.48 | -0.051 | 840.5 | -0.031 |
| p10 | 841.861 | 841.9 | 0.039 | 841.78 | -0.081 | 841.82 | -0.041 |
| p11 | 838.34 | 838.36 | 0.02 | 838.39 | 0.05 | 838.33 | -0.01 |
| p12 | 840.554 | 840.63 | 0.076 | 840.46 | -0.094 | 840.47 | -0.084 |
| p13 | 834.437 | 834.34 | -0.097 | 834.36 | -0.077 | 834.41 | -0.027 |
| p14 | 839.269 | 839.23 | -0.039 | 839.25 | -0.019 | 839.23 | -0.039 |
| p15 | 832.859 | 832.87 | 0.011 | 832.94 | 0.081 | 832.91 | 0.051 |
| p16 | 813.844 | 813.93 | 0.086 | 813.85 | 0.006 | 813.9 | 0.056 |
| p17 | 837.745 | 837.73 | -0.015 | 837.79 | 0.045 | 837.76 | 0.015 |
| p18 | 834.952 | 834.88 | -0.072 | 834.95 | -0.002 | 834.94 | -0.012 |
| p19 | 829.997 | 830.07 | 0.073 | 830.15 | 0.153 | 829.95 | -0.047 |
| p21 | 842.859 | 842.78 | -0.079 | 842.84 | -0.019 | 842.83 | -0.029 |
| p23 | 851.201 | 851.1 | -0.101 | 851.14 | -0.061 | 851.16 | -0.041 |
| p24 | 845.852 | 845.75 | -0.102 | 845.85 | -0.002 | 845.79 | -0.062 |
| **Min (*ft*) =** | | | -0.142 | | -0.094 | | -0.108 |
| **Max (*ft*) =** | | | 0.103 | | 0.153 | | 0.105 |
| **Mean (*ft*) =** | | | -0.004 | | -0.006 | | -0.015 |
| **Std Dev (*ft*) =** | | | 0.073 | | 0.063 | | 0.052 |
| **RMSE (*ft*) =** | | | 0.072 | | 0.062 | | 0.053 |
| **NVA 95% (*ft*) =** | | | 0.140 | | 0.122 | | 0.104 |

***Data Evaluation at R-2303 E Pit Site***

This section describes the detailed information of UAS photogrammetry and LiDAR accuracy results at the R-2303 E pit site.

***<u>UAS Data Evaluation</u>***

*Flight No.1 Collected on October 23rd, 2020*

One set of data was collected using a 25 *mm* focal lens and a single grid at 400 *ft* (the highest flight for the drone) with 90% by 90% image overlap. A total number of 1155 images were collected and utilized during the process by Agisoft, Pix4D, and UASMaster. The average GSD was 0.0663 *ft.* 13 points were used as GCPs (points 2, 15, E2, p1, p2, p6, p7, p8, p9, p11, p12, p13, and p14) to build the model. 20 points (1, 3, 4, 5, 6, 7, 8, 9, 10, 11, 12, 13, 14, E4, E10, E11, p3, p4, p5, and p10) were used as checkpoints to evaluate the results. Figure 9.12 shows the layout of the GCPs and checkpoints. The red points are control points, and the yellow points are checkpoints.

Tables 9.17 to 9.19 show detailed results of data processing by three Agisoft, Pix4D, and UASMaster.

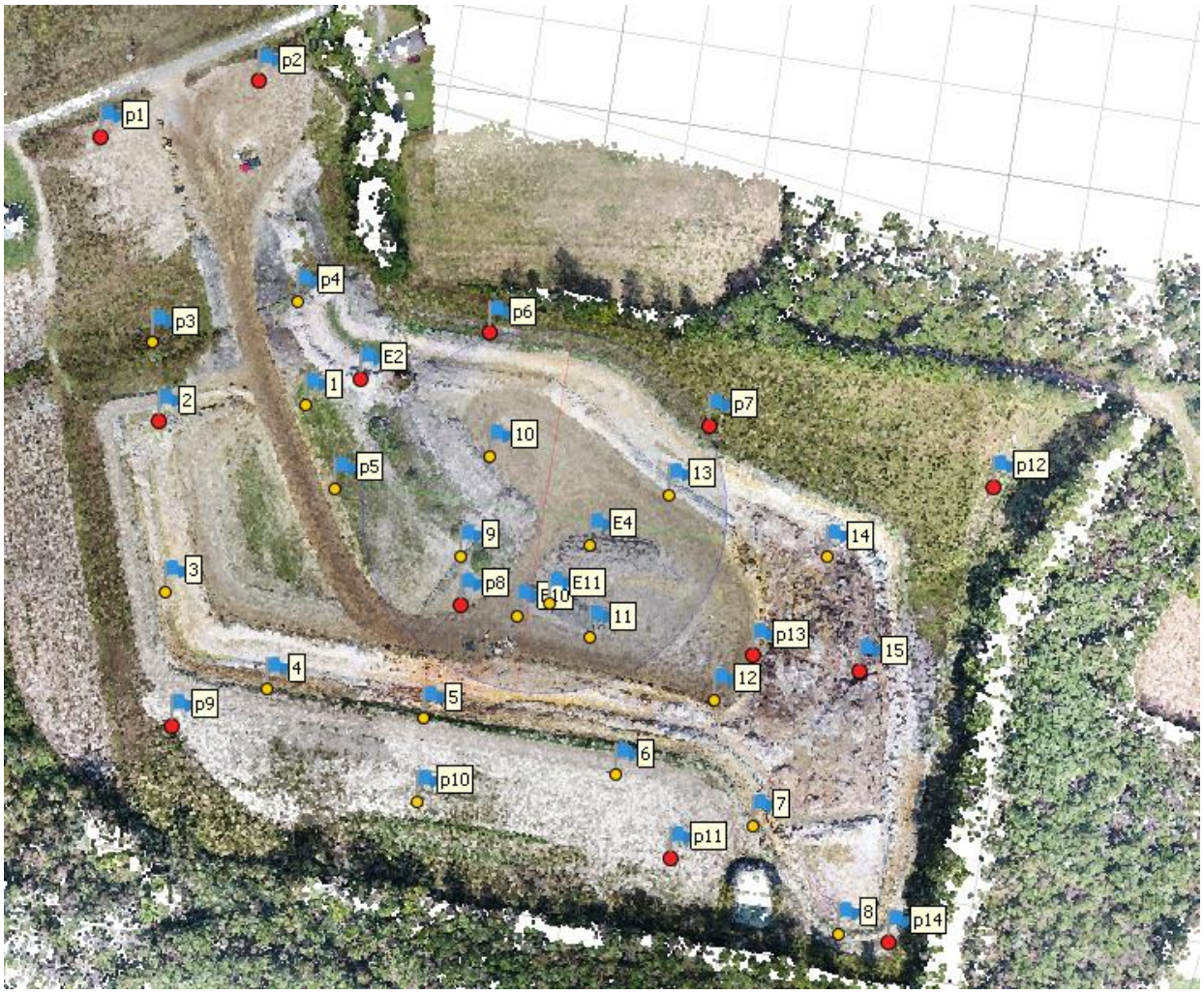


**Figure 9.12 The Layout of GCPs and Checkpoints**

**Table 9.17 Checkpoints Accuracy from Agisoft**

| Point | X error (*ft*) | Y error (*ft*) | Z error (*ft*) |
|---|---|---|---|
| 1 | 0.000 | 0.044 | -0.042 |
| 3 | 0.043 | 0.013 | -0.082 |
| 4 | 0.056 | -0.015 | 0.066 |
| 5 | 0.014 | -0.050 | 0.013 |
| 6 | -0.009 | 0.063 | 0.033 |
| 7 | -0.005 | 0.056 | 0.061 |
| 8 | -0.029 | 0.046 | 0.079 |
| 9 | 0.056 | -0.012 | -0.103 |
| 10 | 0.107 | -0.061 | 0.030 |

| | | | |
|---|---|---|---|
| 11 | 0.031 | 0.031 | -0.114 |
| 12 | -0.046 | 0.042 | -0.081 |
| 13 | 0.046 | -0.050 | 0.005 |
| 14 | -0.052 | -0.038 | -0.153 |
| E4 | 0.067 | -0.048 | 0.019 |
| E10 | 0.069 | 0.022 | -0.159 |
| E11 | 0.042 | -0.013 | 0.111 |
| p3 | 0.120 | 0.041 | 0.115 |
| p4 | 0.014 | 0.037 | 0.056 |
| p5 | 0.038 | -0.061 | -0.154 |
| p10 | 0.091 | 0.116 | 0.090 |
| **Parameter** | **X error (*ft*)** | **Y error (*ft*)** | **Z error (*ft*)** |
| **No. Points =** | 20 | 20 | 20 |
| **Min (*ft*) =** | -0.052 | -0.061 | -0.159 |
| **Max (*ft*) =** | 0.120 | 0.116 | 0.115 |
| **Mean (*ft*) =** | 0.033 | 0.008 | -0.011 |
| **Std Dev (*ft*) =** | 0.047 | 0.049 | 0.092 |
| **RMSE (*ft*) =** | 0.049 | 0.050 | 0.068 |
| **NVA 95% (*ft*) =** | | | 0.133 |
| **RMSE R (*ft*) =** | 0.070 | | |
| **Case 1 95% CE (*ft*) =** | 0.120 | | |
| **Case 2 ~ CE (*ft*) =** | 0.120 | | |

**Table 9.18 Checkpoints Accuracy from Pix4D**

| Point | X error (*ft*) | Y error (*ft*) | Z error (*ft*) |
|---|---|---|---|
| 1 | -0.048 | 0.072 | -0.041 |
| 3 | -0.047 | -0.046 | 0.056 |
| 4 | 0.074 | -0.039 | -0.032 |
| 5 | 0.030 | -0.061 | -0.083 |
| 6 | -0.029 | -0.016 | -0.031 |
| 7 | -0.086 | 0.052 | -0.066 |
| 8 | -0.051 | -0.060 | -0.065 |
| 9 | 0.051 | 0.090 | -0.035 |
| 10 | -0.060 | 0.027 | -0.148 |
| 11 | -0.056 | -0.080 | -0.079 |
| 12 | -0.044 | -0.065 | -0.077 |
| 13 | -0.055 | 0.050 | -0.043 |
| 14 | -0.020 | -0.012 | -0.055 |

| | | | |
|---|---|---|---|
| E4 | -0.032 | 0.070 | -0.063 |
| E10 | -0.012 | -0.067 | 0.070 |
| E11 | -0.003 | -0.020 | -0.039 |
| p3 | -0.041 | -0.038 | -0.069 |
| p4 | -0.052 | 0.075 | -0.033 |
| p5 | 0.084 | 0.085 | 0.098 |
| p10 | 0.073 | -0.008 | -0.088 |
| **Parameter** | **X error (*ft*)** | **Y error (*ft*)** | **Z error (*ft*)** |
| **No. Points =** | 20 | 20 | 20 |
| **Min (*ft*) =** | -0.086 | -0.080 | -0.148 |
| **Max (*ft*) =** | 0.084 | 0.090 | 0.098 |
| **Mean (*ft*) =** | -0.016 | 0.000 | -0.041 |
| **Std Dev (*ft*) =** | 0.051 | 0.059 | 0.057 |
| **RMSE (*ft*) =** | 0.052 | 0.057 | 0.069 |
| **NVA 95% (*ft*) =** | | | 0.136 |
| **RMSE R (*ft*) =** | 0.077 | | |
| **Case 1 95% CE (*ft*) =** | 0.134 | | |
| **Case 2 ~ CE (*ft*) =** | 0.134 | | |

**Table 9.19 Checkpoints Accuracy from UASMaster**

| Point | X error (*ft*) | Y error (*ft*) | Z error (*ft*) |
|---|---|---|---|
| 1 | 0.009 | 0.020 | -0.080 |
| 3 | 0.056 | -0.039 | -0.082 |
| 4 | 0.020 | -0.036 | 0.058 |
| 5 | 0.006 | 0.012 | 0.090 |
| 6 | -0.085 | 0.057 | 0.111 |
| 7 | -0.050 | 0.043 | 0.104 |
| 8 | -0.108 | 0.022 | 0.053 |
| 9 | 0.104 | 0.007 | -0.054 |
| 10 | 0.093 | -0.032 | 0.068 |
| 11 | 0.025 | 0.004 | -0.064 |
| 12 | -0.037 | 0.028 | -0.051 |
| 13 | 0.073 | -0.061 | 0.054 |
| 14 | 0.023 | -0.052 | -0.093 |
| E4 | 0.122 | -0.056 | 0.100 |
| E10 | 0.052 | 0.019 | -0.125 |
| E11 | 0.045 | 0.011 | 0.180 |
| p3 | 0.050 | -0.067 | -0.037 |

| | | | |
|---|---|---|---|
| p4 | -0.063 | 0.122 | -0.030 |
| p5 | -0.004 | -0.013 | -0.144 |
| p10 | -0.087 | 0.080 | 0.133 |
| **Parameter** | **X error (*ft*)** | **Y error (*ft*)** | **Z error (*ft*)** |
| **No. Points =** | 20 | 20 | 20 |
| **Min (*ft*) =** | -0.108 | -0.067 | -0.144 |
| **Max (*ft*) =** | 0.122 | 0.122 | 0.180 |
| **Mean (*ft*) =** | 0.012 | 0.003 | 0.010 |
| **Std Dev (*ft*) =** | 0.066 | 0.050 | 0.095 |
| **RMSE (*ft*) =** | 0.066 | 0.048 | 0.074 |
| **NVA 95% (*ft*) =** | | | 0.145 |
| **RMSE R (*ft*) =** | 0.082 | | |
| **Case 1 95% CE (*ft*) =** | 0.141 | | |
| **Case 2 ~ CE (*ft*) =** | 0.140 | | |

*Flight No.2 Collected on November 21st, 2020*

One set of data was collected using a 25 *mm* focal lens and a single grid at 400 *ft* (the highest flight for the drone) with 90% by 90% image overlap. The NCSU team evaluated the accuracy of the checkpoint at the R-2303 E pit site using three Agisoft, Pix4D, and UASMaster. A total number of 1112 images were collected and utilized during the process. 9 points (1, 9, p2, p6, p9, p12, p14, p21, and p31) were used as GCPs, and 20 checkpoints (2, 3, 4, 5, 6, 7, 8, 10, 11, 12, 13, 14, 15, p3, p5, p7, p8, p10, p24, and p33) were used as checkpoints to build the model. The average GSD was 0.0672 *ft* (2.05 *cm*). Figure 9.13 shows the layout of the GCPs and checkpoints. Tables 9.20 to 9.22 show detailed results of data processing by three software.

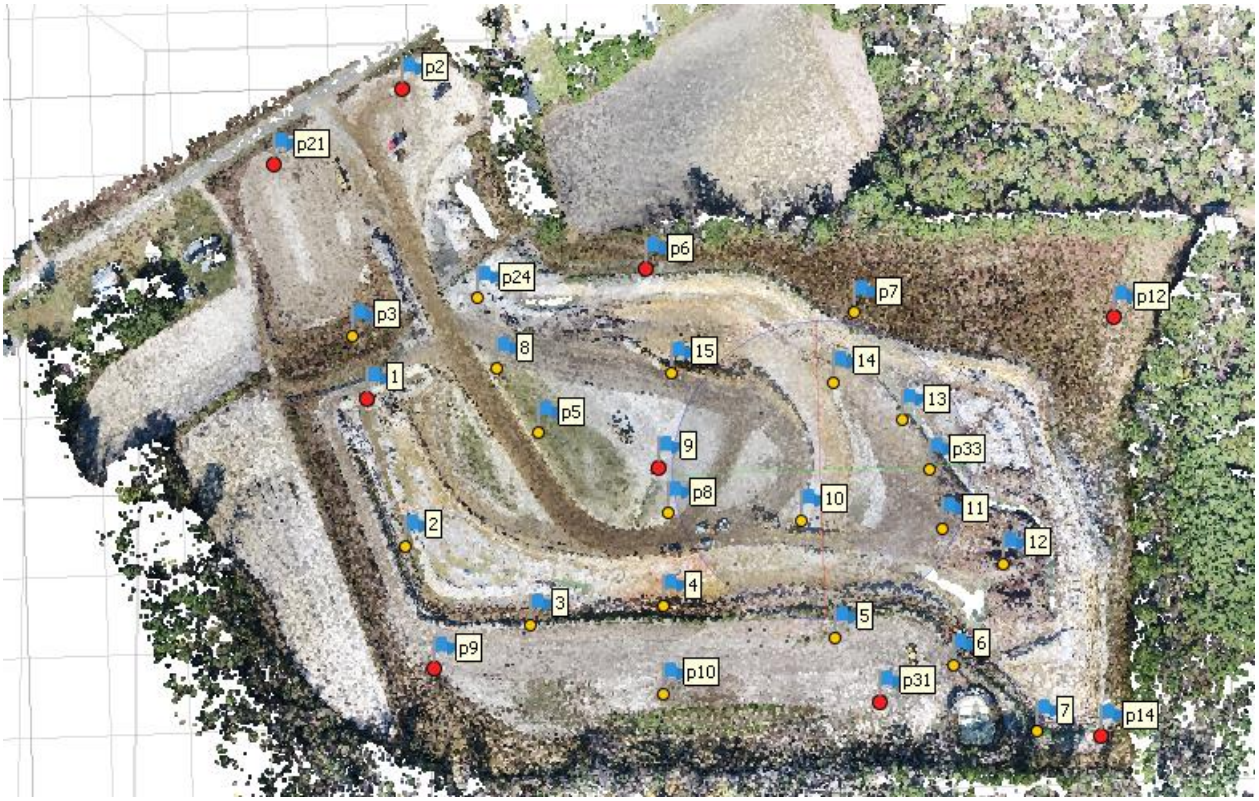


**Figure 9.13 The Layout of GCPs and Checkpoints**

**Table 9.20 Checkpoints Accuracy from Agisoft**

| Point | X error (*ft*) | Y error (*ft*) | Z error (*ft*) |
|---|---|---|---|
| 2 | 0.072 | 0.086 | 0.056 |
| 3 | 0.078 | -0.009 | 0.114 |
| 4 | 0.075 | -0.032 | -0.048 |
| 5 | 0.115 | -0.109 | 0.007 |
| 6 | 0.036 | -0.070 | 0.158 |
| 7 | -0.013 | -0.041 | 0.016 |
| 8 | -0.004 | 0.078 | 0.010 |
| 10 | 0.072 | -0.067 | -0.139 |
| 11 | -0.011 | -0.058 | -0.063 |
| 12 | -0.051 | -0.067 | 0.128 |
| 13 | -0.057 | -0.038 | -0.048 |
| 14 | -0.034 | -0.035 | -0.095 |
| 15 | -0.058 | -0.029 | 0.077 |
| p3 | -0.029 | 0.097 | 0.055 |
| p5 | 0.009 | 0.023 | -0.057 |
| p7 | -0.075 | -0.065 | -0.001 |
| p8 | 0.056 | -0.026 | -0.086 |

| | | | |
|---|---|---|---|
| p10 | 0.074 | -0.106 | -0.140 |
| p24 | 0.012 | 0.052 | -0.063 |
| p33 | -0.037 | -0.074 | -0.065 |
| **Parameter** | **X error (*ft*)** | **Y error (*ft*)** | **Z error (*ft*)** |
| **No. Points =** | 20 | 20 | 20 |
| **Min (*ft*) =** | -0.075 | -0.109 | -0.140 |
| **Max (*ft*) =** | 0.115 | 0.097 | 0.158 |
| **Mean (*ft*) =** | 0.011 | -0.025 | -0.009 |
| **Std Dev (*ft*) =** | 0.057 | 0.061 | 0.086 |
| **RMSE (*ft*) =** | 0.057 | 0.064 | 0.084 |
| **NVA 95% (*ft*) =** | | | 0.165 |
| **RMSE R (*ft*) =** | 0.086 | | |
| **Case 1 95% CE (*ft*) =** | 0.149 | | |
| **Case 2 ~ CE (*ft*) =** | 0.148 | | |

**Table 9.21 Checkpoints Accuracy from Pix4D**

| Point | X error (*ft*) | Y error (*ft*) | Z error (*ft*) |
|---|---|---|---|
| 2 | -0.063 | -0.050 | -0.030 |
| 3 | -0.002 | 0.059 | 0.087 |
| 4 | 0.003 | 0.071 | 0.075 |
| 5 | -0.062 | 0.091 | -0.010 |
| 6 | -0.013 | 0.085 | -0.128 |
| 7 | -0.043 | 0.084 | 0.100 |
| 8 | 0.000 | -0.071 | 0.109 |
| 10 | -0.097 | 0.056 | -0.062 |
| 11 | -0.077 | 0.057 | -0.127 |
| 12 | -0.051 | 0.064 | -0.117 |
| 13 | -0.099 | 0.091 | -0.097 |
| 14 | -0.076 | 0.070 | -0.049 |
| 15 | -0.008 | -0.034 | -0.092 |
| p3 | -0.098 | -0.081 | 0.052 |
| p5 | -0.006 | -0.012 | 0.075 |
| p7 | -0.087 | 0.080 | -0.072 |
| p8 | -0.051 | 0.045 | 0.097 |
| p10 | -0.002 | 0.058 | 0.079 |
| p24 | -0.050 | -0.045 | 0.071 |
| p33 | -0.080 | 0.115 | -0.125 |
| **Parameter** | **X error (*ft*)** | **Y error (*ft*)** | **Z error (*ft*)** |

| | | | |
|---|---|---|---|
| **No. Points =** | 20 | 20 | 20 |
| **Min (*ft*) =** | -0.099 | -0.081 | -0.128 |
| **Max (*ft*) =** | 0.003 | 0.115 | 0.109 |
| **Mean (*ft*) =** | -0.048 | 0.037 | -0.008 |
| **Std Dev (*ft*) =** | 0.037 | 0.061 | 0.090 |
| **RMSE (*ft*) =** | 0.060 | 0.070 | 0.088 |
| **NVA 95% (*ft*) =** | | | 0.173 |
| **RMSE R (*ft*) =** | 0.092 | | |
| **Case 1 95% CE (*ft*) =** | 0.159 | | |
| **Case 2 ~ CE (*ft*) =** | 0.159 | | |

**Table 9.22 Checkpoints Accuracy from UASMaster**

| **Point** | **X error (*ft*)** | **Y error (*ft*)** | **Z error (*ft*)** |
|---|---|---|---|
| 2 | -0.026 | -0.084 | -0.029 |
| 3 | -0.050 | -0.083 | -0.008 |
| 4 | -0.027 | -0.053 | 0.054 |
| 5 | -0.086 | 0.041 | 0.075 |
| 6 | -0.030 | 0.041 | 0.168 |
| 7 | 0.057 | -0.060 | -0.081 |
| 8 | -0.025 | -0.052 | -0.079 |
| 10 | -0.058 | 0.037 | -0.051 |
| 11 | -0.033 | 0.085 | 0.037 |
| 12 | -0.020 | 0.099 | 0.131 |
| 13 | -0.013 | 0.081 | -0.138 |
| 14 | -0.019 | 0.050 | -0.080 |
| 15 | -0.041 | 0.026 | -0.125 |
| p3 | 0.015 | -0.098 | 0.105 |
| p5 | -0.021 | -0.050 | -0.098 |
| p7 | -0.001 | 0.061 | -0.094 |
| p8 | -0.064 | -0.010 | -0.094 |
| p10 | -0.122 | -0.031 | 0.120 |
| p24 | -0.011 | -0.079 | 0.013 |
| p33 | -0.014 | 0.076 | -0.045 |
| **Parameter** | **X error (*ft*)** | **Y error (*ft*)** | **Z error (*ft*)** |
| **No. Points =** | 20 | 20 | 20 |
| **Min (*ft*) =** | -0.122 | -0.098 | -0.138 |
| **Max (*ft*) =** | 0.057 | 0.099 | 0.168 |
| **Mean (*ft*) =** | -0.029 | 0.000 | -0.011 |
| **Std Dev (*ft*) =** | 0.037 | 0.066 | 0.093 |

| | | | |
|---|---|---|---|
| **RMSE (*ft*) =** | 0.046 | 0.065 | 0.092 |
| **NVA 95% (*ft*) =** | | | 0.180 |
| **RMSE R (*ft*) =** | 0.079 | | |
| **Case 1 95% CE (*ft*) =** | 0.138 | | |
| **Case 2 ~ CE (*ft*) =** | 0.136 | | |

***LiDAR Data Evaluation***

LiDAR data collection was performed on November 21st, 2020, by SDC. One set of data was collected using a 229 *ft* flight height, 60% overlap, and 80° FOV. In this flight mission, 12 points were used as control points to merge all the scans, and 20 points (2, 3, 4, 5, 6, 7, 8, 10, 11, 12, 13, 14, 15, p3, p5, p7, p8, p10, p24, and p33) were used as checkpoints. Table 9.23 shows the detailed results.

**Table 9.23 LiDAR Checkpoints Accuracy at R-2303 E Pit Site**

| Control Points | Known Z | LiDAR Z | Difference |
|---|---|---|---|
| 2 | 141.469 | 141.620 | 0.151 |
| 3 | 154.279 | 154.240 | -0.039 |
| 4 | 147.137 | 147.139 | 0.002 |
| 5 | 152.02 | 152.149 | 0.129 |
| 6 | 154.302 | 154.440 | 0.138 |
| 7 | 153.308 | 153.330 | 0.022 |
| 8 | 147.823 | 147.880 | 0.057 |
| 10 | 140.919 | 141.089 | 0.170 |
| 11 | 138.284 | 138.340 | 0.056 |
| 12 | 147.29 | 147.300 | 0.010 |
| 13 | 139.152 | 139.270 | 0.118 |
| 14 | 138.795 | 138.980 | 0.185 |
| 15 | 147.956 | 148.040 | 0.084 |
| p3 | 146.253 | 146.32 | 0.067 |
| p5 | 149.069 | 149.14 | 0.071 |
| p7 | 148.997 | 149.180 | 0.183 |
| p8 | 149.236 | 149.21 | -0.026 |
| p10 | 151.605 | 151.750 | 0.145 |
| p24 | 145.113 | 145.11 | -0.003 |
| p33 | 138.94 | 139.02 | 0.080 |
| **Min (*ft*) =** | | | -0.185 |
| **Max (*ft*) =** | | | 0.039 |
| **Mean =** | | | 0.080 |
| **Std Dev. (*ft*) =** | | | 0.070 |
| **RMSE (*ft*) =** | | | 0.105 |
| **NVA 95% (*ft*) =** | | | 0.207 |

***Data Evaluation at I-26 Rock Slope Site***

This section describes the detailed information of UAS photogrammetry and LiDAR accuracy results at the I-26 rock slope site.

***<u>UAS Data Evaluation</u>***

*Flight No.1 Collected on September 30th, 2020*

This flight mission was conducted manually using a 17 *mm* lens. The highest flight height was 361 *ft*. Because the drone was manually controlled, the flight heights and image overlap varied. The range of the overlap was from 75% to 90% for both forward and side overlaps. 620 photos of the I-26 Rock Surface site were processed using Agisoft, Pix4D, and UASMaster. 11 points were used as GCPs (P2, P5, P9, P11, P12, P16, P20, P21, P22, P24, and P29) to build the model, and 20 checkpoints (P1, P3, P4, P6, P7, P8, P10, P13, P15, P17, P18, P19, P23, P25, P26, P27, P28, P30, and P31) were used to check the accuracy. Figure 9.14 shows the layout of the GCPs and checkpoints. The GCPs are shown in red, and checkpoints are shown in yellow.

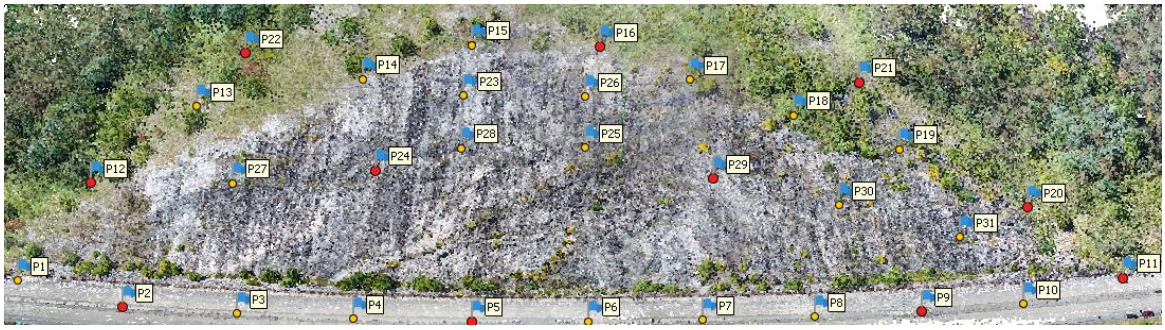


**Figure 9.14 The Layout of GCPs and Checkpoints at I-26 Rock Surface Site**

The average ground sample distance (GSD) was 0.069 *ft* (2.10 *cm*) with the range from 0.031 *ft* (0.94 *cm*) to 0.126 *ft* (3.85 *cm*). The smaller GSD indicates that the drone was closer to the surface (area 2 in this case), while the higher GSD means the drone was flying higher and away from the surface (area 1). Figure 9.15 shows the areas with different GSDs.

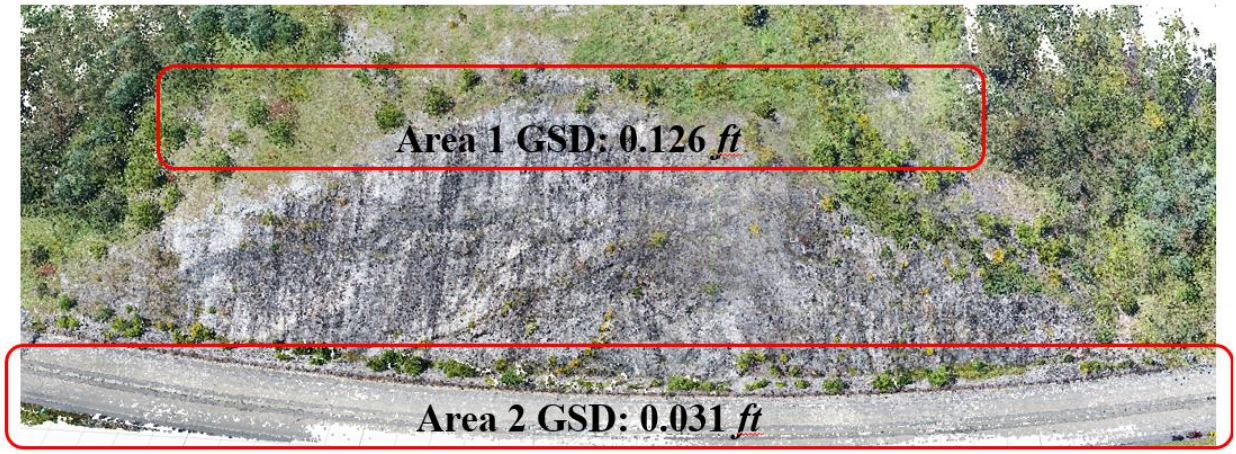


**Figure 9.15 GSD Areas**

Tables 9.24, 9,.25, and 9.26 show detailed overall results of data processing for 20 checkpoints by Agisoft, Pix4D, and UASMaster.

The results show that the checkpoints on the road panels (Aera 2 in Figure 9.16) have lower accuracy than the other points located above the road panels (Area 1 in Figure 9.16). The reason is that checkpoints located on the road panels have fewer reprojections (most reprojection is nine images) than other checkpoints. The accuracy of rest checkpoints was evaluated. Both horizontal and vertical accuracies were significantly improved. The results of checkpoints accuracy for road points and other points were listed in Tables 9.27 to 9.32.

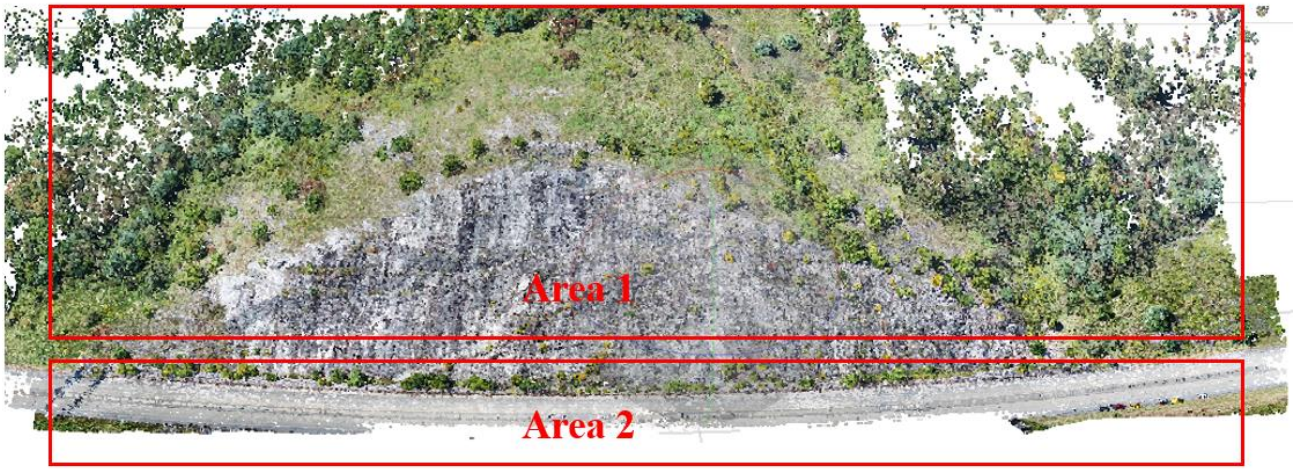


**Figure 9.16 The Location Areas of Points**

**Table 9.24 Checkpoints Accuracy in the Whole Area from Agisoft**

| Point | X error (*ft*) | Y error (*ft*) | Z error (*ft*) |
|---|---|---|---|
| P1 | 0.018 | 0.110 | -0.407 |
| P3 | -0.026 | 0.170 | -0.315 |
| P4 | 0.049 | -0.023 | -0.216 |
| P6 | 0.263 | -0.202 | 0.254 |
| P7 | 0.076 | -0.230 | 0.383 |
| P8 | -0.044 | -0.277 | -0.016 |
| P10 | 0.045 | -0.074 | -0.080 |
| P13 | 0.040 | -0.078 | 0.038 |
| P14 | -0.015 | -0.027 | 0.011 |
| P15 | -0.049 | -0.093 | -0.006 |
| P17 | -0.098 | -0.049 | -0.010 |
| P18 | -0.079 | 0.052 | 0.023 |
| P19 | -0.087 | -0.075 | 0.058 |
| P23 | -0.028 | -0.009 | 0.057 |
| P25 | 0.057 | 0.061 | 0.092 |

| | | | |
|---|---|---|---|
| P26 | 0.079 | 0.019 | 0.051 |
| P27 | 0.077 | -0.057 | 0.016 |
| P28 | 0.037 | -0.079 | 0.051 |
| P30 | 0.060 | 0.035 | 0.012 |
| P31 | 0.031 | 0.071 | 0.024 |
| **Parameter** | **X error (*ft*)** | **Y error (*ft*)** | **Z error (*ft*)** |
| **No. Points =** | 20 | 20 | 20 |
| **Min (*ft*) =** | -0.261 | -0.277 | -0.407 |
| **Max (*ft*) =** | 0.263 | 0.104 | 0.507 |
| **Mean (*ft*) =** | 0.020 | -0.038 | 0.001 |
| **Std Dev (*ft*) =** | 0.081 | 0.111 | 0.171 |
| **RMSE (*ft*) =** | 0.098 | 0.119 | 0.166 |
| **NVA 95% (*ft*) =** | | | 0.326 |
| **RMSE R (*ft*) =** | 0.154 | | |
| **Case 1 95% CE (*ft*) =** | 0.267 | | |
| **Case 2 ~ CE (*ft*) =** | 0.266 | | |

**Table 9.25 Checkpoints Accuracy in the Whole Area from Pix4D**

| Point | X error (*ft*) | Y error (*ft*) | Z error (*ft*) |
|---|---|---|---|
| P1 | -0.005 | -0.015 | -0.123 |
| P3 | -0.019 | 0.117 | -0.260 |
| P4 | 0.097 | 0.138 | -0.106 |
| P6 | 0.126 | -0.149 | 0.333 |
| P7 | -0.385 | 0.109 | -0.376 |
| P8 | 0.337 | -0.410 | 0.204 |
| P10 | 0.094 | -0.049 | -0.021 |
| P13 | 0.032 | -0.063 | 0.073 |
| P14 | -0.028 | -0.023 | -0.007 |
| P15 | -0.063 | -0.086 | -0.045 |
| P17 | -0.095 | -0.045 | -0.026 |
| P18 | -0.085 | 0.100 | 0.010 |
| P19 | -0.097 | -0.040 | 0.071 |
| P23 | -0.056 | -0.005 | 0.070 |
| P25 | 0.049 | 0.058 | 0.081 |
| P26 | 0.059 | 0.018 | 0.062 |
| P27 | 0.054 | -0.117 | 0.044 |
| P28 | 0.028 | -0.080 | 0.090 |
| P30 | 0.077 | 0.031 | 0.037 |

| | | | |
|---|---|---|---|
| P31 | 0.063 | 0.080 | 0.054 |
| **Parameter** | **X error (*ft*)** | **Y error (*ft*)** | **Z error (*ft*)** |
| **No. Points =** | 20 | 20 | 20 |
| **Min (*ft*) =** | -0.385 | -0.410 | -0.376 |
| **Max (*ft*) =** | 0.337 | 0.138 | 0.333 |
| **Mean (*ft*) =** | 0.009 | -0.021 | 0.008 |
| **Std Dev (*ft*) =** | 0.135 | 0.122 | 0.150 |
| **RMSE (*ft*) =** | 0.132 | 0.121 | 0.147 |
| **NVA 95% (*ft*) =** | | | 0.288 |
| **RMSE R (*ft*) =** | 0.179 | | |
| **Case 1 95% CE (*ft*) =** | 0.311 | | |
| **Case 2 ~ CE (*ft*) =** | 0.310 | | |

**Table 9.26 Checkpoints Accuracy in the Whole Area from UASMaster**

| Point | X error (*ft*) | Y error (*ft*) | Z error (*ft*) |
|---|---|---|---|
| P1 | 0.034 | 0.126 | -0.426 |
| P3 | -0.390 | 0.148 | -0.463 |
| P4 | -0.204 | -0.035 | -0.411 |
| P6 | 0.269 | -0.209 | 0.464 |
| P7 | 0.088 | -0.224 | 0.257 |
| P8 | -0.027 | -0.256 | -0.113 |
| P10 | 0.031 | -0.037 | -0.090 |
| P13 | 0.024 | -0.073 | 0.033 |
| P14 | -0.030 | -0.028 | 0.009 |
| P15 | -0.067 | -0.092 | -0.020 |
| P17 | -0.057 | -0.051 | -0.024 |
| P18 | -0.099 | 0.051 | 0.020 |
| P19 | -0.092 | -0.080 | 0.063 |
| P23 | -0.055 | -0.004 | 0.070 |
| P25 | 0.050 | 0.058 | 0.081 |
| P26 | 0.060 | 0.018 | 0.061 |
| P27 | 0.053 | -0.118 | 0.043 |
| P28 | 0.029 | -0.080 | 0.090 |
| P30 | 0.078 | 0.031 | 0.037 |
| P31 | 0.063 | 0.083 | 0.055 |
| **Parameter** | **X error (*ft*)** | **Y error (*ft*)** | **Z error (*ft*)** |
| **No. Points =** | 20 | 20 | 20 |

| | | | |
|---|---|---|---|
| **Min (*ft*) =** | -0.390 | -0.256 | -0.463 |
| **Max (*ft*) =** | 0.269 | 0.148 | 0.464 |
| **Mean (*ft*) =** | -0.012 | -0.039 | -0.013 |
| **Std Dev (*ft*) =** | 0.131 | 0.110 | 0.218 |
| **RMSE (*ft*) =** | 0.127 | 0.114 | 0.212 |
| **NVA 95% (*ft*) =** | | | 0.424 |
| **RMSE R (*ft*) =** | 0.170 | | |
| **Case 1 95% CE (*ft*) =** | 0.295 | | |
| **Case 2 ~ CE (*ft*) =** | 0.294 | | |

**Table 9.27 Checkpoints Accuracy Located on the Above Road from Agisoft (Area 1)**

| **Point** | **X error (*ft*)** | **Y error (*ft*)** | **Z error (*ft*)** |
|---|---|---|---|
| P13 | 0.04 | -0.078 | 0.038 |
| P14 | -0.015 | -0.027 | 0.011 |
| P15 | -0.049 | -0.093 | -0.006 |
| P17 | -0.098 | -0.049 | -0.01 |
| P18 | -0.079 | 0.052 | 0.023 |
| P19 | -0.087 | -0.075 | 0.058 |
| P23 | -0.028 | -0.009 | 0.057 |
| P25 | 0.057 | 0.061 | 0.092 |
| P26 | 0.079 | 0.019 | 0.0505 |
| P27 | 0.077 | -0.057 | 0.016 |
| P28 | 0.037 | -0.079 | 0.0505 |
| P30 | 0.06 | 0.035 | 0.012 |
| P31 | 0.031 | 0.071 | 0.024 |
| **Parameter** | **X error (*ft*)** | **Y error (*ft*)** | **Z error (*ft*)** |
| **No. Points =** | 13 | 13 | 13 |
| **Min (*ft*) =** | -0.098 | -0.093 | -0.01 |
| **Max (*ft*) =** | 0.079 | 0.071 | 0.058 |
| **Mean (*ft*) =** | 0.002 | -0.018 | 0.032 |
| **Std Dev (*ft*) =** | 0.064 | 0.059 | 0.029 |
| **RMSE (*ft*) =** | 0.062 | 0.060 | 0.042 |
| **NVA 95% (*ft*) =** | | | 0.083 |
| **RMSE R (*ft*) =** | 0.086 | | |
| **Case 1 95% CE (*ft*) =** | 0.149 | | |
| **Case 2 ~ CE (*ft*) =** | 0.149 | | |

**Table 9.28 Checkpoints Accuracy Located on the Road Panel from Agisoft (Area 2)**

| Point | X error (*ft*) | Y error (*ft*) | Z error (*ft*) |
|---|---|---|---|
| P1 | 0.018 | 0.110 | -0.407 |
| P3 | -0.026 | 0.170 | -0.315 |
| P4 | 0.049 | -0.023 | -0.216 |
| P6 | 0.263 | -0.202 | 0.254 |
| P7 | 0.076 | -0.230 | 0.383 |
| P8 | -0.044 | -0.277 | -0.016 |
| P10 | 0.045 | -0.074 | -0.080 |
| **Parameter** | **X error (*ft*)** | **Y error (*ft*)** | **Z error (*ft*)** |
| **No. Points =** | 7 | 7 | 7 |
| **Min (*ft*) =** | -0.044 | -0.277 | -0.407 |
| **Max (*ft*) =** | 0.263 | 0.170 | 0.383 |
| **Mean (*ft*) =** | 0.054 | -0.075 | -0.057 |
| **Std Dev (*ft*) =** | 0.101 | 0.172 | 0.291 |
| **RMSE (*ft*) =** | 0.108 | 0.176 | 0.275 |
| **NVA 95% (*ft*) =** | | | 0.539 |
| **RMSE R (*ft*) =** | 0.207 | | |
| **Case 1 95% CE (*ft*) =** | 0.358 | | |
| **Case 2 ~ CE (*ft*) =** | 0.348 | | |

**Table 9.29 Checkpoints Accuracy Located on the Above Road from Pix4D (Area 1)**

| Point | X error (*ft*) | Y error (*ft*) | Z error (*ft*) |
|---|---|---|---|
| P13 | 0.032 | -0.063 | 0.073 |
| P14 | -0.028 | -0.023 | -0.007 |
| P15 | -0.063 | -0.086 | -0.045 |
| P17 | -0.095 | -0.045 | -0.026 |
| P18 | -0.085 | 0.100 | 0.010 |
| P19 | -0.097 | -0.040 | 0.071 |
| P23 | -0.056 | -0.005 | 0.070 |
| P25 | 0.049 | 0.058 | 0.081 |
| P26 | 0.059 | 0.018 | 0.062 |
| P27 | 0.054 | -0.117 | 0.044 |
| P28 | 0.028 | -0.080 | 0.090 |
| P30 | 0.077 | 0.031 | 0.037 |
| P31 | 0.063 | 0.080 | 0.054 |
| **Parameter** | **X error (*ft*)** | **Y error (*ft*)** | **Z error (*ft*)** |
| **No. Points =** | 13 | 13 | 13 |

| | | | |
|---|---|---|---|
| **Min (*ft*) =** | -0.097 | -0.117 | -0.045 |
| **Max (*ft*) =** | 0.077 | 0.100 | 0.090 |
| **Mean (*ft*) =** | -0.005 | -0.013 | 0.040 |
| **Std Dev (*ft*) =** | 0.067 | 0.067 | 0.043 |
| **RMSE (*ft*) =** | 0.064 | 0.066 | 0.057 |
| **NVA 95% (*ft*) =** | | | 0.113 |
| **RMSE R (*ft*) =** | 0.092 | | |
| **Case 1 95% CE (*ft*) =** | 0.159 | | |
| **Case 2 ~ CE (*ft*) =** | 0.159 | | |

**Table 9.30 Checkpoints Accuracy Located on the Road Panel from Pix4D (Area 2)**

| **Point** | **X error (*ft*)** | **Y error (*ft*)** | **Z error (*ft*)** |
|---|---|---|---|
| P1 | -0.005 | -0.015 | -0.123 |
| P3 | -0.019 | 0.117 | -0.260 |
| P4 | 0.097 | 0.138 | -0.106 |
| P6 | 0.126 | -0.149 | 0.333 |
| P7 | -0.385 | 0.109 | -0.376 |
| P8 | 0.337 | -0.410 | 0.204 |
| P10 | 0.094 | -0.049 | -0.021 |
| **Parameter** | **X error (*ft*)** | **Y error (*ft*)** | **Z error (*ft*)** |
| **No. Points =** | 7 | 7 | 7 |
| **Min (*ft*) =** | -0.385 | -0.410 | -0.376 |
| **Max (*ft*) =** | 0.337 | 0.138 | 0.333 |
| **Mean (*ft*) =** | 0.035 | -0.037 | -0.050 |
| **Std Dev (*ft*) =** | 0.219 | 0.195 | 0.249 |
| **RMSE (*ft*) =** | 0.206 | 0.184 | 0.236 |
| **NVA 95% (*ft*) =** | | | 0.462 |
| **RMSE R (*ft*) =** | 0.276 | | |
| **Case 1 95% CE (*ft*) =** | 0.478 | | |
| **Case 2 ~ CE (*ft*) =** | 0.477 | | |

**Table 9.31 Checkpoints Accuracy Located on the Above Road from UASMaster (Area 1)**

| **Point** | **X error (*ft*)** | **Y error (*ft*)** | **Z error (*ft*)** |
|---|---|---|---|
| P13 | 0.024 | -0.073 | 0.033 |
| P14 | -0.030 | -0.028 | 0.009 |
| P15 | -0.067 | -0.092 | -0.020 |
| P17 | -0.057 | -0.051 | -0.024 |
| P18 | -0.099 | 0.051 | 0.020 |

| | | | |
|---|---|---|---|
| P19 | -0.092 | -0.080 | 0.063 |
| P23 | -0.055 | -0.004 | 0.070 |
| P25 | 0.050 | 0.058 | 0.081 |
| P26 | 0.060 | 0.018 | 0.061 |
| P27 | 0.053 | -0.118 | 0.043 |
| P28 | 0.029 | -0.080 | 0.090 |
| P30 | 0.078 | 0.031 | 0.037 |
| P31 | 0.063 | 0.083 | 0.055 |
| **Parameter** | **X error (*ft*)** | **Y error (*ft*)** | **Z error (*ft*)** |
| **No. Points =** | 13 | 13 | 13 |
| **Min (*ft*) =** | -0.099 | -0.118 | -0.024 |
| **Max (*ft*) =** | 0.078 | 0.083 | 0.090 |
| **Mean (*ft*) =** | -0.003 | -0.022 | 0.040 |
| **Std Dev (*ft*) =** | 0.065 | 0.066 | 0.036 |
| **RMSE (*ft*) =** | 0.062 | 0.067 | 0.053 |
| **NVA 95% (*ft*) =** | | | 0.103 |
| **RMSE R (*ft*) =** | 0.091 | | |
| **Case 1 95% CE (*ft*) =** | 0.158 | | |
| **Case 2 ~ CE (*ft*) =** | 0.158 | | |

**Table 9.32 Checkpoints Accuracy Located on the Road Panel from UASMaster (Area 2)**

| Point | X error (ft) | Y error (ft) | Z error (ft) |
|---|---|---|---|
| P1 | 0.034 | 0.126 | -0.426 |
| P3 | -0.390 | 0.148 | -0.463 |
| P4 | -0.204 | -0.035 | -0.411 |
| P6 | 0.269 | -0.209 | 0.464 |
| P7 | 0.088 | -0.224 | 0.257 |
| P8 | -0.027 | -0.256 | -0.113 |
| P10 | 0.031 | -0.037 | -0.090 |
| **Parameter** | **X error (*ft*)** | **Y error (*ft*)** | **Z error (*ft*)** |
| **No. Points =** | 7 | 7 | 7 |
| **Min (*ft*) =** | -0.390 | -0.277 | -0.407 |
| **Max (*ft*) =** | 0.263 | 0.170 | 0.383 |
| **Mean (*ft*) =** | -0.028 | -0.070 | -0.112 |
| **Std Dev (*ft*) =** | 0.212 | 0.166 | 0.360 |
| **RMSE (*ft*) =** | 0.199 | 0.169 | 0.352 |
| **NVA 95% (*ft*) =** | | | 0.690 |

| | | |
|---|---|---|
| **RMSE R (*ft*) =** | 0.261 | |
| **Case 1 95% CE (*ft*)=** | 0.451 | |
| **Case 2 ~ CE (*ft*) =** | 0.450 | |

*Flight No.2 Collected March 9th, 2021*

The flight mission was performed manually using a 17 *mm* lens to cover the whole area and to ensure adequate image overlap. The flight path was from top to bottom and from the right of the rock face to its left. The flight height was consistently at 393 *ft*. The range of the overlap was from 80% to 90% for both forward and side overlaps. 729 photos of the I-26 Rock Surface site were processed using three software. 11 points were used as GCPs (P2, P5, P9, P11, P12, P16, P20, P21, P22, P24, and P29) to build the model, and 20 checkpoints were used to check the accuracy. Figure 9.17 shows the layout of the GCPs and checkpoints. The GCPs are shown in red, and checkpoints are shown in yellow. All the target points can be divided into two groups based on their located areas. The first group is the target points located above the road panel (Area 1 in Figure 9.16). The other group is the target points located on the road panel (Area 2 in Figure 9.16).

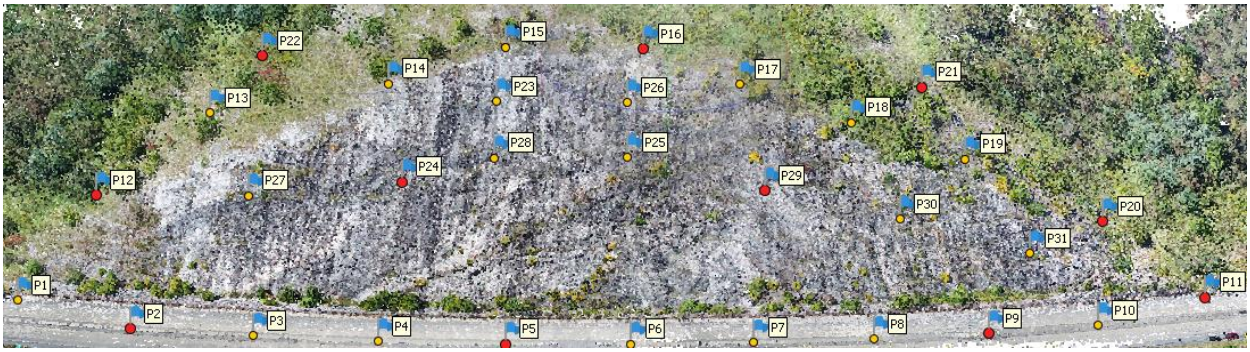


**Figure 9.17 The Layout of GCPs and Checkpoints at I-26 Rock Surface Site**

The average ground sample distance (GSD) was 0.067 *ft* (2.04 *cm)* with the range from 0.020 *ft* (0.62 *cm*) to 0.175 *ft* (5.34 *cm*). The smaller GSD indicates that the drone was closer to the low area of the rock surface (area 2 in this case), while the higher GSD means the drone was flying higher and away from the surface to catch the target points over the top of the rock surface and on the road panel (areas 1 and 3). Figure 9.18 shows the areas with different GSDs.

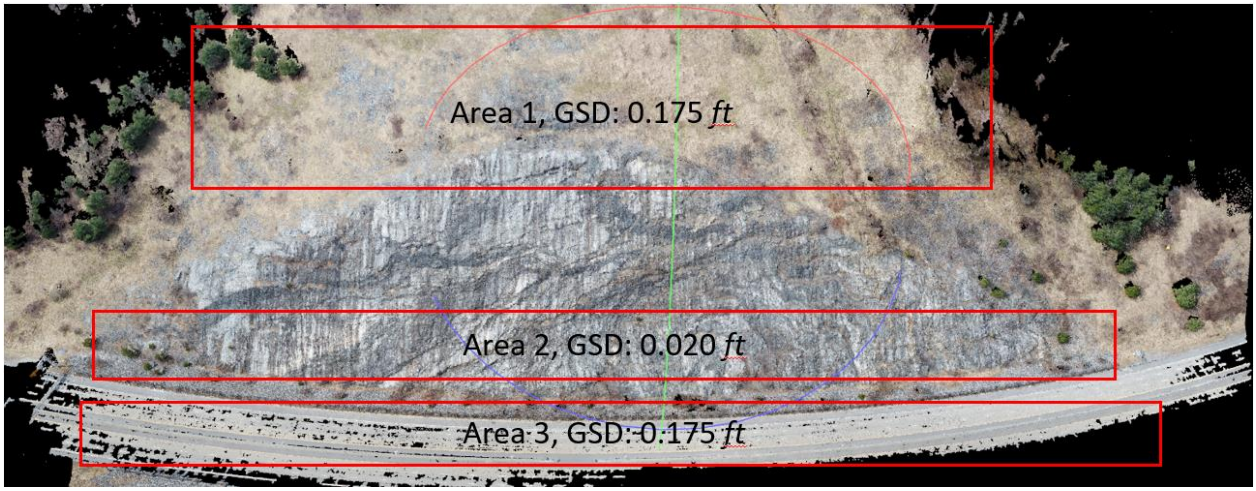


**Figure 9.18 GSD Areas**

Tables 9.33, 9.34, and 9.35 show detailed overall results of data processing for 20 checkpoints by Agisoft, Pix4D, and UASMaster. The results of checkpoints accuracy for road points (Area 2 in Figure 9.16) and other points (Area 1 in Figure 9.16) were listed in Tables 9.36, 9.37, 9.38, 9.39, 9.40, and 9.41.

**Table 9.33 Checkpoints Accuracy in the Whole Area from Agisoft**

| Point | X error (*ft*) | Y error (*ft*) | Z error (*ft*) |
|---|---|---|---|
| P1 | 0.001 | 0.008 | -0.061 |
| P3 | -0.042 | 0.060 | 0.016 |
| P4 | -0.054 | -0.044 | 0.004 |
| P6 | -0.097 | 0.079 | 0.012 |
| P7 | -0.059 | 0.075 | -0.022 |
| P8 | -0.073 | 0.034 | 0.065 |
| P10 | -0.022 | 0.015 | 0.049 |
| P13 | -0.030 | -0.073 | -0.016 |
| P14 | 0.052 | 0.053 | -0.092 |
| P15 | 0.051 | 0.003 | -0.061 |
| P17 | 0.042 | 0.006 | -0.083 |
| P18 | 0.080 | -0.049 | -0.079 |
| P19 | 0.074 | 0.075 | -0.068 |
| P23 | 0.064 | 0.004 | -0.040 |
| P25 | -0.010 | 0.058 | -0.078 |
| P26 | 0.012 | 0.071 | -0.067 |
| P27 | -0.051 | 0.030 | -0.043 |
| P28 | 0.059 | 0.059 | -0.074 |
| P30 | 0.034 | 0.074 | 0.001 |

| | | | |
|---|---|---|---|
| P31 | -0.014 | 0.009 | 0.072 |
| **Parameter** | **X error (*ft*)** | **Y error (*ft*)** | **Z error (*ft*)** |
| **No. Points =** | 20 | 20 | 20 |
| **Min (*ft*) =** | -0.097 | -0.073 | -0.092 |
| **Max (*ft*) =** | 0.080 | 0.079 | 0.072 |
| **Mean (*ft*) =** | 0.001 | 0.027 | -0.028 |
| **Std Dev (*ft*) =** | 0.054 | 0.045 | 0.051 |
| **RMSE (*ft*) =** | 0.052 | 0.056 | 0.058 |
| **NVA 95% (*ft*) =** | | | 0.113 |
| **RMSE R (*ft*) =** | 0.077 | | |
| **Case 1 95% CE (*ft*) =** | 0.133 | | |
| **Case 2 ~ CE (*ft*) =** | 0.133 | | |

**Table 9.34 Checkpoints Accuracy in the Whole Area from Pix4D**

| **Point** | **X error (*ft*)** | **Y error (*ft*)** | **Z error (*ft*)** |
|---|---|---|---|
| P1 | 0.021 | 0.081 | 0.017 |
| P3 | -0.050 | 0.080 | -0.106 |
| P4 | 0.061 | 0.074 | 0.076 |
| P6 | -0.021 | 0.032 | -0.081 |
| P7 | -0.046 | 0.024 | -0.030 |
| P8 | -0.050 | -0.034 | -0.068 |
| P10 | 0.029 | 0.055 | 0.030 |
| P13 | 0.066 | 0.009 | -0.018 |
| P14 | 0.086 | 0.066 | 0.036 |
| P15 | 0.010 | -0.081 | -0.014 |
| P17 | 0.006 | -0.093 | 0.060 |
| P18 | -0.080 | 0.061 | 0.100 |
| P19 | -0.098 | -0.050 | 0.100 |
| P23 | 0.049 | -0.069 | 0.078 |
| P25 | -0.034 | -0.062 | 0.050 |
| P26 | 0.031 | -0.024 | 0.069 |
| P27 | 0.012 | 0.058 | -0.043 |
| P28 | 0.033 | -0.009 | 0.010 |
| P30 | 0.046 | -0.012 | 0.037 |
| P31 | 0.034 | 0.043 | 0.014 |
| **Parameter** | **X error (*ft*)** | **Y error (*ft*)** | **Z error (*ft*)** |
| **No. Points =** | 20 | 20 | 20 |

| | | | |
|---|---|---|---|
| **Min (*ft*) =** | -0.098 | -0.093 | -0.068 |
| **Max (*ft*) =** | 0.086 | 0.081 | 0.100 |
| **Mean (*ft*) =** | 0.005 | 0.008 | 0.016 |
| **Std Dev (*ft*) =** | 0.051 | 0.058 | 0.059 |
| **RMSE (*ft*) =** | 0.050 | 0.057 | 0.060 |
| **NVA 95% (*ft*) =** | | | 0.118 |
| **RMSE R (*ft*) =** | 0.075 | | |
| **Case 1 95% CE (*ft*) =** | 0.131 | | |
| **Case 2 ~ CE (*ft*) =** | 0.130 | | |

**Table 9.35 Checkpoints Accuracy in the Whole Area from UASMaster**

| Point | X error (*ft*) | Y error (*ft*) | Z error (*ft*) |
|---|---|---|---|
| P1 | 0.050 | 0.056 | 0.094 |
| P3 | 0.080 | 0.031 | 0.062 |
| P4 | 0.031 | -0.065 | 0.083 |
| P6 | 0.090 | -0.040 | 0.028 |
| P7 | 0.040 | -0.049 | -0.013 |
| P8 | 0.058 | -0.036 | -0.097 |
| P10 | 0.066 | 0.054 | -0.086 |
| P13 | 0.045 | 0.080 | 0.059 |
| P14 | 0.059 | -0.062 | -0.058 |
| P15 | 0.046 | -0.082 | -0.069 |
| P17 | 0.040 | -0.051 | -0.050 |
| P18 | -0.056 | -0.040 | 0.046 |
| P19 | -0.052 | -0.075 | 0.064 |
| P23 | 0.066 | -0.095 | -0.035 |
| P25 | 0.051 | -0.037 | 0.020 |
| P26 | 0.063 | -0.063 | -0.059 |
| P27 | 0.047 | 0.040 | 0.097 |
| P28 | 0.054 | -0.046 | 0.015 |
| P30 | 0.007 | -0.031 | -0.001 |
| P31 | -0.048 | -0.033 | -0.042 |
| **Parameter** | **X error (*ft*)** | **Y error (*ft*)** | **Z error (*ft*)** |
| **No. Points =** | 20 | 20 | 20 |
| **Min (*ft*) =** | -0.056 | -0.095 | -0.097 |
| **Max (*ft*) =** | 0.090 | 0.080 | 0.097 |
| **Mean (*ft*) =** | 0.037 | -0.027 | 0.003 |

| | | | |
|---|---|---|---|
| **Std Dev (*ft*) =** | 0.042 | 0.051 | 0.062 |
| **RMSE (*ft*) =** | 0.055 | 0.056 | 0.061 |
| **NVA 95% (*ft*) =** | | | 0.119 |
| **RMSE R (*ft*) =** | 0.079 | | |
| **Case 1 95% CE (*ft*) =** | 0.137 | | |
| **Case 2 ~ CE (*ft*) =** | 0.137 | | |

**Table 9.36 Checkpoints Accuracy Located on the Above Road from Agisoft (Area 1)**

| **Point** | **X error (*ft*)** | **Y error (*ft*)** | **Z error (*ft*)** |
|---|---|---|---|
| P13 | -0.030 | -0.073 | -0.016 |
| P14 | 0.052 | 0.053 | -0.092 |
| P15 | 0.051 | 0.003 | -0.061 |
| P17 | 0.042 | 0.006 | -0.083 |
| P18 | 0.080 | -0.049 | -0.079 |
| P19 | 0.074 | 0.075 | -0.068 |
| P23 | 0.064 | 0.004 | -0.040 |
| P25 | -0.010 | 0.058 | -0.078 |
| P26 | 0.012 | 0.071 | -0.067 |
| P27 | -0.051 | 0.030 | -0.043 |
| P28 | 0.059 | 0.059 | -0.074 |
| P30 | 0.034 | 0.074 | 0.001 |
| P31 | -0.014 | 0.009 | 0.072 |
| **Parameter** | **X error (*ft*)** | **Y error (*ft*)** | **Z error (*ft*)** |
| **No. Points =** | 13 | 20 | 20 |
| **Min (*ft*) =** | -0.051 | -0.073 | -0.092 |
| **Max (*ft*) =** | 0.080 | 0.075 | 0.072 |
| **Mean (*ft*) =** | 0.028 | 0.025 | -0.048 |
| **Std Dev (*ft*) =** | 0.042 | 0.047 | 0.045 |
| **RMSE (*ft*) =** | 0.049 | 0.052 | 0.065 |
| **NVA 95% (ft) =** | | | 0.127 |
| **RMSE R (*ft*) =** | 0.071 | | |
| **Case 1 95% CE (*ft*) =** | 0.123 | | |
| **Case 2 ~ CE (*ft*) =** | 0.123 | | |

**Table 9.37 Checkpoints Accuracy Located on the Road Panel from Agisoft (Area 2)**

| **Point** | **X error (*ft*)** | **Y error (*ft*)** | **Z error (*ft*)** |
|---|---|---|---|
| P1 | 0.001 | 0.008 | -0.061 |
| P3 | -0.042 | 0.060 | 0.016 |
| P4 | -0.054 | -0.044 | 0.004 |

| | | | |
|---|---|---|---|
| P6 | -0.097 | 0.079 | 0.012 |
| P7 | -0.059 | 0.075 | -0.022 |
| P8 | -0.073 | 0.034 | 0.065 |
| P10 | -0.022 | 0.015 | 0.049 |
| **Parameter** | **X error (*ft*)** | **Y error (*ft*)** | **Z error (*ft*)** |
| **No. Points =** | 7 | 7 | 7 |
| **Min (*ft*) =** | -0.097 | -0.044 | -0.061 |
| **Max (*ft*) =** | 0.001 | 0.079 | 0.065 |
| **Mean (*ft*) =** | -0.050 | 0.032 | 0.009 |
| **Std Dev (*ft*) =** | 0.033 | 0.044 | 0.042 |
| **RMSE (*ft*) =** | 0.058 | 0.052 | 0.040 |
| **NVA 95% (*ft*) =** | | | 0.079 |
| **RMSE R (*ft*) =** | 0.078 | | |
| **Case 1 95% CE (*ft*) =** | 0.135 | | |
| **Case 2 ~ CE (*ft*) =** | 0.135 | | |

**Table 9.38 Checkpoints Accuracy Located on the Above Road from Pix4D (Area 1)**

| **Point** | **X error (*ft*)** | **Y error (*ft*)** | **Z error (*ft*)** |
|---|---|---|---|
| P13 | 0.066 | 0.009 | -0.018 |
| P14 | 0.086 | 0.066 | 0.036 |
| P15 | 0.010 | -0.081 | -0.014 |
| P17 | 0.006 | -0.093 | 0.060 |
| P18 | -0.080 | 0.061 | 0.100 |
| P19 | -0.098 | -0.050 | 0.100 |
| P23 | 0.049 | -0.069 | 0.078 |
| P25 | -0.034 | -0.062 | 0.050 |
| P26 | 0.031 | -0.024 | 0.069 |
| P27 | 0.012 | 0.058 | -0.043 |
| P28 | 0.033 | -0.009 | 0.010 |
| P30 | 0.046 | -0.012 | 0.037 |
| P31 | 0.034 | 0.043 | 0.014 |
| **Parameter** | **X error (*ft*)** | **Y error (*ft*)** | **Z error (*ft*)** |
| **No. Points =** | 13 | 20 | 20 |
| **Min (*ft*) =** | -0.098 | -0.093 | -0.043 |
| **Max (*ft*) =** | 0.086 | 0.066 | 0.100 |
| **Mean (*ft*) =** | 0.012 | -0.012 | 0.037 |
| **Std Dev (*ft*) =** | 0.054 | 0.057 | 0.045 |
| **RMSE (*ft*) =** | 0.053 | 0.056 | 0.057 |
| **NVA 95% (ft) =** | | | 0.111 |

| | | | |
|---|---|---|---|
| **RMSE R (*ft*) =** | 0.077 | | |
| **Case 1 95% CE (*ft*) =** | 0.133 | | |
| **Case 2 ~ CE (*ft*) =** | 0.133 | | |

**Table 9.39 Checkpoints Accuracy Located on the Road Panel from Pix4D (Area 2)**

| **Point** | **X error (*ft*)** | **Y error (*ft*)** | **Z error (*ft*)** |
|---|---|---|---|
| P1 | 0.021 | 0.081 | 0.017 |
| P3 | -0.050 | 0.080 | -0.106 |
| P4 | 0.061 | 0.074 | 0.076 |
| P6 | -0.021 | 0.032 | -0.081 |
| P7 | -0.046 | 0.024 | -0.030 |
| P8 | -0.050 | -0.034 | -0.068 |
| P10 | 0.029 | 0.055 | 0.030 |
| **Parameter** | **X error (*ft*)** | **Y error (*ft*)** | **Z error (*ft*)** |
| **No. Points =** | 7 | 7 | 7 |
| **Min (*ft*) =** | -0.050 | -0.034 | -0.106 |
| **Max (*ft*) =** | 0.061 | 0.081 | 0.076 |
| **Mean (*ft*) =** | -0.008 | 0.045 | -0.023 |
| **Std Dev (*ft*) =** | 0.045 | 0.041 | 0.066 |
| **RMSE (*ft*) =** | 0.042 | 0.059 | 0.066 |
| **NVA 95% (*ft*) =** | | | 0.129 |
| **RMSE R (*ft*) =** | 0.072 | | |
| **Case 1 95% CE (*ft*) =** | 0.125 | | |
| **Case 2 ~ CE (*ft*) =** | 0.124 | | |

**Table 9.40 Checkpoints Accuracy Located on the Above Road from UASMaster (Area 1)**

| **Point** | **X error (*ft*)** | **Y error (*ft*)** | **Z error (*ft*)** |
|---|---|---|---|
| P13 | 0.045 | 0.080 | 0.059 |
| P14 | 0.059 | -0.062 | -0.058 |
| P15 | 0.046 | -0.082 | -0.069 |
| P17 | 0.040 | -0.051 | -0.050 |
| P18 | -0.056 | -0.040 | 0.046 |
| P19 | -0.052 | -0.075 | 0.064 |
| P23 | 0.066 | -0.095 | -0.035 |
| P25 | 0.051 | -0.037 | 0.020 |
| P26 | 0.063 | -0.063 | -0.059 |
| P27 | 0.047 | 0.040 | 0.097 |
| P28 | 0.054 | -0.046 | 0.015 |
| P30 | 0.007 | -0.031 | -0.001 |

| | | | |
|---|---|---|---|
| P31 | -0.048 | -0.033 | -0.042 |
| **Parameter** | **X error (*ft*)** | **Y error (*ft*)** | **Z error (*ft*)** |
| **No. Points =** | 13 | 20 | 20 |
| **Min (*ft*) =** | -0.056 | -0.095 | -0.069 |
| **Max (*ft*) =** | 0.066 | 0.080 | 0.097 |
| **Mean (*ft*) =** | 0.025 | -0.038 | -0.001 |
| **Std Dev (*ft*) =** | 0.046 | 0.048 | 0.055 |
| **RMSE (*ft*) =** | 0.051 | 0.060 | 0.053 |
| **NVA 95% (*ft*) =** | | | 0.104 |
| **RMSE R (*ft*) =** | 0.079 | | |
| **Case 1 95% CE (*ft*) =** | 0.136 | | |
| **Case 2 ~ CE (*ft*) =** | 0.136 | | |

**Table 9.41 Checkpoints Accuracy Located on the Road Panel UASMaster (Area 2)**

| **Point** | **X error (*ft*)** | **Y error (*ft*)** | **Z error (*ft*)** |
|---|---|---|---|
| P1 | 0.050 | 0.056 | 0.094 |
| P3 | 0.080 | 0.031 | 0.062 |
| P4 | 0.031 | -0.065 | 0.083 |
| P6 | 0.090 | -0.040 | 0.028 |
| P7 | 0.040 | -0.049 | -0.013 |
| P8 | 0.058 | -0.036 | -0.097 |
| P10 | 0.066 | 0.054 | -0.086 |
| **Parameter** | **X error (*ft*)** | **Y error (*ft*)** | **Z error (*ft*)** |
| **No. Points =** | 7 | 7 | 7 |
| **Min (*ft*) =** | 0.031 | -0.065 | -0.097 |
| **Max (*ft*) =** | 0.090 | 0.056 | 0.094 |
| **Mean (*ft*) =** | 0.059 | -0.007 | 0.010 |
| **Std Dev (*ft*) =** | 0.021 | 0.052 | 0.078 |
| **RMSE (*ft*) =** | 0.062 | 0.049 | 0.073 |
| **NVA 95% (*ft*) =** | | | 0.143 |
| **RMSE R (*ft*) =** | 0.079 | | |
| **Case 1 95% CE (*ft*) =** | 0.137 | | |
| **Case 2 ~ CE (*ft*) =** | 0.136 | | |

***LiDAR Data Evaluation***

For the LiDAR data collection performed on September 30th, 2020, one LiDAR dataset was collected using 262 *ft* flight height with 80° FOV with 50% overlap. 29 points were used as control points to merge all the scans. 20 checkpoints (P1, P3, P4, P6, P7, P8, P10, P13, P14, P15, P17, P18, P19, P23, P25, P26, P27, P28, P30, and P31) were used to calculate the accuracy. For the

LiDAR data collection performed on March 09th, 2021, one LiDAR dataset was collected using 262 *ft* flight height with 56° FOV with 60% overlap. 11 points were used as control points to merge all the scans. The same 20 checkpoints were used to calculate the accuracy. Table 9.42 shows the detailed results.

**Table 9.42 LiDAR Checkpoints Accuracy at I-26 Rock Surface Site**

| | | 09/30/2020 | | 03/09/2021 | |
|---|---|---|---|---|---|
| **Control Points** | **Known Z** | **LiDAR Z** | **Difference** | **LiDAR Z** | **Difference** |
| P1 | 3364.204 | 3364.13 | -0.074 | 3364.220 | 0.016 |
| P3 | 3366.588 | 3366.68 | 0.092 | 3366.580 | -0.008 |
| P4 | 3365.186 | 3365.25 | 0.064 | 3365.290 | 0.104 |
| P6 | 3359.363 | 3359.2 | -0.163 | 3359.380 | 0.017 |
| P7 | 3354.799 | 3354.77 | -0.029 | 3354.760 | -0.039 |
| P8 | 3349.374 | 3349.5 | 0.126 | 3349.420 | 0.046 |
| P10 | 3335.448 | 3335.39 | -0.058 | 3335.490 | 0.042 |
| P13 | 3523.727 | 3523.7 | -0.027 | 3577.780 | 0.062 |
| P14 | 3577.718 | 3577.57 | -0.148 | 3617.320 | 0.048 |
| P15 | 3617.272 | 3617.2 | -0.072 | 3613.170 | 0.023 |
| P17 | 3569.906 | 3569.79 | -0.116 | 3569.870 | -0.036 |
| P18 | 3522.335 | 3522.25 | -0.085 | 3522.440 | 0.105 |
| P19 | 3465.128 | 3465.03 | -0.098 | 3465.160 | 0.032 |
| P23 | 3563.979 | 3563.86 | -0.119 | 3564.030 | 0.051 |
| P25 | 3503.779 | 3503.69 | -0.089 | 3503.880 | 0.101 |
| P26 | 3561.122 | 3561.05 | -0.072 | 3561.090 | -0.032 |
| P27 | 3462.709 | 3462.73 | 0.021 | 3462.820 | 0.111 |
| P28 | 3505.299 | 3505.11 | -0.189 | 3505.330 | 0.031 |
| P30 | 3423.694 | 3423.39 | -0.304 | 3423.740 | 0.046 |
| P31 | 3374.427 | 3374.37 | -0.057 | 3374.265 | -0.162 |
| **Min (*ft*) =** | | | -0.304 | | -0.139 |
| **Max (*ft*) =** | | | +0.189 | | 0.162 |
| **Mean =** | | | -0.070 | | 0.028 |
| **Std Dev. (*ft*) =** | | | 0.098 | | 0.064 |
| **RMSE (*ft*) =** | | | 0.119 | | 0.068 |
| **NVA 95% (*ft*) =** | | | 0.233 | | 0.133 |

## Appendix II: Guidelines and Recommendations for UAS-based Photogrammetric Surveying Accuracy

### *Purpose*

This document contains a set of guidelines and recommendations that can be used to achieve consistent and reliable accuracy for survey-grade geospatial products using unmanned aerial systems (UAS) equipped with digital cameras. It focuses on different terrain types for preconstruction, construction, and sloped sites. It will also help assess and improve the quality of survey data. It summarizes the findings from previous North Carolina Department of Transportation (NCDOT) reports, data collection, and evaluations from six different study sites, including a track facility and Lake Raleigh on North Carolina State University (NCSU) campus, NCDOT UAS Test Site in Butner, the U2412-A construction site in High Point, R2303-E pit site at Clinton, and I-26 rock surface in Mars Hill.

### *Scope and Applicability*

This document can be used by any practitioners who want to use UAS-based photogrammetry on surveying and mapping to generate survey-grade geospatial products for preconstruction, construction, and rock slope sites. Its scope is limited to non-vegetated areas and the use of indirect georeferencing that uses ground control points (GCP). The word “survey” in this document refers to a photogrammetry-based survey using UAS equipped with a digital camera.

### *Authority*

The responsible organization for preparing, maintaining, and coordinating work on this guideline is the NCSU research team and NCDOT.

### *Structure and Format*

This document is structured as follows: the primary terms and definitions, background information, and detailed guidelines and recommendations.

***Terms and definitions***

The terms and definitions listed below are also used in the American Society for Photogrammetry and Remote Sensing (ASPRS) Positional Accuracy Standards for Digital Geospatial Data, Edition 1, Version 1.0. (2015).

| Term | Definitions |
|---|---|
| Absolute Accuracy | A measure that accounts for all systematic and random errors in a data set. |
| Checkpoints | Points with known coordinates that are used to validate the accuracy of the survey as an independent source. |
| Ground Control Points (GCPs) | The points that the surveyors can precisely pinpoint with a handful of known coordinates in an aerial survey. GCPs can be anything that is easily recognized in the images. |
| Ground Sample Distance (GSD) | The linear dimension of a sample pixel's footprint on the ground. |
| Horizontal Accuracy | The horizontal (radial) component of the positional accuracy of a data set with respect to a horizontal datum, at a specified confidence level. |
| Local Accuracy | The uncertainty in the coordinates of points with respect to coordinates of other directly connected, adjacent points at the 95% confidence level. |
| Non-Vegetated Vertical Accuracy (NVA) | The vertical accuracy at the 95% confidence level in non-vegetated open terrain, where errors should approximate a normal distribution. |
| Pixel Resolution or Pixel Size | As used within this document, pixel size is the ground size of a pixel in a digital orthoimage, after all rectifications and resampling procedures. |
| Positional Error | The difference between data set coordinate values and coordinate values from an independent source of higher accuracy for identical points. |
| Positional Accuracy | The accuracy of the position of features, including horizontal and vertical positions, with respect to horizontal and vertical datums. |
| Relative Accuracy | A measure of variation in point-to-point accuracy in a data set. |
| Resolution | The smallest unit a sensor can detect or the smallest unit an orthoimage depicts. The degree of fineness to which a measurement can be made. |
| Root Mean Square Error (RMSE) | The square root of the average of the set of squared differences between data set coordinate values and coordinate values from an independent source of higher accuracy for identical points. |
| Systematic Error | An error whose algebraic sign and, to some extent, magnitude bears a fixed relation to some condition or set of conditions. Systematic errors follow some fixed pattern and are introduced by data collection procedures, processing or given datum. |

| | |
|---|---|
| Vertical Accuracy | The measure of the positional accuracy of a data set with respect to a specified vertical datum, at a specified confidence level or percentile. |

***Background***

UAS and photogrammetry together can be an effective way of producing 3D geospatial data with relatively low cost. However, they often produce inconsistent and unreliable survey results, in part because there are no good guidelines that can ensure the quality and consistency. Without proper guidelines, repeated surveying at a designated area over time (e.g., a construction site with periodic data collection) can result in unreliable data.

***Guidelines and Recommendations***

This section presents guidelines and recommendations that can help reduce inconsistency and achieve more accurate and reliable survey data. It contains the following three sections: data acquisition, data processing, and quality assessment.

***Data Acquisition***

This section presents multiple factors of data acquisition that affect survey results.

*Ground Sample Distance (GSD) and Accuracy*

GSD is the distance between two consecutive pixel centers measured on the ground. In simpler terms, GSD represents the size of one pixel on the ground. GSD is calculated based on the flight height (the distance from the terrain or object), the image width (or the image height), sensor width (or the sensor height), and focal length. When calculating the GSD, the worse (larger) value of the results from two different calculations is used:

$$GSD_h = \frac{Flight\ Height \times Sensor\ Height}{Focal\ Lenth\ \times Image\ Height}$$
$$GSD_w = \frac{Flight\ Height \times Sensor\ Width}{Focal\ Lenth\ \times Image\ Width}$$

A higher value of GSD means a lower spatial resolution of an image and less visible details.

Thus, when a detailed survey of the area is needed, maintaining a low GSD is suggested. There are two ways to decrease GSD:

- If an altitude is fixed due to site constraints, increasing the focal length (zoom-in or change the camera lens),
- If a focal length is fixed due to limited resources, decreasing the altitude.

On the other hand, when covering large areas that do not need very detailed results, having a higher GSD by flying at a higher altitude or decreasing the focal length can reduce the acquisition time, the number of batteries to be used, and the processing time.

The maximum horizontal accuracy that can be achieved can be estimated by multiplying GSD by an approximated GCP selection error (see Appendix III and Figure 9.28 for details). The GCP selection error can range from 1-3 pixels if a user of 3D photogrammetry software makes very careful selection. However, that can be very time consuming. This selection error can easily increase as flight height increases because GCP targets will appear smaller.

*Distribution and Separation Distance of Ground Control Points*

The GCP quantity, distribution, and spacing can impact the accuracy. Evenly distributed GCPs generate more accurate results than random distribution. Also, increasing the number of GCPs can improve the accuracy. Additionally, reducing the distance between GCPs can increase the accuracy. To achieve a horizontal accuracy of the selection error times GSD, the GCP spacing should be equal to or less than 262 *ft* (80 *m*). The last section of Appendix III provides details of how GCP spacing affects the accuracy.

*Image Overlap*

Increasing overlaps will improve the survey accuracy. The recommended overlap for most cases is at least 70% forward overlap and at least 70% side overlap. Moreover, for some cases with complex terrains, including vegetation areas, slopes, or construction sites, a high image overlap should be applied (for example, at least 80% forward and side overlap).

*Camera Shooting Angle*

Either nadir or oblique images can be utilized in the project based on the sites. Nadir images are shot with the camera axis along the vertical direction, which allows for the reconstruction of the surveyed territory or object in 3D. However, it is not appropriate for the 3D modeling of buildings. Thus, under this circumstance, integrating oblique images (are shot with the camera axis at an angle with respect to the vertical) capturing the building themselves with nadir images will improve the 3D model reconstruction and further improve the accuracy of the results.

Thus, it is recommended to capture both nadir and oblique images for the building or facility sites to improve the 3D model completeness and accuracy.

*Camera Settings*

In most cases, the shutter speed, aperture, and ISO of the cameras can be set on automatic. However, if images are blurry or noisy, it is recommended to set these parameters manually based on the weather and lighting conditions. The images should be sharp and have the least amount of noise.

The white balance can be set as sunny or daylight or some equivalent mode to balance the quality of light and color. A low ISO (100-200, the minimum is 100) can be used to reduce the noise, a high aperture (f/4 or higher) should be applied to increase the depth of field, and a high shutter speed (more than 1/300 second) should be applied to reduce the motion blur. The following is an example of desirable camera settings when the aperture is f/1.8 when the weather is sunny. Note

that these settings are weather dependent. Moreover, these settings should be changed for a lens with a different aperture value (f/#). For instance, a cheaper lens will typically have higher f/#, resulting in darker images with a low ISO, so ISO and shutter speed needs to be adjusted (higher and slower, respectively).

White Balance: Daylight (or 5500K -6500K)
ISO: 100
Shutter Speed: 1/6400 sec (+/-)

*Image Quality*

The quality of the image should be checked before starting the data processing. The poor-quality images should be excluded from photogrammetric processing. Some of the SfM software (i.e., Agisoft) quantifies image quality. For example, the image quality by Agisoft ranges from 0 to 1. The quality value is calculated based on the sharpness level of the most focused part of the picture. The images with quality values less than 0.5 should be removed from data processing. However, if the software does not automatically identify image qualities, the user should manually inspect images to identify and remove low-quality images, such as blurry images.

## ***Data Processing***

In this section, the guidelines and recommendations for data processing are presented.

*Camera Calibration*

There are two ways to calibrate cameras: pre-calibration before the mission for each camera or calibration as part of structure-from-motion (SfM – 3D modeling by photogrammetry software). When pre-calibration is performed, all camera settings should be fixed. Any change to the fixed camera settings (including autofocus and zoom) can cause inconsistent results. If autofocus is used or if camera settings will be changed, calibration during SfM should be used. Moreover, pre-calibration should be performed multiple times to make sure that consistent intrinsic parameters are achieved. When a video is taken, pre-calibration should be used. For photos, both pre-calibration and calibration as part of SfM can be used.

*Software Processing Procedures*

This subsection presents a recommended workflow for processing data using Agisoft. Users can adjust the following procedures based on their drones and processing software.

- Import Photos
- Manually remove images that are obvious ‘outliers’ (e.g., images that have been taken before take-off, etc.)
- Convert GPS coordinates of your geotagged images (WGS84) to match the coordinate system of your ground control points (GCPs) which will be imported later.
- Estimate image quality. Disable all images that have an image quality below 0.5
- Generate masks if necessary.

- Align photos (quality HIGH, pair preselection: REFERENCE, key point limit: 40,000, tie point limit: 4,000, adaptive camera model fitting: YES).
- Import list of ground control points (also include the X/Y/Z accuracy values)
- Verify and link markers to images (use FILTER BY MARKERS by right-clicking on GCP). Mark each GCP in at least 3-6 images. When finished, press the UPDATE button in the reference pane.
- Uncheck all images in the reference pane and also uncheck checkpoints.
- Clean sparse point cloud (MODEL > GRADUAL SELECTION). Remove all points with high reprojection error (choose a value below 1, the value between 0.5-0.8 is suggested) and high reconstruction uncertainty (try to find the 'natural threshold' by moving the slider).
- Adjust your bounding box
- Optimize camera alignment (magic wand button)
- Build dense cloud (choose HIGH or MEDIUM quality, but it depends on what you want to do with the data and on your hardware, including CPU, GPU, and RAM)
- Build mesh (not needed if you just want a DEM and/or orthophotograph)
- Build texture (not needed if you just want a DEM and/or orthophotograph)
- Build DEM (from the dense cloud)
- Build Orthomosaic based on DEM

***Quality Assessment***

In this section, the guidelines and recommendations for assessing quality of survey results are presented.

*Principle of Image-based 3D Reconstruction*

To assess photogrammetry-based survey results, understanding the basic concepts of image-based 3D reconstruction is very important. 3D reconstruction is a pipeline of algorithms that detects and matches visual features from images, estimates 3D points and calibrates the camera (SfM), and performs optimization (bundle adjustment) as more features and images are processed (see Figure 9.19 and Figure 9.20). After all data is processed, the estimated 3D points are back-projected onto each image to calculate the reprojection errors (see Figure 9.21).

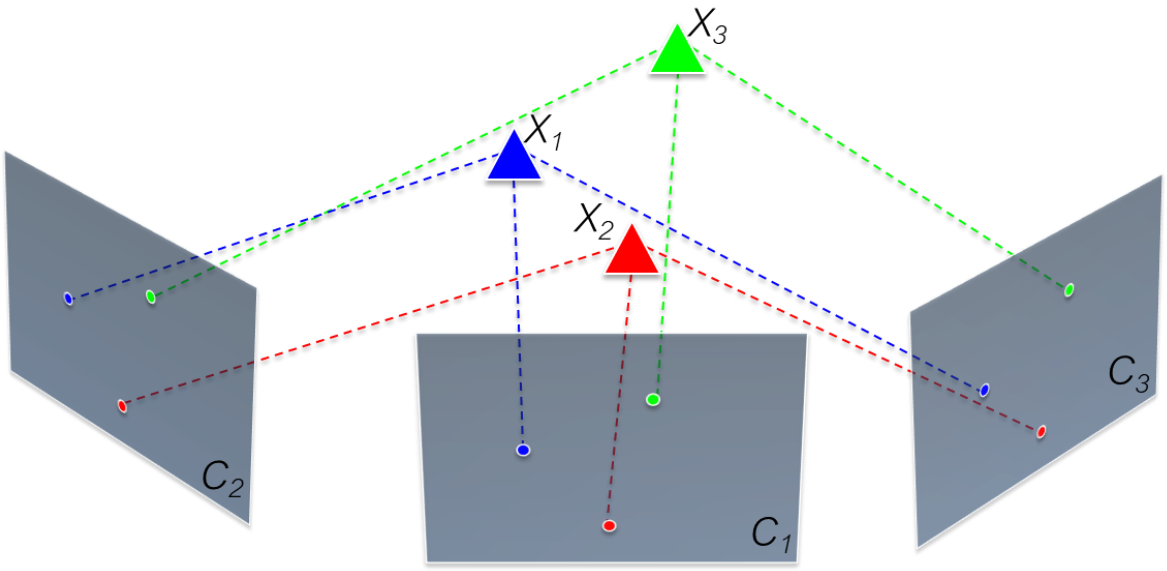


**Figure 9.19 Structure from Motion**

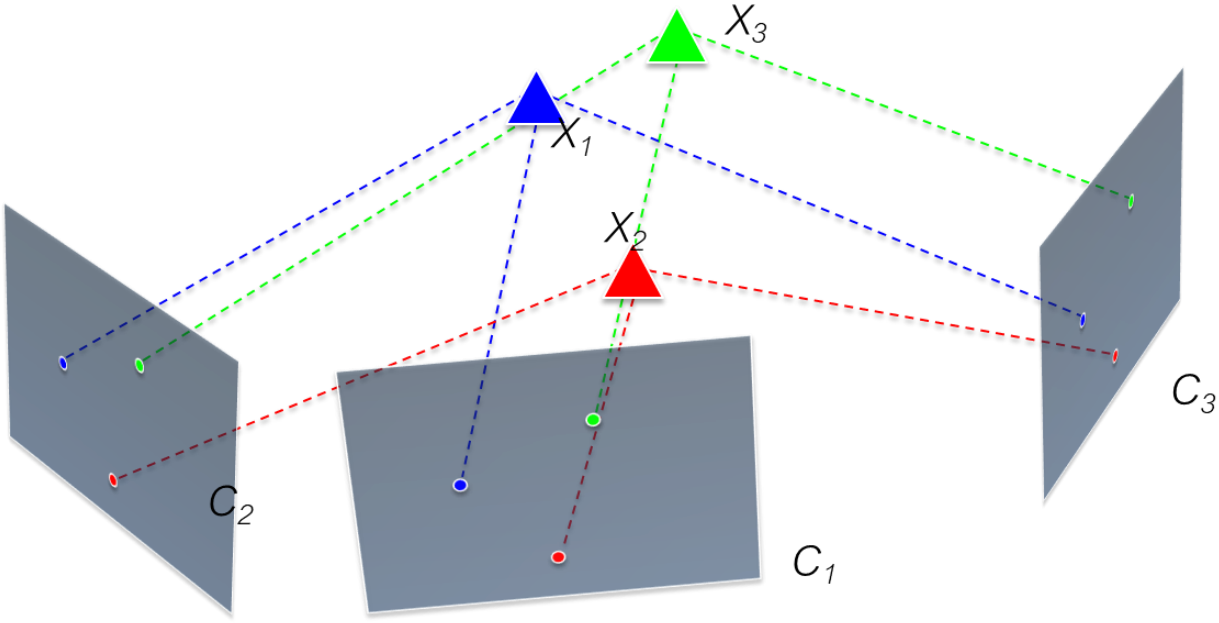


**Figure 9.20 Bundle Adjustment (BA)**

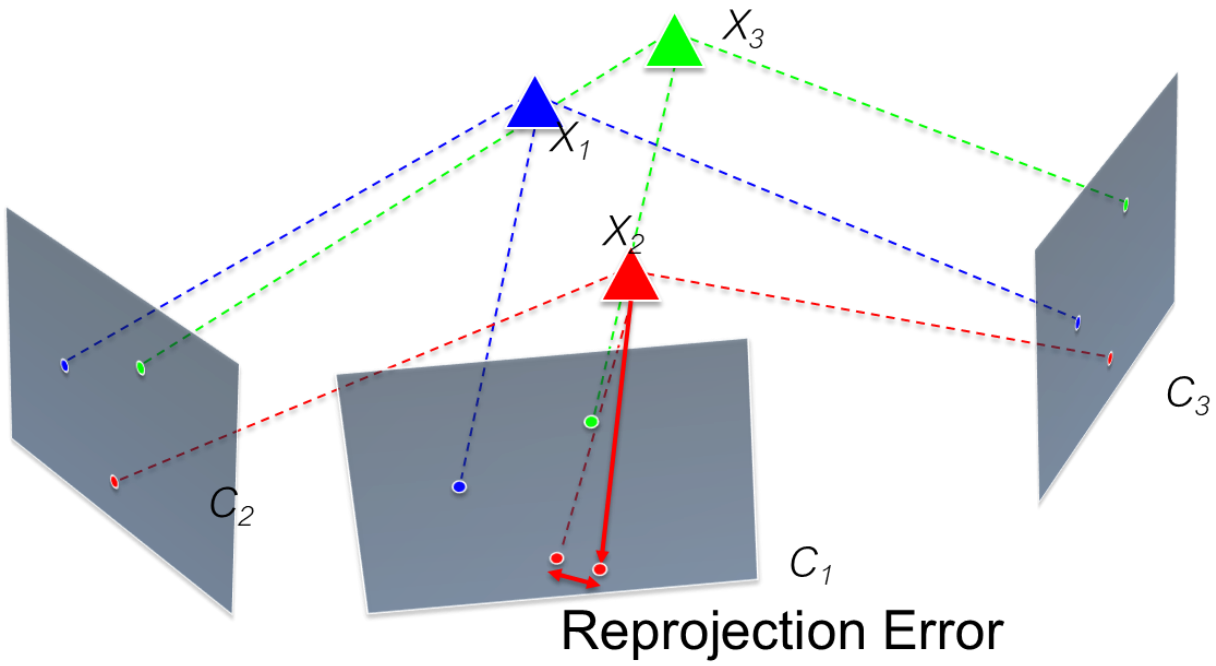


**Figure 9.21 SfM & BA Minimizes Reprojection Error**

*3D Point Cloud Reconstruction Using Ground Control Points*

GCPs can be measured using traditional surveying methods (i.e., total station), or measured using the global navigation satellite system (GNSS), GCPs with GNSS built-in, LiDAR, or an existing map. Since GCPs have specific geolocations, they are used during the data processing step to reduce the marginal errors of GPS data from the images (GPS data can have a margin of error of up to 3 *ft*, depending on conditions at the site) and to accurately georeference and calibrate your images.

There are also real-time kinematic (RTK) equipped UAS that can store high precision GPS information. In addition, Post-Processed Kinematic (PPK) that uses base station data to correct and improve the accuracy of RTK's GPS information. Despite the claims by the manufacturer, accuracy of these technologies was not reliable based on the research team's evaluation of NCDOT's data that was collected using a Loki system. The evaluation shows that GCPs were still needed to produce an accurate survey result. However, this evaluation was based on PPK using a base station instead of GCPs with GNSS built in. Further investigation is needed if NCDOT wants to examine the Loki system with GCPs with GNSS built-in (i.e., AeroPoints).

*Decreasing Reprojection Error*

The reprojection error (defined previously in Section *Principle of Image-based 3D Reconstruction*) is a type of measure that shows how accurately a 3D point that makes up a point cloud is created. Multiple factors can cause an excessive number of 3D points (often referred as tie points by photogrammetry software) with high reprojection errors. These factors are, but not limited to:

- Blurry or poorly exposed images.
- An insufficient number of tie point.
- An insufficient number of tie point marks on images.
- Inaccurate tie point marks on one or more images.

The reprojection error corresponds to the image distance between a projected point and a measured one. Poor quality images can fail the feature detection and SfM camera calibration to further affect the image distance measurement. Thus, to decrease the reprojection error, only high-quality images should be used. A sufficient number of tie points, the number of GCPs, and the number of images marked by GCPs are required as well.

Based on the camera resolutions and the lens, a recommended average reprojection error varies. However, it should be less than or equal to one pixel.

*Individual Errors at Each Checkpoint*

The positional error at each checkpoint varies and needs to be evaluated. The number of images marked using checkpoints (often known as reprojection or registered images) can affect the accuracy. Checkpoints with fewer reprojections (less than 10) have lower positional accuracy, especially in the vertical direction, than checkpoints with more images.

When there is less than 10 reprojections and undesirable local accuracy, either more images with better quality and sufficient overlap (see to *Data Acquisition* Section) need to be collected and added to the current set of images or the guidelines below should be followed.

*Point Clouds Accuracy Improvement and Generating Consistent Quality from Images*

The output of SfM (i.e., position and orientation of the cameras) can be verified and improved by removing or fixing bad tie points with high reprojection errors or incorrect alignment and adding new manual tie points. Figure 9.22 illustrates how to fix the inconsistent models by removing the bed tie points and adding manual tie points.

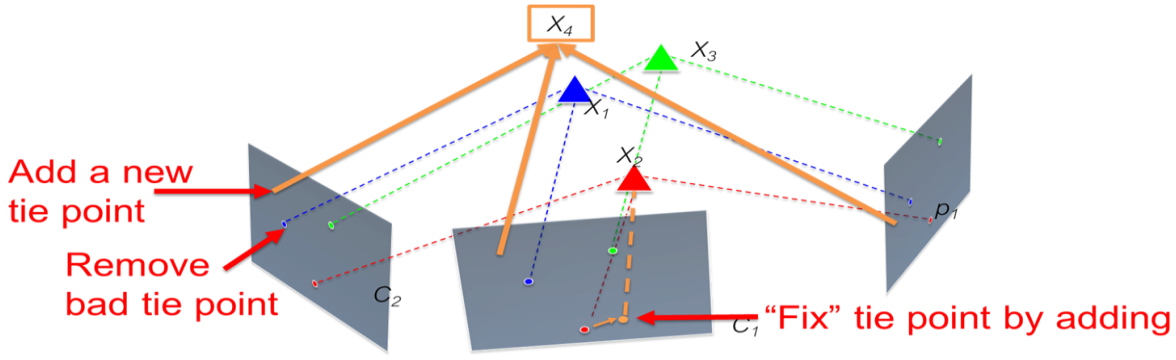


**Figure 9.22 Point Clouds Accuracy Improvement**

Each software provides different features for performing these improvements. For instance, Agisoft has a Graduation Selection tool that can be used to filter out the points that are below desired quality. Below are the three steps for using this tool:

1) Reconstruction Uncertainty – Level 10. Do it twice if necessary → run Optimization
2) Reprojection Error – Level 0,5 → run Optimization
3) Projection Accuracy – 10% of total points → run Optimization

The following Figures 9.23 – 9.25 show an example of these steps. In this example, 1,960,352 out of 2,561,589 points are selected after the first step. After deleting those points, the Optimization function is performed. With the second step, 16, 821 out of 601, 237 points are selected and removed. With the last step 27,989 out of 584,416 points are selected and removed.

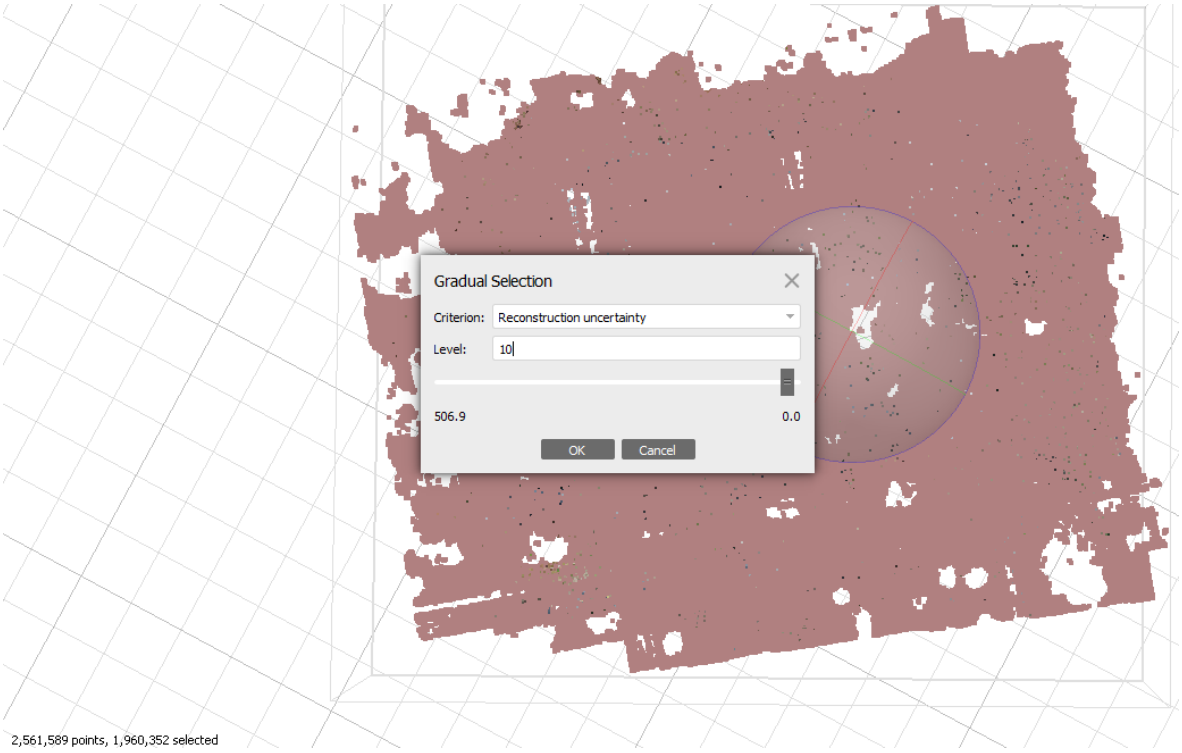


**Figure 9.23 Reconstruction Uncertainly – Level 10**

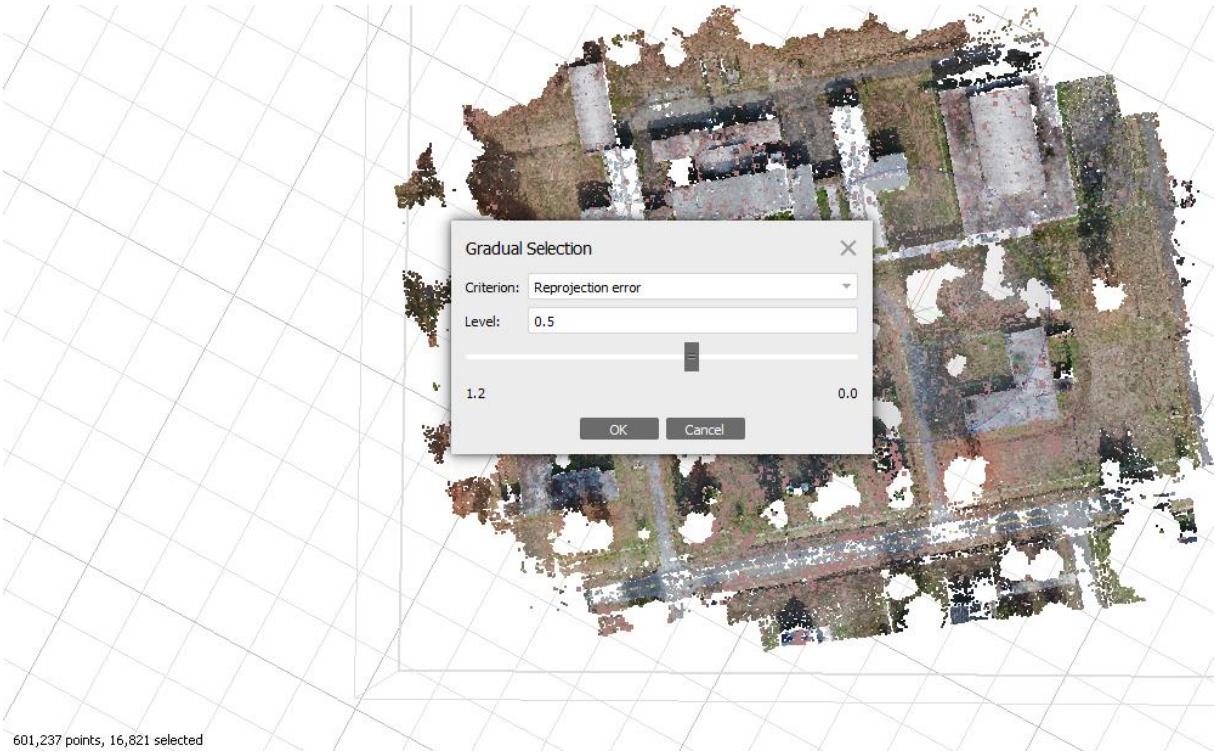


**Figure 9.24 Reprojection Error – Level 0,5**

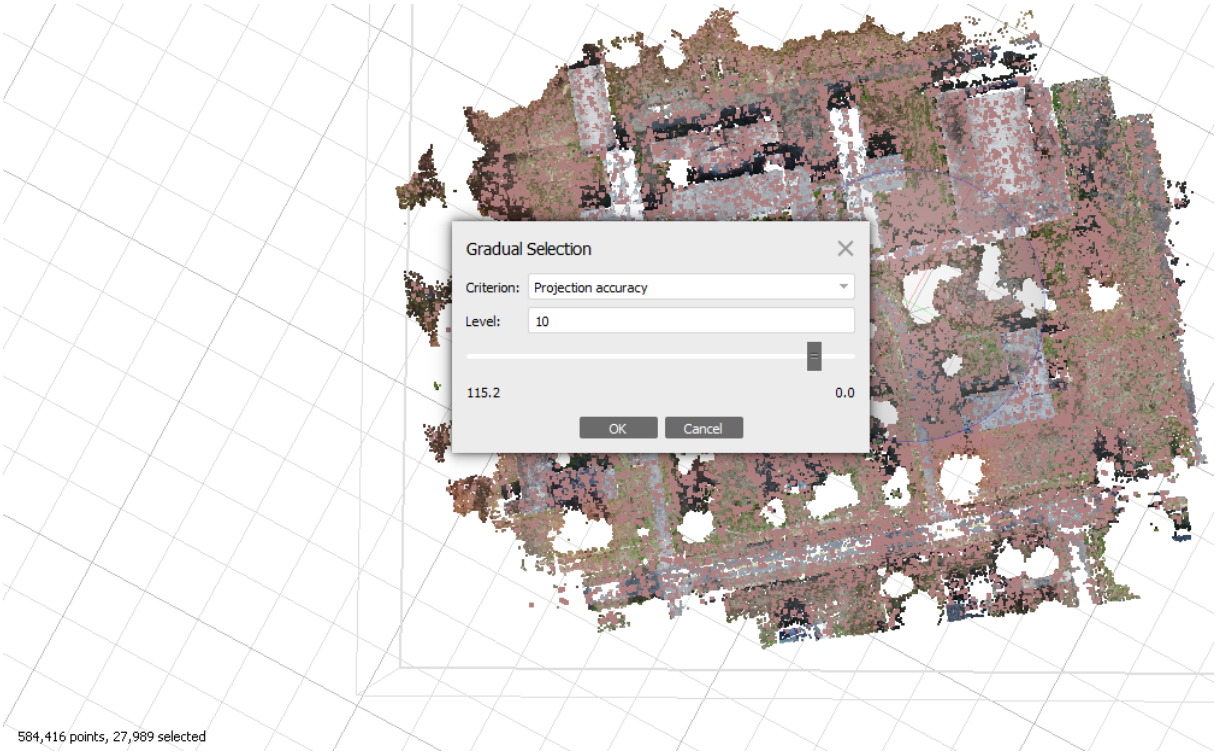


**Figure 9.25 Projection Accuracy – 10% of total points.**

Pix4D allows adding new manual tie points, which replace inaccurate tie points. The following figures show an example of how to add manual tie points in Pix4D. Figure 9.26 shows an

automatic tie point that was inserted during SfM by Pix4D. The maximal orthogonal ray distance in easting is -0.167, which is high. Thus, a new manual tie point can be added to fix it. Figure 9.27 shows the newly added manual tie point. The maximal orthogonal ray distance in easting is -0.036, which is reasonable. Thus, the method can improve the model accuracy.

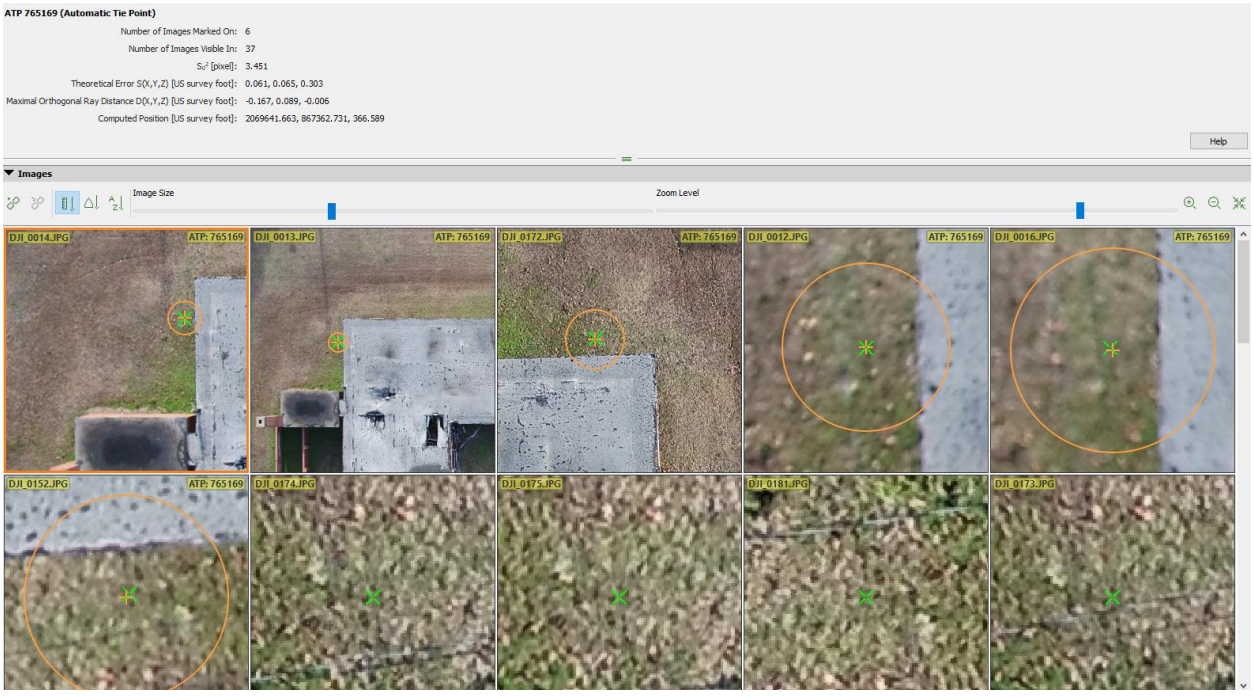


**Figure 9.26 "Bad" Tie Point**

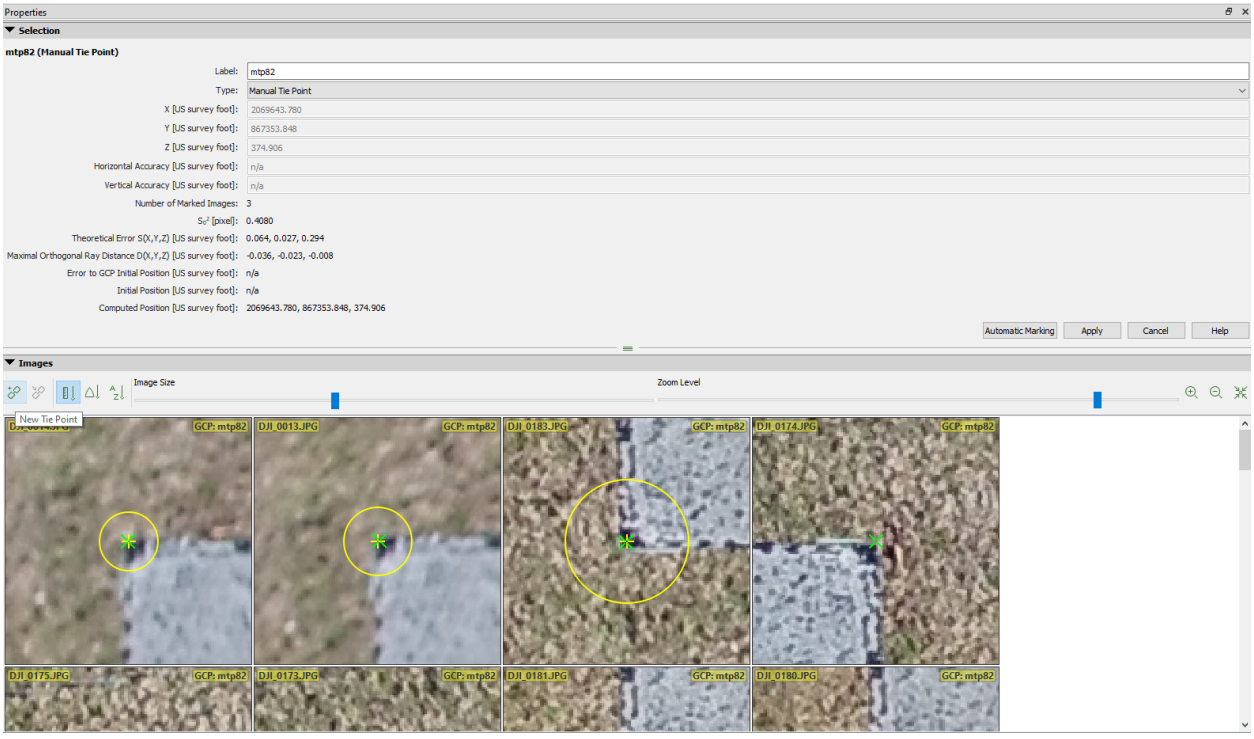


**Figure 9.27 Adding New Tie Point**

***Additional Recommendation – Development of Accuracy Prediction Model***

In an effort to evaluate different factors that influence survey accuracy, the NCSU research team developed a multiple regression (MR) model. This model also can be used as a prediction model that predicts expected survey accuracy. NCDOT may benefit from building their own prediction using their own hardware and software for common terrain types of their interest. The development and results of the MR model are detailed in Appendix IV.

**Appendix III: Specifications for UAS-based Photogrammetric Surveying Accuracy**

This document provides instructions on how to estimate the maximum accuracy, given the site conditions, ground control point (GCP) placement, and hardware information. NCDOT can use the information in this document to develop a set of specifications for surveying preconstruction, construction, and sloped site. The set of specifications include the maximum accuracy and required GCP accuracy and spacing. This document can be used by NCDOT to produce their own surveying data. It can also help NCDOT develop specifications for its subcontractors and ensure they produce reasonable and reliable surveying data. This document contains three aspects – maximum accuracy estimation, GCP accuracy, and GCP placement.

***Maximum Accuracy Estimation***

The ground sampling distance (GSD) represents the size of one pixel on the ground. The maximum accuracy is dictated by GSD. GSD is determined by the flight height (the distance from the terrain or object), the image width (or the image height), sensor width (or the sensor height), and focal length. When calculating the GSD, the worse (larger) value of the results from two different calculations is used:

$$GSD_h = \frac{Flight\ Height \times Sensor\ Height}{Focal\ Lenth\ \times Image\ Height}$$

$$GSD_w = \frac{Flight\ Height \times Sensor\ Width}{Focal\ Lenth\ \times Image\ Width}$$

Another factor is error in marking the exact center of the GCP targets when using SfM software. As shown in Figure 9.28, there could easily be selection errors of 1-3 pixels. Higher flight altitudes will have higher selection error because these GCPs will appear smaller. This selection error can vary widely by the flight height, GCP target size, and users (careful selection vs. careless selection if the software fails to detect them automatically because the targets appear too small or blurry).

Reasonable maximum accuracy based on the research team's experience and literature (Barry and Coakley, 2013, Pix4D 2019) are typically 1 to 3 GSD. For the example in Figure 9.21, a reasonable maximum accuracy can range from 0.044 *ft* to 0.132 *ft*.


**Figure 9.28 Pixel Error**

***Ground Control Points Accuracy***

The maximum accuracy is limited by the accuracy of the GCPs that is dictated by the measuring surveying equipment. For example:

- Traditional surveying using a total station: ~ 0.01 *ft* (0.3 *cm*).
- Surveying using GNSS: ~ 0.03 *ft* (0.8 *cm*).
- GCPs with GNSS built-in (i.e., Aeropoints): ~ 0.1 *ft* (3 *cm*).
- Surveying using a LiDAR: ranging from 0.03 *ft* (1 *cm*) to 0.1 *ft* (3 *cm*).

***Ground Control Points Spacing with Accuracy***

The GCP spacing affects the positional accuracy in both horizontal and vertical directions.

- When average GCP spacing is equal to or less than 262 *ft* (80 *m*), the achievable horizontal and vertical accuracies are around 3 times GSD.
- When average GCP spacing is equal to or less than 525 *ft* (160 *m*), the achievable horizontal and vertical accuracies are around 4-5 times GSD and 6-8 times GSD, respectively.
- When average GCP spacing is more than 525 *ft* (160 *m*), the achievable horizontal and vertical accuracies are more than 6 times GSD and 10 times GSD, respectively.

The detailed study on GCP spacing is available in Appendix V.

***Example: R 2303-E Pit Site***

This site was so big (29.01 *acres*) and the research team had to fly as high as they can in order to capture the whole site given the limited number of batteries. However, the flight height was limited to 400 *ft* to be in accordance with Federal Aviation Administration 14 CFR Part 107 Small Unmanned Aircraft Systems.

The research team used a camera lens with 25 *mm* focal length, 17.3 *mm* sensor height, and 3956 image heights. With this information, GSD was calculated as follows:

$$GSD = \frac{400\ ft \times 17.3}{25\ mm\ \times 3956} = \ 0.070\ ft\ (2.13\ cm)$$

The site had 13 GCPs with the average spacing of 209 *ft*. With this information, the expected accuracy was 0.070 to 0.21 *ft* (1 to 3 GSD).

The actual average GSD from the commercial software (Pix4D, Agisoft, and UASMaster) was 0.067 *ft* (2.02 *cm*) since the site is not flat. The actual horizontal (Case 1 & Case 2) and vertical (NVA 95%) accuracies were 0.159 *ft* (~ 2.4 GSD) and 0.180 *ft* (~ 2.7 GSD), respectively, which falls within the expected range of accuracy.

## Appendix IV: Multiple Regression Analysis

Previous research (Anders et al. (2020), Lee et al. (2021), Barba et al. (2019), and Catania et al. (2020)) has shown that these 3D point clouds are influenced by numerous factors, such as flight heights, UAS-equipped camera sensors and settings, image, georeferencing, and processing SfM software utilization. To generate consistently high-quality 3D models from UAS-based photogrammetric surveying and mapping, understanding how these factors affect the model accuracy and their levels of significance is important. No previous research uses a quantitative method to analyze more than three impact factors and discuss which factors have a higher or lower impact on accuracy. Thus, the main objective of this research is to assess five major impact factors and identify their levels of significance on horizontal and vertical accuracies using the multiple regression (MR) method through a case study. The impact factors include:

1) flight height,
2) flight overlap,
3) the quantity of GCPs,
4) the focal length of the camera lens, and
5) the average image quality of each image dataset.

Additionally, an MR model is built during the MR analysis to compare the significance of impact factors and predict UAS-based photogrammetric surveying accuracy in the site with similar terrain types. Furthermore, the results of the MR model are validated using the results generated from another site with similar terrain and site conditions.

### *Data Collection and Data Processing*

40 flight missions were conducted at the track facility site with four different flight heights, five different image overlaps, two different focal lengths of lenses. The UAS image data was collected using a DJI Inspire II drone with a DJI Zenmuse X5S camera and an Olympus M.Zuiko 25*mm* and 17*mm* focal length lenses. The following are the detailed flight configurations used to collect the data at the track facility site.

- Flight Heights: 40*m* (131*ft*), 50*m* (164*ft*), 60*m* (197*ft*), and 70*m* (229*ft*)
- Image Overlap: 50%, 60%, 70%, 80%, and 90%
- Focal Length: 17*mm* and 25*mm*

A total of 4425 images were collected for all flight missions. The number of collected images for every flight mission was from 20 to 539. The average image quality of every image data set was between 0.18 and 1.01. The quality of each image was calculated based on the comparison of the contrast gradients in the most peculiar areas between the original image and the Gaussian blur filter applied image through the Agisoft Metashape Estimate Image Quality tool. Table 9.43 lists those 40 flight missions with detailed information.

**Table 9.43 Detailed Flight Mission Information**

| Flight No. | Focal Length (*mm*) | Flight Height (*m*) | Overlap (%) | Average Image Quality | Num. of Image |
|---|---|---|---|---|---|
| 1 | 25 | 40 | 90 | 0.88 | 539 |
| 2 | 25 | 40 | 80 | 0.23 | 161 |
| 3 | 25 | 40 | 70 | 0.30 | 94 |

| | | | | | |
|---|---|---|---|---|---|
| 4 | 25 | 40 | 60 | 0.22 | 57 |
| 5 | 25 | 40 | 50 | 0.96 | 48 |
| 6 | 25 | 50 | 90 | 0.29 | 473 |
| 7 | 25 | 50 | 80 | 0.90 | 156 |
| 8 | 25 | 50 | 70 | 0.24 | 64 |
| 9 | 25 | 50 | 60 | 0.63 | 48 |
| 10 | 25 | 50 | 50 | 0.25 | 39 |
| 11 | 25 | 60 | 90 | 0.60 | 391 |
| 12 | 25 | 60 | 80 | 0.34 | 86 |
| 13 | 25 | 60 | 70 | 0.95 | 47 |
| 14 | 25 | 60 | 60 | 0.28 | 30 |
| 15 | 25 | 60 | 50 | 0.18 | 22 |
| 16 | 25 | 70 | 90 | 0.32 | 120 |
| 17 | 25 | 70 | 80 | 0.40 | 98 |
| 18 | 25 | 70 | 70 | 0.31 | 39 |
| 19 | 25 | 70 | 60 | 0.33 | 30 |
| 20 | 25 | 70 | 50 | 0.58 | 20 |
| 21 | 17 | 40 | 90 | 0.49 | 345 |
| 22 | 17 | 40 | 80 | 1.01 | 148 |
| 23 | 17 | 40 | 70 | 0.48 | 55 |
| 24 | 17 | 40 | 60 | 1.01 | 46 |
| 25 | 17 | 40 | 50 | 0.63 | 35 |
| 26 | 17 | 50 | 90 | 0.92 | 321 |
| 27 | 17 | 50 | 80 | 0.37 | 77 |
| 28 | 17 | 50 | 70 | 0.37 | 48 |
| 29 | 17 | 50 | 60 | 0.63 | 31 |
| 30 | 17 | 50 | 50 | 0.63 | 21 |
| 31 | 17 | 60 | 90 | 0.43 | 226 |
| 32 | 17 | 60 | 80 | 0.63 | 85 |
| 33 | 17 | 60 | 70 | 0.65 | 48 |
| 34 | 17 | 60 | 60 | 0.92 | 28 |
| 35 | 17 | 60 | 50 | 0.51 | 23 |
| 36 | 17 | 70 | 90 | 0.49 | 171 |
| 37 | 17 | 70 | 80 | 0.40 | 75 |
| 38 | 17 | 70 | 70 | 0.50 | 30 |
| 39 | 17 | 70 | 60 | 0.39 | 30 |
| 40 | 17 | 70 | 50 | 0.42 | 20 |

When processing the images for 3D reconstruction, 4, 6, 8, and 10 GCPs were used, leading to 160 combinations of datasets (40 flight configurations ×4 sets of GCPs). The data were processed based on all the flight missions with different GCP quantities using Pix4DMapper.

***Multiple Regression Analysis***

$RMSE_R$ and RMSEz were used to evaluate the model accuracy in statistical analysis. The level of significance of impact factors was assessed using the significance value, also known as the p-value, at a 95% confidence level. If the p-value of an impact factor is less than 0.05, that means this impact factor is statistically significant. Otherwise, the impact factor has no significance in statistics.

When developing the MR prediction model, the relationships between impact factors and the distribution and skewness of the dependent variables ($RMSE_R$ and RMSEz) were checked and considered. The reason to check the relationship between impact factors was to observe if there was interaction existing. Interaction presents a particular type of non-linear relationship, which means the influence of an independent variable on the dependent variable varies at different values of another independent variable in the model. The reason to check the distribution of the dependent variables was to identify if the dependent variables followed a normal distribution. Although it was not required that the distribution be a normal distribution, it could eliminate the harmful effects and develop more accurate MR prediction models using a transformation when the distribution was very skewed.

Two MR prediction models were built based on the value of impact factors to predict the $RMSE_R$ and RMSEz. IBM SPSS Statistics and R-Studio were used to conduct the statistical analysis. The MR models were computed using the following regression equation:

$$y_i = \beta_0 + (\sum_j^m \beta_m \times x_{im}) + \varepsilon \quad (5)$$

Where..

- $i$ is the dataset combination numbers, in this case, ranging from 1 to # of $n$ (160 in this case).
- $y_i$ is the dependent variable, which is $RMSE_R$ and RMSEz, or the value of transformed $RMSE_R$ and RMSEz, respectively, in this case.
- $x_{im}$ is the independent variables, which are impact factors in this case, and $m$ ranging from 1 to 5.
- $\beta_0$ is the intercept of $y_i$, which is the value of y-axis when all the independent variables are equal to zero.
- $\beta_m$ is the regression coefficient.
- $\epsilon$ is the residuals, which is negligible

The regression coefficients $\beta_m$ represents the slope of the line between the independent variable and the dependent variable. It indicates how much the dependent variable varies with an independent variable when all other independent variables are held constant ($\beta_0$). Following is the equation (6):

$$\beta_m = \frac{\sum(x_{im} - \overline{x_m}) \times (y_i - \bar{y})}{\sum(x_{im} - \overline{x_m})^2} \quad (6)$$

Where:

- $\overline{x_m}$ is the average value of independent variables.
- $\bar{y}$ represents the average value of the dependent variables.

***Results***

This research aimed at understanding how the five impact factors influence the UAS-based photogrammetry accuracy and develop an MR model to predict the horizontal and vertical accuracies based on the known flight and site information. This results section is divided into two subsections: The influence of impact factors and their level of significance and the accuracy prediction.

***Influence of Impact Factors and Their Level of Significance on Accuracy***

Figure 9.29 shows the mean of $RMSE_Z$ and $RMSE_R$ for the five impact factors. According to all the figures, the means of $RMSE_Z$ are higher than that of $RMSE_R$ for all the impact factors. That means the impact factors have greater influence on vertical accuracy than horizontal accuracy. As shown in Figure 9.29 (a), the mean of $RMSE_Z$ and $RMSE_R$ of the 17 *mm* focal length lens is lower, which means the 17 *mm* focal length yielded higher horizontal and vertical accuracies than that of the 25 *mm* focal length lens. Figure 9.29 (b) shows that low flight heights yielded low errors in the horizontal direction. The mean of $RMSE_R$ for 40 *m* and 50 *m* flight heights was lower than the mean of $RMSE_R$ for 60 *m* and 70 *m*. The highest accuracy in the horizontal direction is achieved when the flight height is 50 *m*. However, the mean of $RMSE_Z$ for 60 *m* and 70 *m* flight heights was lower, although the difference was 0.02 *m*. The lowest $RMSE_Z$ is obtained using 70 *m* flight height.

As shown in Figure 9.29 (c) and (d), increasing the image overlap and the number of GCPs improves horizontal and vertical accuracies. However, there is no noticeable difference in $RMSE_R$ using over 6 GCPs. Additionally, Figure 9.29 (e) shows that the datasets with high image quality yield higher accuracy in both directions, although the accuracy fluctuates.

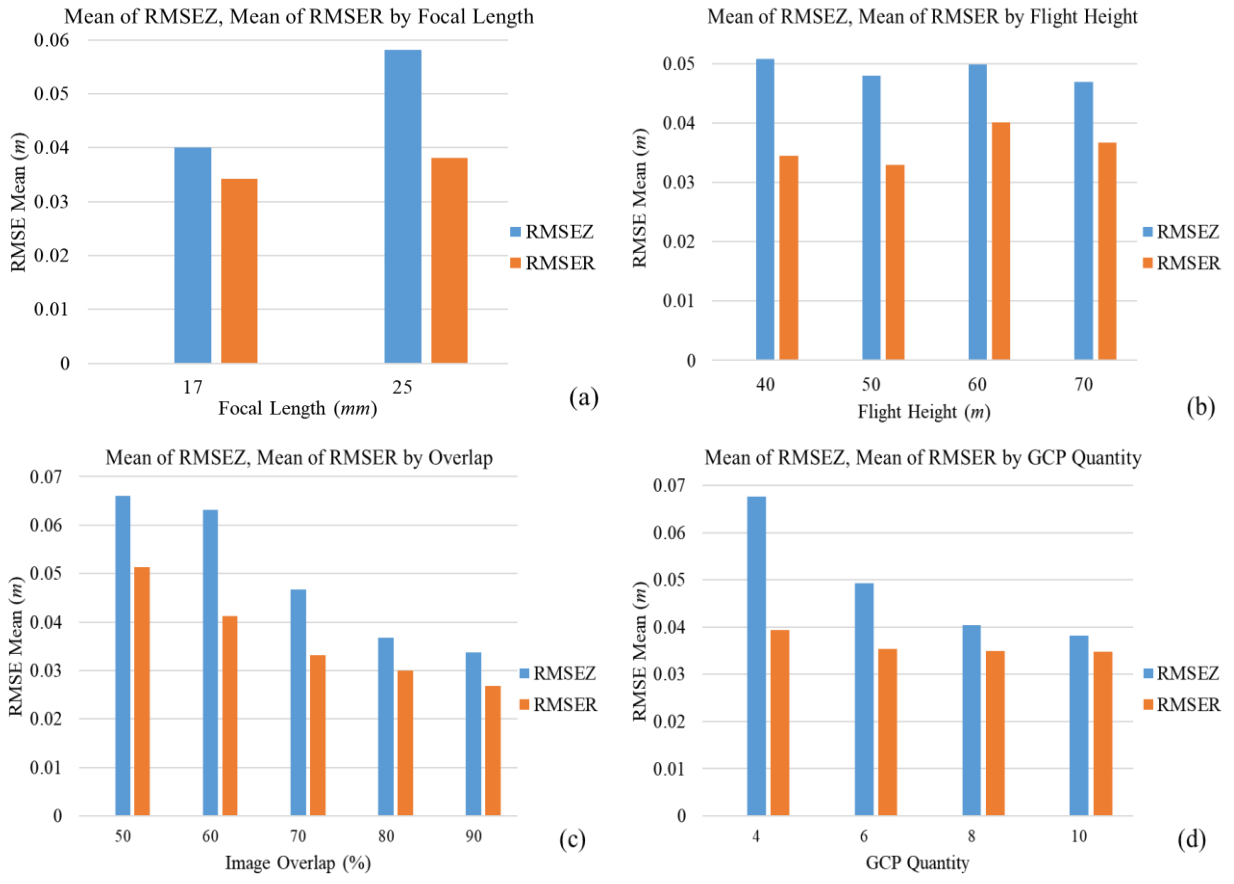

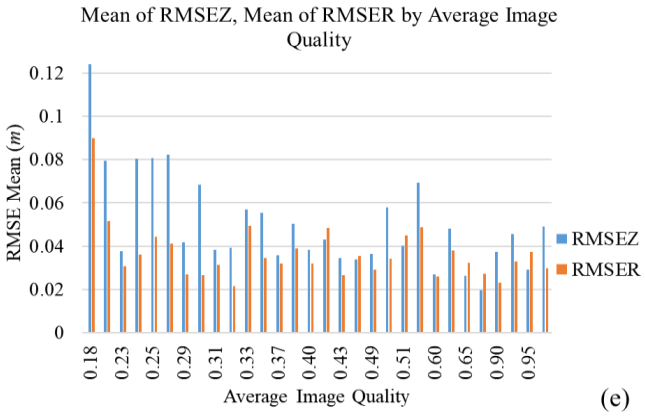


**Figure 9.29 Mean of $RMSE_Z$ and $RMSE_R$ for Five Impact Factors: (a) Mean of $RMSE_Z$ and $RMSE_R$ for Different Focal Length of Lenses; (b) Mean of $RMSE_Z$ and $RMSE_R$ for Different Flight Heights; (c) Mean of $RMSE_Z$ and $RMSE_R$ for Different Overlaps; (d) Mean of $RMSE_Z$ and $RMSE_R$ for Different GCP Quantities; and € Mean of $RMSE_Z$ and $RMSE_R$ for Different Average Image Quality**

Table 9.44 below lists the t-values and p-values of the flight height, the focal length of lenses, image overlap, average image quality, and GCPs quantity on $RMSE_Z$ and $RMSE_R$. Both the overlap and the GCP quantities have significant impacts with a 95% confidence level on $RMSE_Z$ since the p-values are smaller than 0.05. Compared to other factors, the image overlap has a substantial impact with the 95% confidence level on $RMSE_R$ since the p-values are smaller than 0.05. The focal length, flight height, and average image quality have a low significant influence on both $RMSE_Z$ and $RMSE_R$.

**Table 9.44 Level of Significance of Impact Factors**

| | RMSEZ | | RMSER | |
|---|---|---|---|---|
| | t-value | p-value | t-value | p-value |
| **Constant** | 3.442 | 0.009 | 7.831 | <0.001 |
| **Focal Length** | 0.298 | 0.773 | -2.223 | 0.057 |
| **Flight Height** | -0.816 | 0.438 | 0.956 | 0.367 |
| **Image Overlap** | -3.093 | 0.015 | -10.206 | <.001 |
| **GCP Quantity** | -2.697 | 0.027 | -1.709 | 0.126 |
| **Average Image Quality** | -0.837 | 0.427 | 1.838 | 0.103 |

***MR Prediction Model Development***

The interactions between impact factors were found. That means the influence of one impact factor on the accuracy is impacted when varying other impact factors.

The distributions of $RMSR_Z$ and $RMSE_R$ are right-skewed (the values of skewness of $RMSR_Z$ and $RMSE_R$ are 0.918 and 2.801, respectively). To improve the MR prediction model fitness, instead of directly using the values of $RMSR_Z$ and $RMSE_R$, a logarithm transformation is used to transform the values of $RMSR_Z$ and $RMSE_R$ to the values of $lgRMSR_Z$ and $lgRMSE_R$. The following are the equations of logarithm transformation:

$$lgRMSE_z = \lg(RMSE_Z)$$
$$lgRMSE_R = \lg(RMSE_R)$$

After transformation, the skewness of the distribution of the value of $lgRMSR_Z$ and $lgRMSE_R$ are -0.024 and 1.098, separately, which means the new distributions are closer to normal distributions. Thus, the MR prediction models are established using the values of $lgRMSR_Z$ and $lgRMSE_R$, the values of impact factors, and the interactions between impact factors. The following equations present the developed MR prediction models from MR analysis:

$$\begin{aligned} y_Z = \; & -4.234 + 0.161 \times x_{i1} + 0.017 \times x_{i2} + 0.022 \times x_{i3} + 0.025 \times x_{i4} + 2.399 \times x_{i5} \\ & - 0.001 \times x_{i1} \times x_{i2} - 0.001 \times x_{i1} \times x_{i3} - 0.049 \times x_{i1} \times x_{i5} \\ & + 6.609 \times 10^{-5} \times x_{i2} \times x_{i3} - 0.014 \times x_{i2} \times x_{i5} - 0.001 \times x_{i3} \times x_{i4} \\ & - 0.011 \times x_{i3} \times x_{i5} + 0.003 \times x_{i4} \times x_{i5} \end{aligned}$$

$$\begin{aligned} y_R = \; & -1.353 + 0.027 \times x_{i1} - 0.003 \times x_{i3} - 0.021 \times x_{i4} - 0.387 \times x_{i5} \\ & - 4.066 \times 10^{-5} \times x_{i1} \times x_{i2} - 0.001 \times x_{i1} \times x_{i5} - 4.549 \times 10^{-5} \times x_{i2} \times x_{i3} \\ & + 5.933 \times 10^{-5} \times x_{i2} \times x_{i4} + 0.005 \times x_{i3} \times x_{i5} - 0.011 \times x_{i4} \times x_{i5} \end{aligned}$$

Where $y_Z$ is the estimated value of $lgRMSR_Z$, $y_{ZR}$ is the estimated value of $lgRMSR_R$. $x_{i1}$ is the value of focal length; $x_{i2}$ is the value of flight height; $x_{i3}$ is the value of image overlap; $x_{i4}$ is the value of the GCP quantity; and $x_{i5}$ is the value of average image quality. –4.234 and –1.353 are the intersect ($\beta_0$ of the MR prediction model). The rest of the constants are the parameters of impact factors.

***Example – Butner Test Site***

Here is an example of using the developed MR prediction models to estimate the accuracy of the data collected at the Butner site. Butner site has similar terrains to the track facility site, which contained a building facility, open space, and vegetation. Two datasets of the Butner site used in this research were collected on February 25th, 2021. The detailed flight configuration is listed in Table 3.3 in Chapter 3. The average image qualities of both image datasets were 0.85 and 0.48. 13 and 12 GCPs (see Figures 9.2 and 9.3) were used for the two datasets processing using Pix4D, respectively.

To utilize the MR prediction models, the values of impact factors from the test site were imported into the MR prediction models to produce the predicted $lgRMSE_Z$ and $lgRMZE_R$ for flight missions 1 and 2. The predicted $lgRMSE_Z$ and $lgRMZE_R$ for flight mission 1 are -2.753 and -1.577, respectively. The predicted $lgRMSE_Z$ and $lgRMZE_R$ for flight mission 2 are -1.534 and -1.643, separately. Then, an exponential function with the base of 10 is used to convert the values of predicted $lgRMSE_Z$ and $lgRMZE_R$ to the values of predicted $RMSE_Z$ and predicted $RMSE_R$. The following are the exponential function for predicted $RMSE_Z$ and predicted $RMSE_R$.

$$RMSE_z = 10^{\mathrm{lgRMSE}_Z}$$
$$RMSE_R = 10^{\mathrm{lgRMSE}_R}$$

Table 9.45 shows the validation results using these two MR prediction models with the data collected from the Butner UAS Test site. The differences of RMSEZ from Pix4D and predicted RMSEZ from the MR model for both flight missions are 0.011 *ft* and 0.026 *ft*, respectively. The differences of RMSER from Pix4D and predicted $RMSE_R$ from the MR model for flight missions 1 and 2 are 0.005 *ft* and 0.006 *ft*, respectively.

**Table 9.45 Results of Butner UAS Test Site from Pix4D and MR Models**

| Flight Mission | $RMSE_Z$ from Pix4D (*ft*) | $RMSE_R$ from Pix4D (*ft*) | Predicted $RMSE_Z$ from MR Model (*ft*) | Predicted $RMSE_R$ from MR Model (*ft*) |
|---|---|---|---|---|
| 1 | 0.070 | 0.080 | 0.059 | 0.085 |
| 2 | 0.069 | 0.081 | 0.095 | 0.075 |

## Appendix V: Ground Control Spacing

The quantity and distribution of GCPs have direct impact on survey accuracy. For instance, increasing the number of well-distributed GCPs improves the 3D point clouds accuracy (Barba et al., 2019; Ferrer-González et al., 2020). Thus, the common way to improve accuracy is to increase the number of GCPs used on the sites.

However, placing GCPs and surveying their coordinates are labor intensive and time consuming, increasing the overall costs for NCDOT and its subcontractors. Thus, it is essential to identify the relationship between GCPs placement and 3D point cloud accuracy to find the most optimal number of GCPs for different sites. Several studies (Oniga et al. (2018), Martínez-Carricondo et al. (2018), Bolkas (2019), and Ferrer-González, et al. (2020)) have been researched to determine the optimum number of GCPs in certain sizes of study sites. Not much research studies the impact of GCPs quantities and separation spacing on the UAS-based photogrammetric surveying accuracy.

### *Research Objective and Method Overview*

This research aims to determine the optimal numbers and spacing of GCPs on different levels of accuracy for preconstruction and construction sites. The Butner and U2412-A construction sites' UAS and LiDAR data were used in this research. Figure 9.30 depicts the workflow of the method. LiDAR offers the means to acquire point clouds with millimeter-level accuracy and millimeter- to centimeter-level point spacing. Due to these advantages, LiDAR has been used in studies for the accuracy assessment of UAS surveys. The collected LiDAR point clouds were segmented into a small size (131 *ft* by 131 *ft*) of LiDAR point clouds. The near corner points were manually chosen as GCPs. After that, those selected GCPs were imported into the collected UAS image data processing. This UAS image data were processed by Pix4DMapper. After processing all the image data, a sparse point cloud was reconstructed, and the horizontal and vertical accuracies were assessed by using RMSE. The following subsections present the detailed information and tasks of this research.

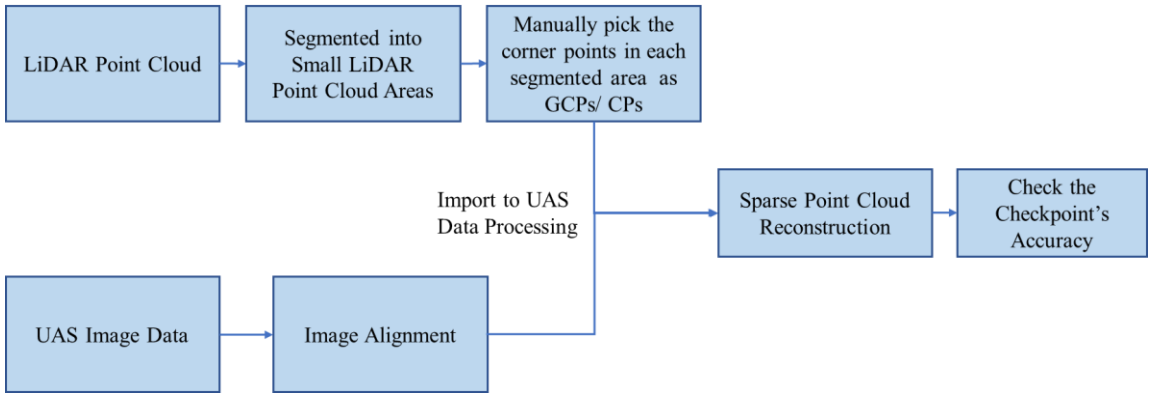


**Figure 9.30 Workflow of the Method**

***LiDAR Point Cloud Segmentations***

This section describes the LiDAR point cloud segmentation method and the GCP selection for the Butner and U2412-A construction sites.

The dimensions of the study areas of the Butner site and the U2412-A construction site are 671 *ft* by 797 *ft* and 2180 *ft* by 284 *ft*, respectively. The point clouds of both sites were segmented into small size grids (131 *ft* by 131 *ft*) from the center lines (shown in red lines). Figures 9.31 and 9.32 show the LiDAR point cloud segmentation of the Butner and U2412-A construction sites.

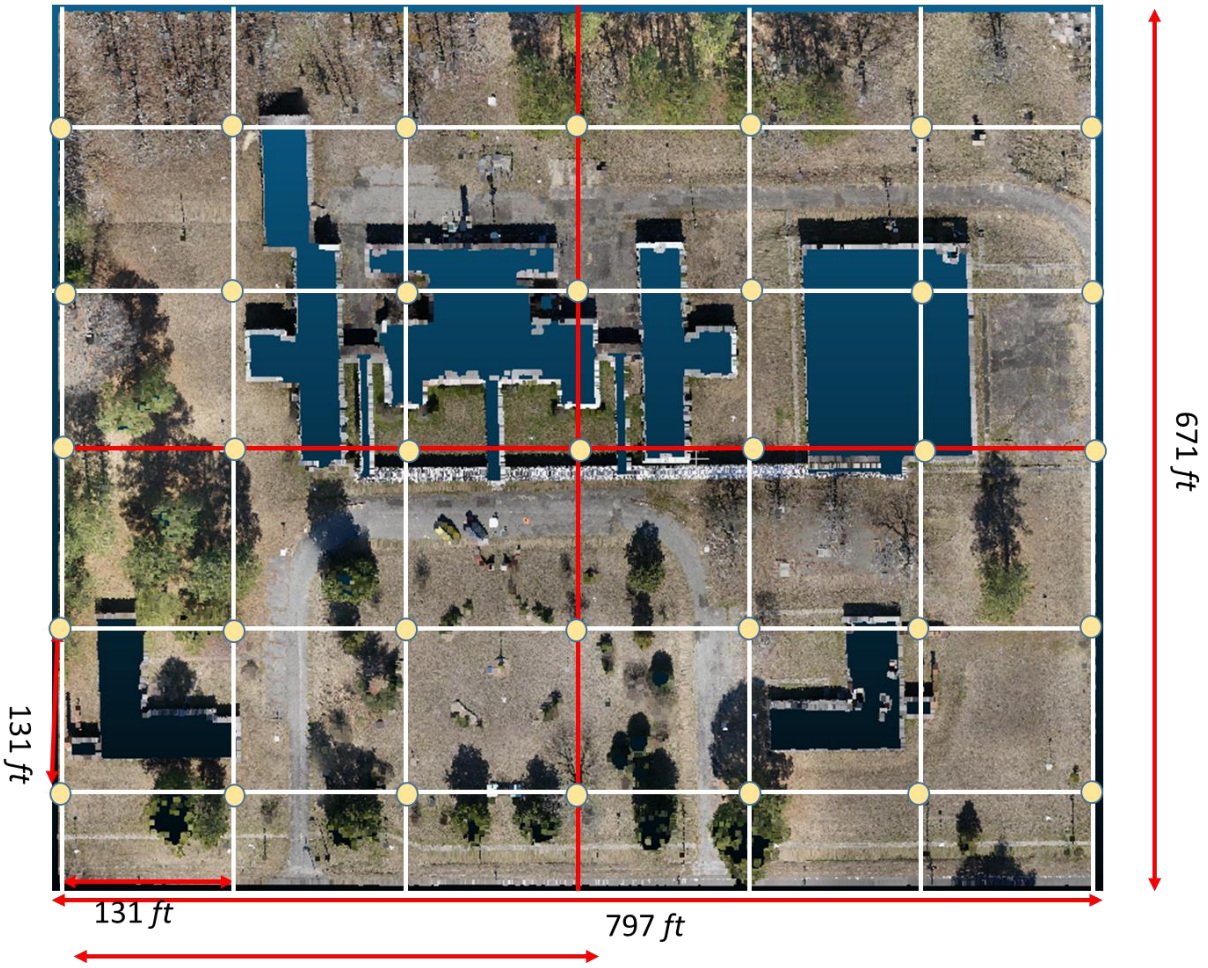


**Figure 9.31 Butner Site Point Cloud Segmentation**

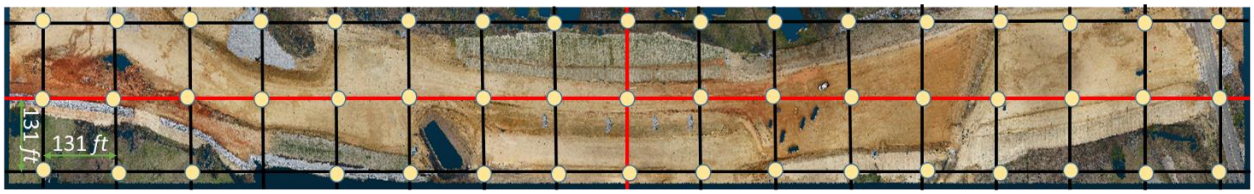


**Figure 9.32 U2412-A Construction Site Point Cloud Segmentation**

Three different GCPs quantities distributions were used to evaluate the influence of GCP quantity and spacing on the accuracy on each site.

For the Butner site, 4, 6, and 9 GCPs were picked with rectangular distribution and different separation distances. Figures 9.33 -9.35 show the layout of the GCPs at the Butner site. The GCPs are shown in yellow. The average GCP spacing of using different numbers of GCPs varied from 1181 *ft* to 525 *ft*. The detailed GCP spacing information lists in Table 9.46.

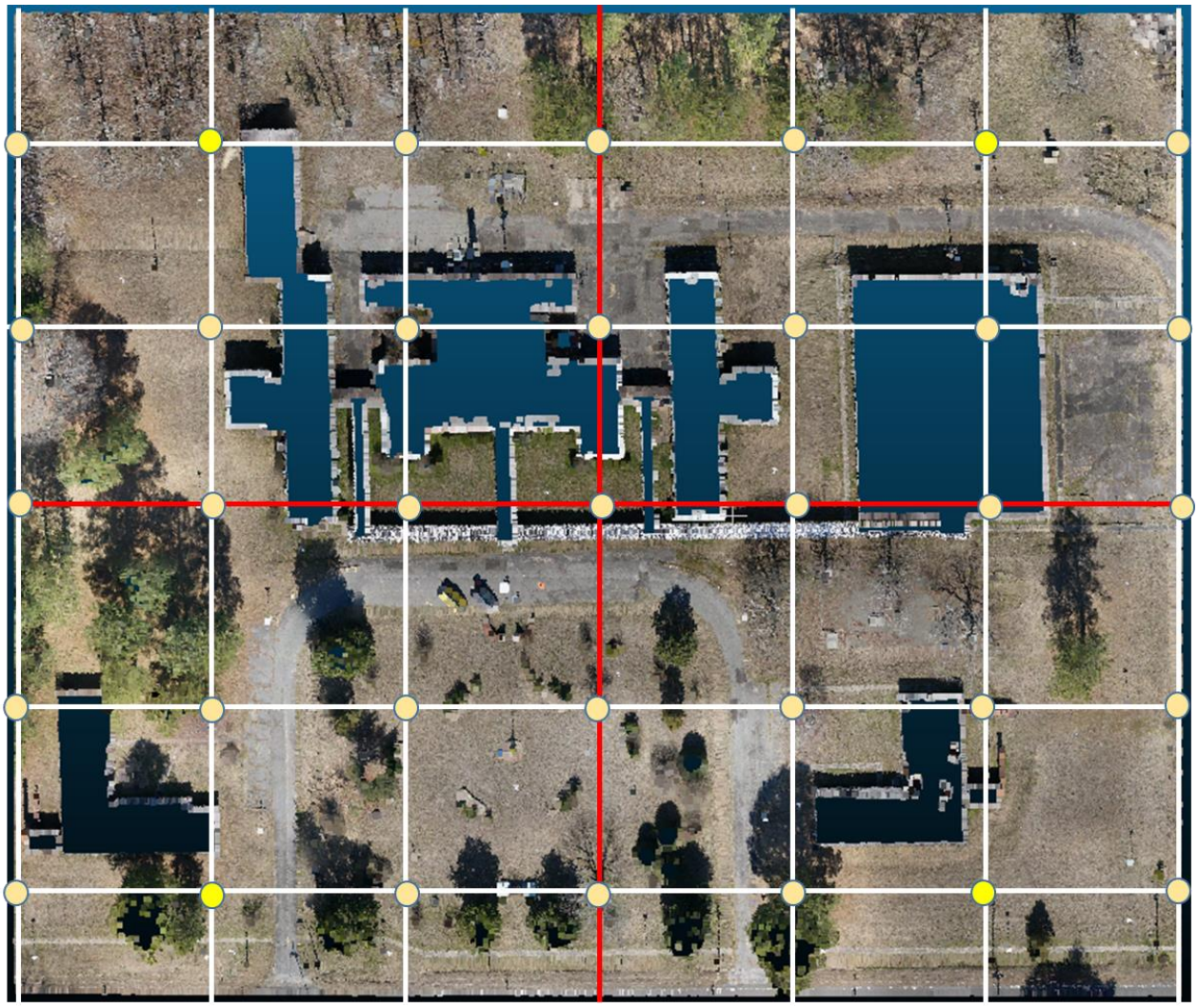

**Figure 9.33 Butner Site 4 GCPs Rectangular Distribution**

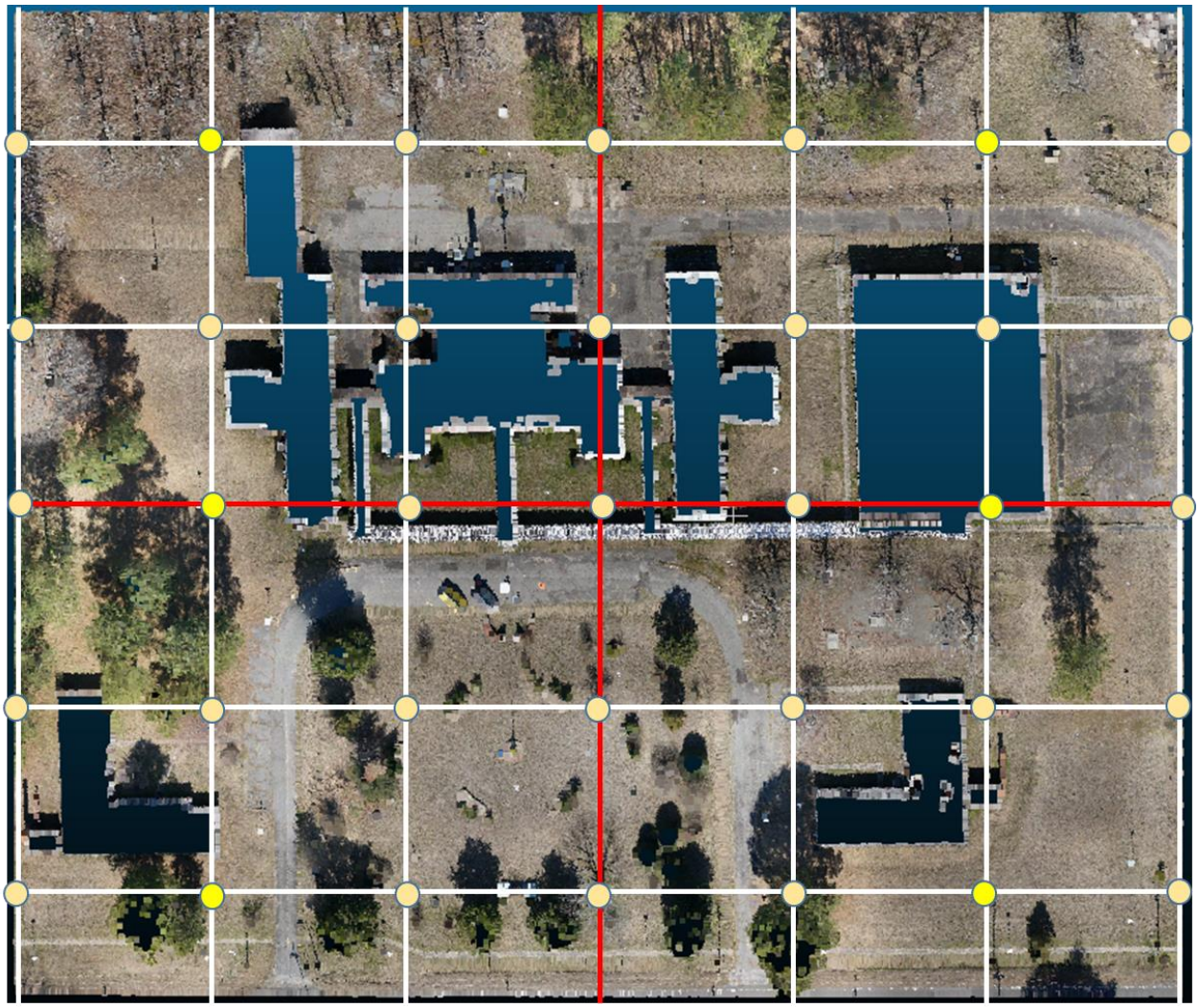

**Figure 9.34 Butner Site 6 GCPs Rectangular Distribution**

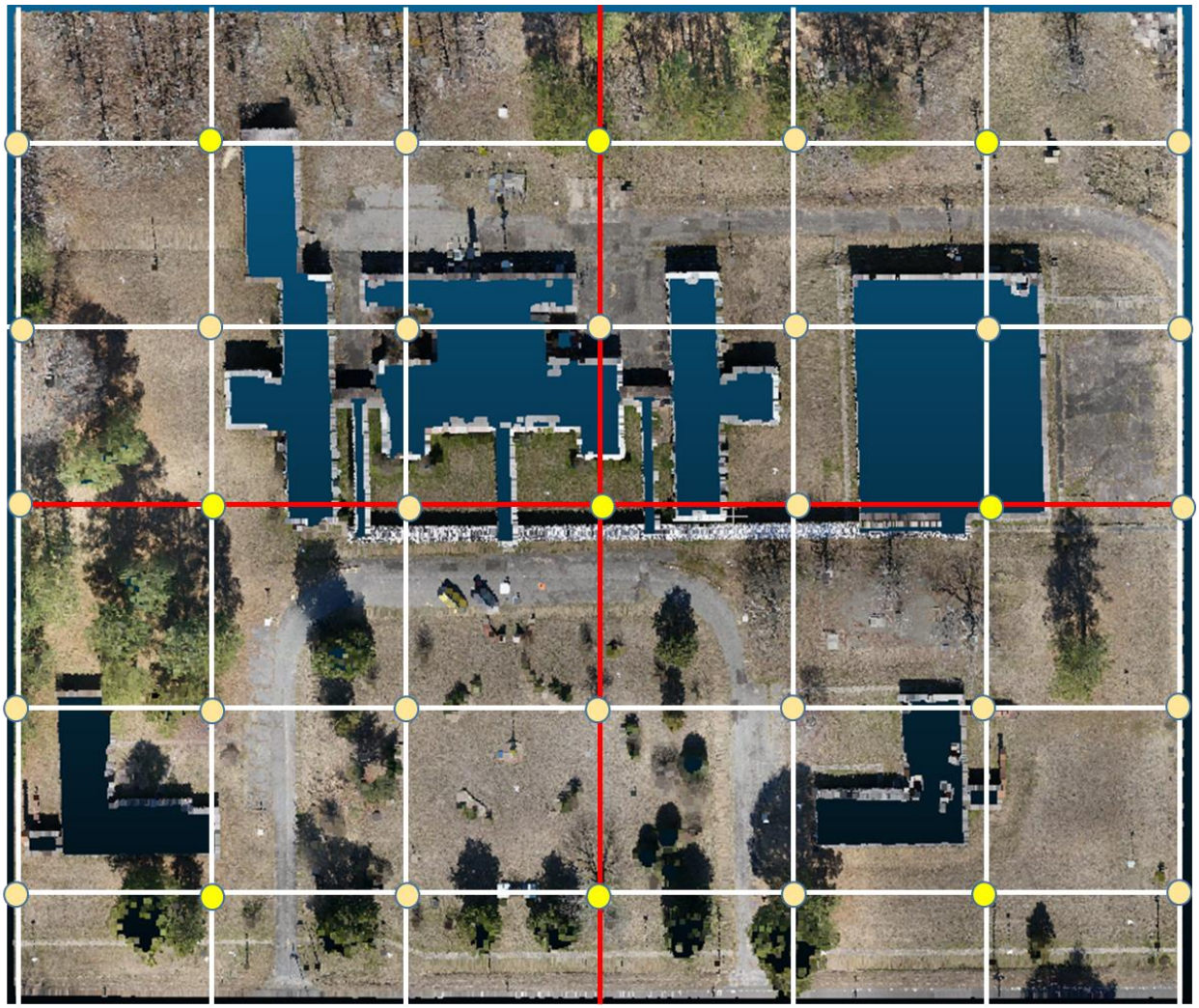

**Figure 9.35 Butner Site 9 GCPs Rectangular Distribution**

**Table 9.46 GCP Spacing at Butner Site**

| GCP Quantity | GCP Spacing (*ft*) | Average GCP Spacing (*ft*) |
|---|---|---|
| 4 | 525 | 525 |
| 6 | 262 -525 | 374 |
| 9 | 262 | 262 |

For the U2412-A construction site, 4, 6, and 8 GCPs were picked with rectangular distribution and different separation distances. Figures 9.36 -9.38 show the layout of the GCPs. The GCPs are shown in yellow. The average GCP spacing of using different numbers of GCPs varied from 525 *ft* to 262 *ft*. The detailed GCP spacing information lists in Table 9.47.

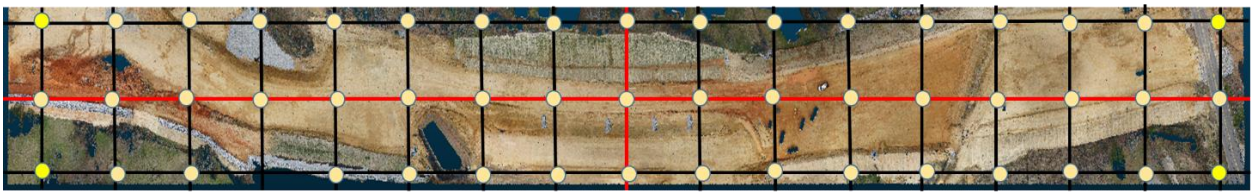

**Figure 9.36 U2412-A Construction Site 4 GCPs Rectangular Distribution**

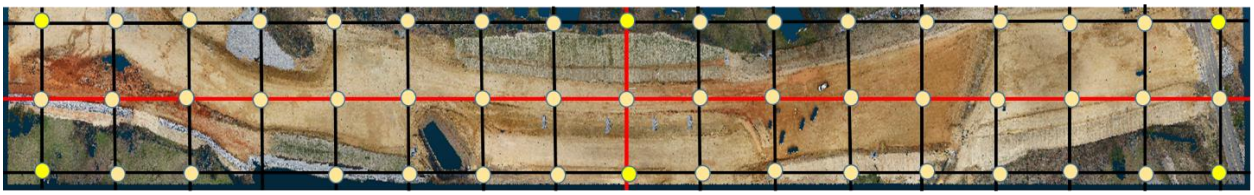

**Figure 9.37 U2412-A Construction Site 6 GCPs Rectangular Distribution**

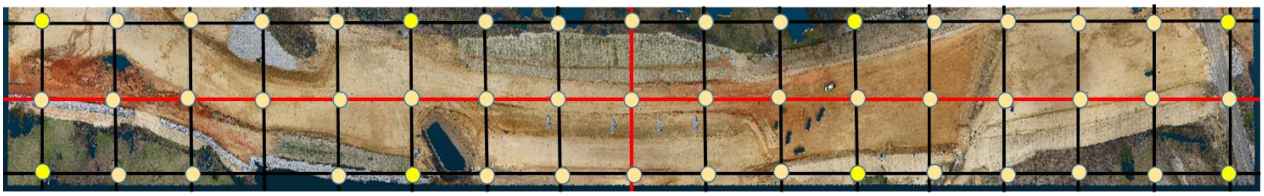

**Figure 9.38 U2412-A Construction Site 8 GCPs Rectangular Distribution**

**Table 9.47 GCP Spacing at U2412-A Construction Site**

| GCP Quantity | GCP Spacing (*ft*) | Average GCP Spacing (*ft*) |
|---|---|---|
| 4 | 262 - 2100 | 1181 |
| 6 | 262 -1050 | 830 |
| 8 | 262 - 787 | 525 |

***Results***

This study aimed at identifying the GCP quantity and spacing influence on the UAS-based photogrammetric surveying accuracy. The results show that increasing GCP quantity and decreasing GCP separation distance can improve the accuracy in horizontal and vertical directions. Moreover, a shorter distance produces better results when using the same number of GCPs with different separation distances. The detailed results list in Table 9.48.

**Table 9.48 Accuracy of GCP Spacing**

| Sites | GCP Quantity | GCP Spacing (*ft*) | Average GCP Spacing (*ft*) | RMSER (*ft*) | RMSEZ (*ft*) |
|---|---|---|---|---|---|
| Butner Site | 4 | 525 | 525 | 0.156 | 0.217 |
| | 6 | 262 -525 | 374 | 0.141 | 0.148 |
| | 9 | 262 | 262 | 0.090 | 0.096 |
| U2412-A Construction Site | 4 | 262 - 2100 | 1181 | 0.198 | 1.815 |
| | 6 | 262 -1050 | 830 | 0.167 | 0.281 |
| | 8 | 262 - 787 | 525 | 0.130 | 0.197 |

### *Assumptions and Limitations*

To effectively utilize the findings of this study, understanding of the assumption and limitation is very important. The recommended GCP spacing is only applicable to specific GSDs that were used in this study because this research is conducted using a fixed flight height and a camera lens. Thus, flight missions with notably different GSDs should not use the recommended GCP spacing. However, NCDOT should be able to use the recommended spacing as they will have very similar GSDs in most cases because they use a lens with similar a camera (the same model but a generation older) and will likely fly at the maximum flight height to cover large terrains (i.e., highway construction). The flight height in this study was very close to the maximum flight height allowed by FAA.

Moreover, note that this study assumes the collected data will have good quality images that are fully aligned and uniformly registered during the SfM data processing. The recommended GCP spacing does not guarantee successful SfM. Insufficient image overlap and/or poor image quality may still lead to undesirable local accuracies between GCPs even with the recommended spacing.

Further investigation is needed, if NCDOT would like to acquire recommended GCP spacing for varying GSDs (i.e., different flight heights and cameras) and varying image quality and overlaps.